Magnetic Field Distribution in the Quiet Sun

Bartolomeo Viticchiè

Università degli Studi di Roma "Tor Vergata"
Dottorato in Astronomia XXI Ciclo

a.a. 2008/2009

PhD Supervisor
Prof. Francesco Berrilli

PhD Coordinator
Prof. Pasquale Mazzotta

Dedicated to Sara

Quiero ver la risa del Sol por las mañanas
Que venga siempre a golpearnos la ventana
Yo quiero un Sol, yo quiero un Sol que siempre me acompañe
Hablando siempre de frente, tirando todo lo malo

Diego Torres in "Abriendo Caminos"

Contents

Abstract

Modern observations of the solar surface performed with high polarimetric sensitivity and high spatial resolution reveal how magnetic fields are present almost everywhere on the solar photosphere. These fields fill more than 90% of the solar surface causing weak polarization signals to emerge from those regions where old magnetometers could not reveal any magnetic field: the quiet Sun.
Nowadays, thanks to remarkable improvements in theory, observations and diagnostic techniques, it is well known that quiet Sun magnetic fields vary between zero and about 2 kG and are continuously moved and shuffled by photospheric plasma motions acting over timescales of few minutes. In this scenario, the weak polarization signals covering the solar photosphere can be interpreted as the result of the linear combination of the polarization emerging from discrete magnetic flux tubes; these flux tubes are smaller than the angular resolution of observations and fill the solar photosphere with a complex topology imposed by the photospheric plasma dynamics.

In spite of the recent improvements much work remains to be done to completely understand the solar surface magnetism. In this thesis we investigate the quiet Sun magnetism through the development and integration of dynamical models, synthesis and inversion of lines sensible to magnetic fields via Zeeman effect and MHD simulations. The work done can be organized in four main topics:

- We simulated the dynamics and the evolution of quiet Sun magnetic elements to study the statistical properties of the field strengths associated with such elements.
  The dynamics of the magnetic field is simulated by means of a numerical model in which magnetic elements are passively driven by an advection field characterized by spatio-temporal correlations that mimick the granulation and mesogranulation scales observed on the solar surface. The field strength can increase due to an amplification process

that occurs where magnetic elements converge.
Our model is able to produce kG magnetic fields in a time interval of the order of the granulation timescale. The mean unsigned flux density and the mean magnetic energy density of the synthetic quiet Sun reach values of $\langle B \rangle \simeq 100$ G and $\langle B^2 \rangle^{1/2} \simeq 350$ G respectively. The probability density function of the magnetic field strength derived from this simulation shows how $B \geq 700$ G fields dominate both the unsigned flux density and magnetic energy density, although the probability density function of the field strength presents a maximum at $B \sim 10$ G.

- We performed the first syntheses of Mn I lines in realistic quiet Sun model atmospheres. Plasmas varying in magnetic field strength, magnetic field direction, and velocity, contribute to the synthetic polarization signals.
  The syntheses show how the Mn I lines weaken with increasing field strength. In particular, kG magnetic concentrations produce Mn I λ5538 circular polarization signals (Stokes V) which can be up to two orders of magnitude smaller than what the Weak Field Approximation predicts. Therefore, the polarization emerging from an atmosphere having weak and strong fields is biased towards the weak fields, and hyperfine structure features characteristic of weak fields show up even when the magnetic flux and energy are dominated by kG fields. Moreover, atmospheres with unresolved velocities produce very asymmetric line profiles, which cannot be reproduced by simple one-component model atmospheres. Inversion techniques accounting for complex magnetic atmospheres must be implemented for a proper diagnosis.

- We analyzed Stokes I and V signals observed by the HINODE SOT/SP instrument by adopting the MIcro Structured Magnetic Atmosphere hypothesis. The analysis has as a final goal the definition of a probability density function for the statistical description of quiet Sun magnetic fields for a direct comparison with recently published results. Here we present preliminary results obtained from the inversion of about 15000 spectropolarimetric profiles.

- We analyzed the properties of the Mn I λ5395 photospheric line in relation to its larger activity, than most other photospheric lines, related to the solar cycle.
  We performed classical one-dimensional modelling as a starting point to understand the properties of the line and then we used recent three-dimensional MHD simulations for verification and analysis.

The Mn I λ5395 sensitivity to solar activity derives from its hyperfine structure. This overrides the thermal and granular Doppler smearing through which other photospheric lines lose such sensitivity. We take the nearby Fe I λ5395 line as example of the latter and analyze the formation of both lines in detail to demonstrate granular Doppler brightening.

Chapter 1

Quiet Sun Magnetic Fields

1.1 Introduction

The Sun is a unique astrophysical object. It is the only star that can be resolved and on which physical processes can be observed in detail. By observing the Sun, we learned how stellar atmospheres can be extremely complex, highly structured and controlled by the interaction between magnetic fields, turbulent plasma and heating processes. These interactions manifest their effects in stellar activities (e.g., spots, flares, stellar winds) and stellar global cyclic evolution. For these reasons the Sun can be considered the prototype star in astrophysics.
The Sun is an extraordinary laboratory of plasma physics. It continuously carries out new experiments in conditions that are not reproducible in laboratory. By remote sensing of these experiments we can explore totally inaccessible physical conditions also in modern laboratory experiment and MHD simulations.
The Sun is the source of energy of our planetary system. The interplanetary space is filled with the tenuous, hot and supersonically expanding corona which extends beyond the orbit of Pluto where it is blocked by the interaction with the interstellar medium. This region, named heliosphere, experiences strong modifications of its physical conditions in response to the magnetic activity of the Sun.
In spite of the shielding provided by the terrestrial magnetosphere, it is also well known that terrestrial climate is affected by the solar magnetic activity. More in detail, we can talk about a modulation of earth climate conditions due to the solar magnetic field activity. As an example, in the period roughly from 1645 to 1715 sunspots became exceedingly rare, as noted by solar observers of the time; this phase of the solar activity, also named Maunder

Minimum, coincided with the middle and coldest part of the Little Ice Age, during which Europe and North America were subjected to bitterly cold winters. Simultaneously, short time fluctuations are clearly associated to the appearance of spots or bright faculae on the solar photosphere. As a consequence, a detailed knowledge of the solar magnetic field would allow to understand the extra-terrestrial contribution to climate variation and, at the same, would help to disentangle this from the effects caused by the human activity.
The fundamental physical ingredient to understand the different aspects of the solar activity described above is the solar magnetic field. For this reason, the study of the solar magnetism is one of the most important topic in solar physics. In this thesis we'll focus on the study of the magnetic fields of the solar photosphere and, more in detail, on quiet Sun magnetic fields. Before introducing the quiet Sun and illustrating in detail the state of the art of the study of this region of the solar photosphere, we rapidly introduce here the origin of the photospheric magnetic fields and the large variety of magnetic features observed on the solar photosphere.

It is well known that the origin of the solar magnetic fields lies in the dynamo located at the base of the solar convection layer, in a region with a thickness of about 10^4 km also referred to as the convective overshoot layer (e.g., Spiegel & Weiss 1980). This idea was originally proposed long time ago by Larmor (1919) and then further developed by Cowling (1933) and Parker (1955). Qualitatively, the dynamo involves the generation of a toroidal component of the magnetic field (directed azimuthally) from a poloidal (meridional) magnetic field due to the differential rotation of the star (ω effect). The next step is the regeneration of the poloidal field from the toroidal field. A workable model for this mechanism was proposed Parker (1955) by the addition of helical motion due to the Coriolis forces (α effect).
Once the field has been amplified up to $10^4 - 10^5$ G by the dynamo, it is released into the convection zone and transported to the surface by the magnetic buoyancy (Parker 1955). The magnetic buoyancy acts on flux tubes in pressure equilibrium with the surrounding unmagnetized plasma so that $p_i + B^2/8\pi = p_e$, where p_i and p_e represents the internal and external pressure respectively and B is the field strength in the flux tube. If $T_i = T_e$, since $p_i < p_e$ the gas in the tube is less dense than its surrounding ($\rho_i < \rho_e$), implying that the tube will rise into the convection zone and then to the solar surface under the effect of the gravity.
Let us now focus on the magnetic fields in the photosphere. The magnetic field on the solar surface consists on discrete elements having different sizes, from about 50000 km for the largest sunspots down to 100 km of intense

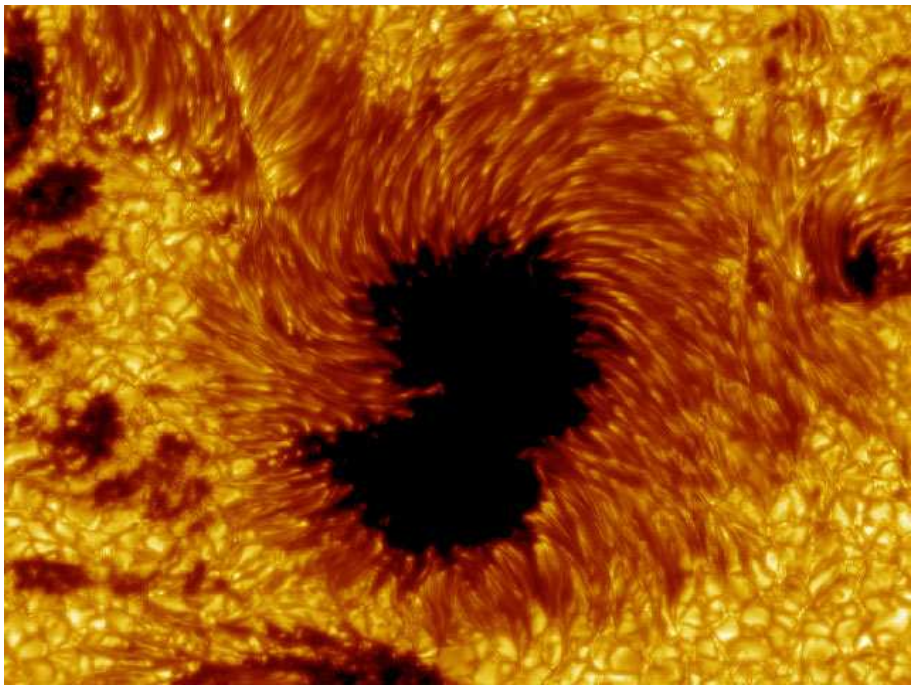

Figure 1.1: White light closeup of a sunspot. The umbra, darkest region, and the penumbra, radial filamentary region as observed by the Swedish 1 m Solar Telescope at La Palma in the Canary Islands. The granulation convection pattern surrounding the spot is easily recognizable.

flux tubes, and different typical timescales ranging from several weeks to few minutes. Sunspots (see Figure 1.1) are the most evident signatures of the photospheric magnetism. They have typical dimensions of 30000 km, kilogauss (kG) magnetic field strengths and typical lifetimes of the order of one week. The core of the spot is typically named the umbra. It's well recognizable as the darkest part of the spot, where the field lines are approximately vertical and where the energy transport by convection is inhibited by the strong kG magnetic field, typically above 1.5 kG. Sunspots appear extremely dark due to the contrast with the surrounding 5800 K photosphere; in fact, the typical temperature of the umbra is about $4000 - 4500$ K. All around the umbra there's the penumbra presenting filaments oriented radially towards the granulation surrounding the spot. The penumbra is lighter than the cold sunspot core and is characterized by inclined magnetic field lines, the geometry of the filaments is representative of such field configuration.
On smaller dimensions compared with sunspots, the pores have spatial extension of few thousands of kilometers, magnetic fields of the order of few kG

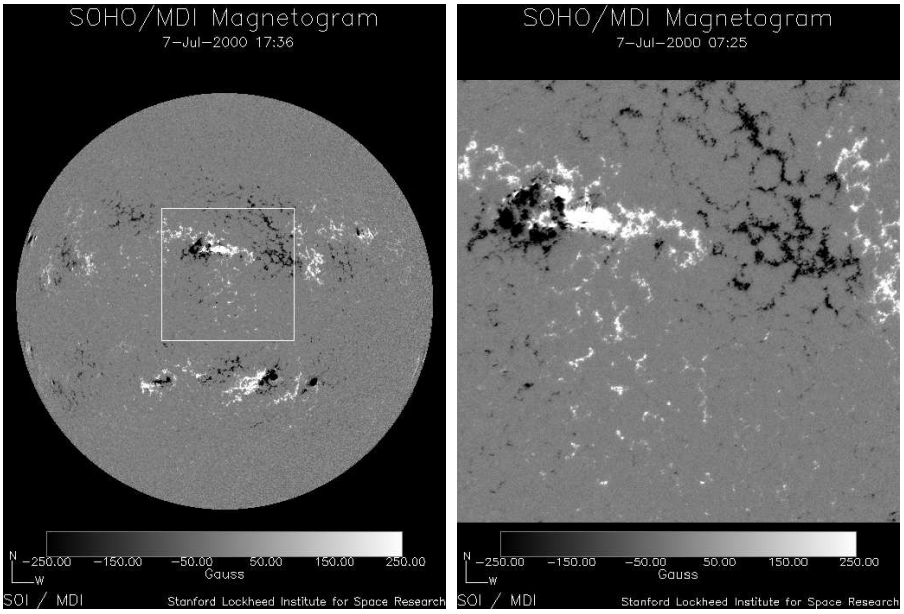

Figure 1.2: SOHO MDI magnetograms. *Left Panel*: full disk magnetogram of the solar photosphere. *Right Panel*: zoom in the square region delimited in the full disk image. In both the images the absolute value of the magnetic field saturates at 250 G.

and a typical lifetime of one day. They don't present any penumbra and they can be thought as an intermediate state between tiny photospheric magnetic flux tubes and complex and large sunspots. The debate on physical mechanisms governing the formation and evolution of solar pores, also in relation with sunspots, is still open. A detailed review on solar sunspots and pores can be found in Sobotka (2003) and Thomas & Weiss (2004).
Sunspots and pores are examples of photospheric magnetic features having quite small spatial extension. By observing the solar photosphere in modern magnetograms, as the one shown in Figure 1.2, it is evident how magnetic fields are distributed all over the solar photosphere. More in detail, bipolar regions (dark and bright in grey scale), named active regions, extend for thousands of kilometers. Strong active regions are typically associated with group of sunspots and pores. When observed in Ca II lines or Hα, active regions appear extremely bright defining plages or faculae. In addition to active regions, the solar photosphere is covered by many magnetic patches forming a sort of net, also defined the magnetic network. This is the result of the concentration of magnetic flux in the boundaries of supergranular cells (Livingston & Harvey 1975), the largest organization scale observable in the

photospheric plasma motion (see the zoom-in panel in Figure 1.2). The origin of these extended active regions can be explained invoking collections of flux tubes formed as fragments of large coherent magnetic entities as sunspots. In this context, the formation of network patches could follow from the debris of the decay of active regions organized by the photospheric plasma motions on supergranular scales.
The magnetic field debris introduced above assume, in the framework of the formation of extended magnetic structures, the role of bricks of the photospheric magnetic fields. The origin of these small-scale fields is not yet fully clarified. It seems plausible that the rise and emergence of magnetic flux from the deep convection zone in the form of small dipoles could justify the existence of such smaller flux tubes as, on the other hand, the effect of a local dynamo acting in the near-surface layers of the Sun (Vögler & Schüssler 2007, and references therein).
These small-scale magnetic fields fill the portion of magnetized photosphere known as the quiet Sun on which we'll focus in the dissertation developed in this thesis (§ 1.2).

In full disk magnetograms like the one in Figure 1.2 a large part of the solar photosphere appears unmagnetized. This large portion of the solar surface is also defined the quiet Sun or internetwork, as it corresponds to the interior of network cells. It is evident that the definition of internetwork is not so solid. In fact, it is not straightforward to distinguish between network and internetwork as the presence or absence of magnetic signals in magnetograms depends on both the sensitivity and spatial resolution of the magnetometer. However, even taking into account this uncertainty, we can state that quiet Sun regions cover about 90% of the solar photosphere, independently of the phase of the 11-years solar cycle (Harvey-Angle 1993). In the following we'll expose how internetwork regions are very far from being unmagnetized and why they have raised enormous interest in the solar community.

1.2 Quiet Sun Magnetism

In spite of the definition given above, nowadays is well known that magnetic fields are present almost everywhere in quiet Sun regions in a spatial intermittent fashion. In fact, modern spectropolarimetric measurements show a not-so quiet Sun, with magnetic fields varying between zero to ~ 2 kG continuously moved and shuffled by photospheric plasma motions acting over timescales of the order of the granulation lifetime (~ 10 min, see Figure 1.3; see e.g., Berrilli et al. 2002; Del Moro et al. 2007). In this scenario, the weak

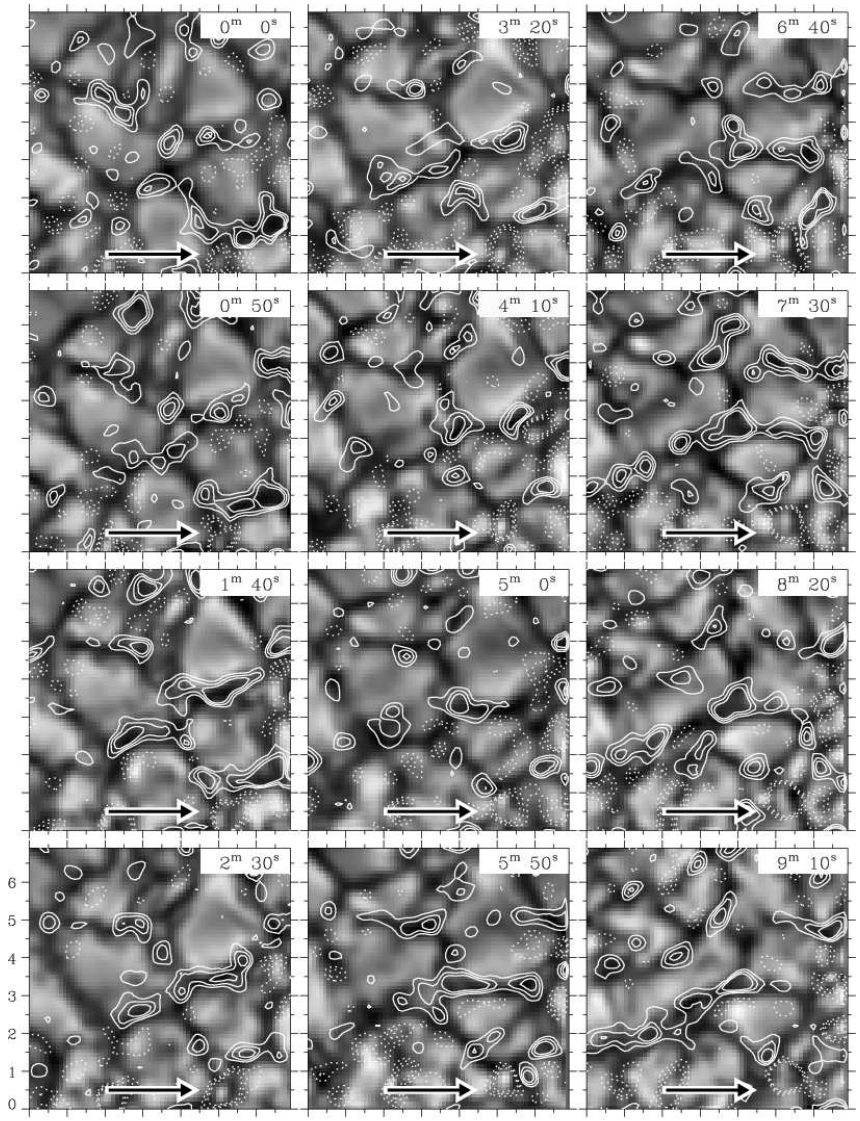

Figure 1.3: Temporal evolution of magnetic fields due to granular motions. Time increases from top to bottom and from left to right. The arrow points out a specific region dominated by a magnetic concentration of negative polarity. Positive polarity fields are represented with solid line while negative polarity fields are represented with dotted line (Domínguez Cerdeña et al. 2003b).

polarization signals measured in internetwork regions, in lines sensible to magnetic fields, can be interpreted as the result of the linear combination of the polarization emerging from discrete magnetic flux tubes, which typically

are smaller than the angular resolution, that fill the solar photosphere with a complex topology imposed by the photospheric plasma motion (e.g., Emonet & Cattaneo 2001a; Sánchez Almeida et al. 2003b).
From the sketch made above follows that the quiet Sun is an extraordinary laboratory to test turbulence and MHD theory under the $\beta > 1$ condition. As an example, it can allow us to test our ideas on the magnetic field generation by convective processes (turbulent dynamo). If this mechanism is actually operating in the Sun, the quiet Sun is the obvious place to look for its signature. This is also a natural step toward understanding the principles of astrophysical dynamos.
Besides, due to its large diffusion onto the solar surface, internetwork magnetic fields can be useful to understand the physics at the base of the overall photospheric magnetism. In fact, the quiet Sun could hold a large fraction of the unsigned flux density and magnetic energy density of the solar photosphere (e.g., Unno 1959; Stenflo 1982; Sánchez Almeida 1998, 2004; Schrijver & Title 2003).
Moreover, the photospheric magnetic field is the base of the magnetic field of the solar chromosphere and corona. For this reason, the quiet Sun is an important starting point to understand the magnetism of the solar upper atmosphere. As an example of the tight connection between the physics of the quiet Sun and the physics of the solar atmosphere we can refer to the "nanoflare hypothesis", formulated by Parker (1988), to justify the heating of the solar corona. He proposed nanoflare energy emissions ($\sim 10^{25}$ erg) due to the dissipation at many tangential discontinuities as a consequence of random continuous motion of the footpoints of the field due to photospheric convection. Recently, Krucker & Benz (1998), using the EUV Imaging Telescope on board of the SOHO satellite, showed that nanoflare energy emissions can be observed in quiet Sun regions and that their statistical properties may justify a sufficient energetic support to heat the solar corona up to $\sim 10^6$ K.

The arguments exposed above are some of the aspects that support the importance of the study of the internetwork in modern solar physics and are also the aspects that will often recur in the whole discussion reported in this thesis. § 1.2.1 and § 1.2.2 have the aim of exposing in detail the results obtained from observations and numerical simulations of quiet Sun regions, respectively.

1.2.1 Observations

Spectropolarimetric observations are the most powerful and promising tool to measure magnetic fields in quiet Sun regions. The interpretation of the

polarized radiation emerging from the magnetized photosphere allows to measure the magnetic field vector generating the polarization. Putting aside the theoretical details of spectropolarimetric techniques applied to the measurements internetwork magnetic fields that will be discussed in Chapter 4, here we focus on the main results obtained from spectropolarimetric observations of quiet Sun regions obtained in the last two decades.

Magnetic fields were detected for the first time in the solar internetwork about three decades ago by Livingston & Harvey (1975) and Smithson (1975). During the past decade, improved instrumentation was designed for the detection of polarization in lines sensible to the magnetic field as Fe I λ15648 and Fe I λ15652 (e.g., Khomenko et al. 2003), Fe I λ6301 and Fe I λ6302 (e.g., Domínguez Cerdeña et al. 2003b,a; Lites 2002) that could be observed combining high polarimetric precision, $\sim 10^{-4}$ the continuum level, and high spatial resolution, up to $0.''5$ (e.g., Domínguez Cerdeña et al. 2003b). Parallely, improved diagnostic techniques based on Hanle depolarization theory (e.g., Stenflo 1982; Faurobert-Scholl 1993; Faurobert-Scholl et al. 1995; Landi degl'Innocenti 1998; Trujillo Bueno et al. 2004; Manso Sainz et al. 2004), Principal Component Analysis (PCA) of polarimetric signals (e.g., Rees et al. 2000; Socas-Navarro et al. 2001; Socas-Navarro & Sánchez Almeida 2002) and appropriate description of solar magnetized atmospheres (e.g., MIcro Structured Magnetized Atmosphere models Sánchez Almeida et al. 1996; Sánchez Almeida 1997; Sánchez Almeida & Lites 2000) allowed to interpret in a brand new way the polarization emerging from the solar photosphere. The advances briefly listed above made it possible to determine some of the internetwork magnetic field properties and, at the same time, to renew the interest of the solar community in the magnetism of the quiet Sun.

The magnetic field strength is one of the key parameters to characterize the internetwork magnetism. The Hanle depolarization signals of photospheric lines are consistent with a turbulent magnetic field occupying most of the observed volume. Although the computed field is a model dependent quantity the estimates based on this technique retrieve a magnetic field strength between zero and 130 G (Stenflo 1982; Faurobert-Scholl 1993; Bianda et al. 1999; Shchukina & Trujillo Bueno 2003; Trujillo Bueno et al. 2004; Bommier et al. 2005).

Despite Hanle depolarization was the first technique applied to measure internetwork magnetic fields, most of the modern measurements are based on the polarization signals produced in spectral lines sensible to the magnetic field via Zeeman effect. Different photospheric lines are known to be sensible to magnetic field, they can be organized in two main groups: lines in the visible spectral range and lines in the infrared spectral range. When measuring the polarization in visible lines, the values of the magnetic fields obtained from

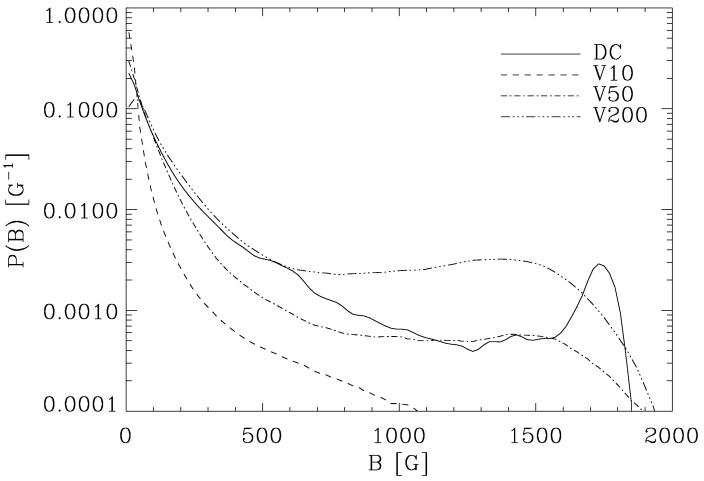

Figure 1.4: Comparison between different PDFs of quiet Sun magnetic fields. The DC line represents a PDF from the combination of Hanle and Zeeman measurements. The other PDFs are produced from from numerical simulations of magnetoconvection by Vögler et al. (2003) imposing initial field strengths of 10 G (V10), 50 G (V50), and 200 G (V200), see § 1.2.2 (Domínguez Cerdeña et al. 2006).

the analysis are found typically in the kG range (Sánchez Almeida & Lites 2000; Socas-Navarro & Sánchez Almeida 2002; Domínguez Cerdeña et al. 2003b,a). On the contrary, measurements based on infrared lines retrieve a dominant role of hectogauss (hG) fields (Lin & Rimmele 1999; Khomenko et al. 2003).

The disagreement between the measurements based on visible and infrared lines, combined with both the Hanle depolarization measurements and the information retrieved by modern numerical MHD simulations (see § 1.2.2), lead to two important conclusions. The first one is that internetwork magnetic fields can vary in a continuous range (Sánchez Almeida & Lites 2000; Trujillo Bueno et al. 2004); moreover, the upper limit of this range is well known and is set at about 2 kG by the pressure equilibrium between flux tubes and unmagnetized photospheric plasma (Parker 1978; Spruit 1979). The second conclusion is that each observation technique is biased towards a certain field strength range that can give just a partial description of the internetwork magnetism.

The parameter typically used for a statistical description is the fraction of photosphere occupied by a certain field strength. This can be translated in

the probability density function (PDF) of the magnetic field strength, $P(B)$, that is an extremely powerful quantity for the description of the global properties of a quiet Sun region. As an example, calculating the first and the second momentum of $P(B)$ gives information about the mean unsigned flux density and the mean magnetic energy density (save for a constant factor $1/8\pi$), respectively.

Lin (1995) computed a PDF for magnetic fields in active regions and quiet Sun regions using Fe I λ15648 and Fe I λ15652 lines while Lites (2002) obtained it from the analysis of network regions and their surroundings using Fe I lines at 6300 Å. Both authors found a bimodal distribution with a dominant contribution at $\simeq$ 150 G and a secondary peak at $\simeq$ 1.5 kG. Conversely, Collados (2001), studying quiet Sun regions using the same infrared lines as Lin (1995), found an exponential decline in the magnetic flux density histogram from a peak at $\simeq$ 200 G and no counts for magnetic flux density greater than 1 kG. Domínguez Cerdeña et al. (2006) worked out a set of PDFs of the quiet Sun magnetic fields consistent with observations and magneto convection simulations by using information from both Hanle and Zeeman observations. In spite of its exploratory character, their work arose a big interest because of a particular property of the functions they obtained: they increase for strong fields, right before the cut-off at $B \simeq 1.8$ kG (see Figure 1.4). This characteristic gives to strong fields a particular relevance because, even if they are present in a small fraction of the photosphere, they dominate the unsigned flux density and magnetic energy density. On the other hand, the magnetic field distributions proposed by Martínez González et al. (2006a,b, 2008), obtained from simultaneous infrared and visible observations of Fe I lines do not present any rise for strong fields. Recent analysis of Fe I lines at 6300 Å, observed with the HINODE, satellite confirms this result (Orozco Suárez et al. 2007).

In an effort to complement the existing spectropolarimetric diagnostic techniques, López Ariste et al. (2002) proposed the use of spectral lines whose Zeeman patterns are sensitive to hyperfine structure (HFS). The formalism to deal with the HFS of spectral lines in magnetic atmospheres was developed more than thirty years ago by Landi degl'Innocenti (1975). According to such formalism, the polarization of the HFS lines vary with magnetic field strength very differently from the lines commonly used in solar magnetometry. This unusual behaviour was invoked by López Ariste et al. (2002) when proposing the use of HFS Mn I lines as a diagnostic tool for magnetic field strengths. López Ariste and coworkers have applied the idea to measure magnetic field strengths in quiet Sun regions using Mn I λ5538 and Mn I λ15263 (López Ariste et al. 2006, 2007; Asensio Ramos et al. 2007). Recently, Ramirez Velez et al. (2008), defined a PDF of internetwork magnetic

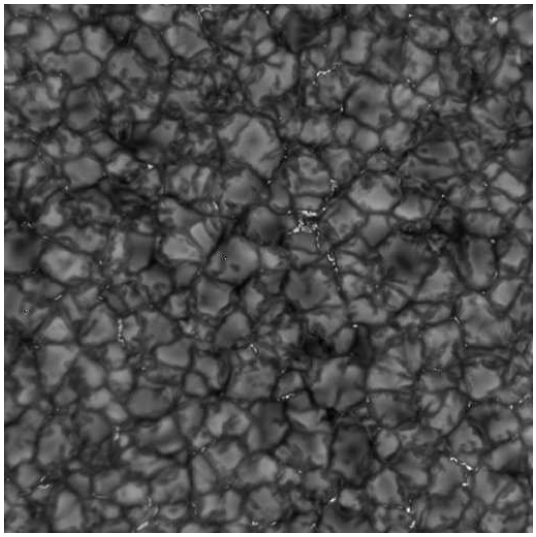

Figure 1.5: G-band bright points in a quiet Sun region. This image has been obtained from G-band images acquired at the Dunn Solar Telescope at Sacramento Peak after Multi Frame Blind Deconvolution reconstruction technique to reach a spatial resolution of about $0''.1$.

fields interpreting Mn I λ5538 and Fe I lines at 6300 Å polarization profiles. The retrieved distribution shows the predominance of weak hG magnetic fields.

Small magnetic features in internetwork regions are related to the so called G-band bright points. The G-band is a 1 nm wide band around $\lambda = 4305$ Å where CH bands are found. In this band there is a strong contrast between kG flux tubes, and the surrounding photosphere due to the dissociation of CH molecules that increases the visibility of the subphotospheric and hot fluxtube walls (for a detailed description of bright points formation see Rutten et al. 2001). Nowadays is well known that bright points correspond to strong kG flux tubes, with spatial extension of $100 - 200$ km, at the limit of resolution of ground-based solar telescopes, and nearly vertical field lines (see the review Solanki 1993).
The first images of magnetic elements identified as discrete bright points were produced between the end of the 80s and the beginning of the 90s (Muller et al. 1989; Auffret & Muller 1991). They can also be observed in groups defining elongated bright features named filigree of bright points (e.g., Dunn & Zirker 1973; Berger et al. 1995) which can be exactly defined as chains of bright features located within the intergranular lanes (i.e., dark region

between photospheric granules associated with downflows), as shown in Figure 1.5.
The dynamics and evolution of bright points have been largely studied (e.g., Muller et al. 1994; Berger & Title 1996; Loefdahl et al. 1998; van Ballegooijen et al. 1998) and all the analysis agree that bright points appear to be passively advected by granulation flows with velocities of the order of 1.5 km s^{-1}. G-band bright points provide a simple and direct way to study the magnetism of the quiet Sun using unpolarized light. More in detail, the presence of bright points strongly suggests that part of the internetwork fields has to be kG fields. As exposed above, spectropolarimetric observations indicate that quiet Sun magnetic fields can vary from zero to kG, but the presence of kG field strengths is still strongly debated. G-band bright points provide an independent proof that strong magnetic fields may play a crucial role in the internetwork magnetism.
The quantitative results derived from observations, based upon different methods, exposed in this chapter seems not to provide yet a fully consistent picture of internetwork magnetic fields. In fact, due to their turbulent nature, with mixed polarities on small spatial scales, their extended range of field strength plus their weak polarization signals consequence of a complex topology, quiet Sun magnetic fields are an extremely difficult observational target. However, what appears to be clear is that small-scale, mixed-polarity magnetic fields are present almost everywhere in the quiet Sun and they contribute in an important way to the total magnetic energy and flux of the quiet photosphere.
In the following section we expose the main results obtained with MHD simulations of quiet Sun regions as support to observation in the description of these ubiquitous fields present in internetwork regions.

1.2.2 MHD Simulations

As already pointed out in § 1.2.1, diagnostic techniques are strongly supported by numerical simulations able to provide an important guidance for the interpretations of the observations by reproducing, in an extremely detailed way, the interaction between magnetic fields and photospheric plasma and the complex field topology which is expected from this interaction, a knowledge critical for a proper interpretation of the observables.
Numerical MHD simulations of small portions of the solar photosphere are a powerful tool to obtain information on the three-dimensional structure of the atmosphere and on the configurations of the magnetic field permeating the atmosphere. Moreover, all these informations are produced with spatial resolutions orders of magnitude above the ones accessible by current observa-

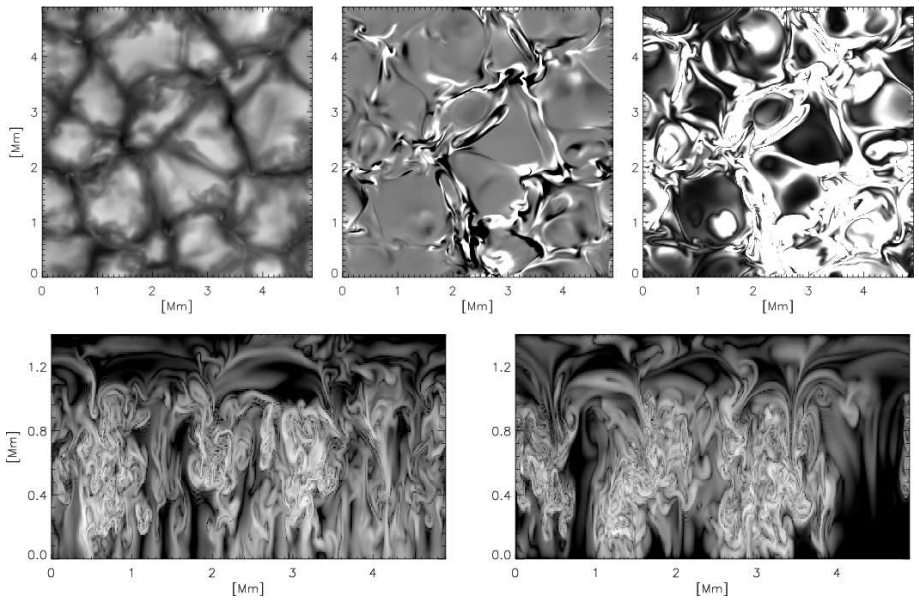

Figure 1.6: Snapshot from the saturated phase of the dynamo. The panels in the upper row show the continuum intensity at 630 nm wavelength (*upper left*), a grey-scale image ("magnetogram", saturated at ±10 G, black and white colour indicating the two polarities) of the (signed) vertical field component on the surface $\tau_{630} = 10^{-2}$, roughly corresponding to the formation height of the spectral line used for the observations (*upper middle*), and the unsigned horizontal field strength (*upper right*), black colour in this panel representing a very weak field and white colour indicating the saturation level of 10 G. The two panels in the lower row show grey-scale images of the logarithm of the horizontal field strength (black colour indicating fields below 1 G) for vertical cuts through the simulation box along a horizontal line at $y = 1.5$ Mm (*left*) and $y = 3$ Mm (*right*), respectively, in the upper panels. The level of $\tau_{630} = 1$ is roughly at a height of 0.9 Mm, the level of $\tau_{630} = 10^{-2}$ at 1.2 Mm (Vögler & Schüssler 2007).

tions, thus providing unique information on the physical processes underlying the observed phenomena. In order to reproduce realistic solar conditions of magneto-convection in the photosphere realistic physics have to be included in simulations, namely, radiative transfer, and partial ionization.
Starting from the pioneering work of Nordlund (1983), several three dimensional MHD simulations of the solar photosphere have been carried out by different authors (e.g., Nordlund & Stein 1990; Bercik 2002; Stein & Nordlund 2003) providing important description of the spatial structure and temporal evolution of magnetic field concentrations in quiet Sun regions. Adopting a different approach, Steiner et al. (1998) and Grossmann-Doerth et al. (1998)

performed two-dimensional simulations of magnetic structures. Despite their geometrical constraints these simulations were able to reach high spatial resolution allowing a more realistic modelling of small-scale magnetic structures. Pursuing the philosophy of more realistic models, Cattaneo (1999), Emonet & Cattaneo (2001b) and Cattaneo et al. (2003) developed models to simulate thermal magneto-convection in the Boussinesq approximation. These simulations pointed out the possibility that an important fraction of the magnetic field of internetwork regions is created locally by dynamo process produced by the convective motions on granular scale. In recent three dimensional simulations Vögler & Schüssler (2007) and Schüssler & Vögler (2008) confirmed this result finding that a dynamo action by near-surface convection contributes significantly to the solar internetwork fields.

As can be easily understood, magneto convection simulations offer a wide variety of PDFs of the quiet Sun magnetic fields to be compared with those obtained from observations described in § 1.2.1. Simulations show, for example, exponential decays (Cattaneo 1999; Stein et al. 2003; Stein & Nordlund 2006; Vögler & Schüssler 2007), bimodal behaviours (Vögler et al. 2003; Vögler & Schüssler 2003) or an "exponential-like core and a modest peak" for $B \sim 1$ kG (Steiner 2003).

As exposed above, modern magneto-convection simulations takes into account the solution of the full compressible MHD equations including elaborate physics and can make clear predictions about the complex processes that take place in the Sun's magnetized atmosphere. A test to verify the realism of simulations can be performed by a direct comparison with observations if typical quantities measured in observations are produced by simulations. As already pointed out, Stokes diagnostics is the main tool to study internetwork magnetic fields. For this reason Steiner et al. (1998), Grossmann-Doerth et al. (1998) and Steiner (1999) included in their code a set of routines providing synthetic Stokes profiles and continuum intensity diagnostics producing polarization signals in full agreement with the ones observed by Sigwarth et al. (1999). Further synthesis of polarization profiles were produced by Sánchez Almeida et al. (2003b) using MHD simulations of Cattaneo (1999) and Emonet & Cattaneo (2001b). Recently, Khomenko et al. (2005) and Shelyag et al. (2007) proposed extremely detailed works on the Stokes diagnostics produced by solving the radiative transfer equation in unidimensional atmosphere produced by Vögler et al. (2003, 2005) (see Figure 1.6). The results obtained by Khomenko et al. (2005) and Shelyag et al. (2007) confirm the high degree of realism of modern simulations and open a wide field of investigation based on synthetic Stokes diagnostic extremely powerful also to test diagnostic techniques usually applied with blind faith to observed polarization profiles.

Chapter 2

Dynamic Models of Quiet Sun Magnetism

As already exposed in § 1.2, the study of quiet Sun magnetic fields is strongly supported by realistic MHD simulations. These allow to study quite small portions of solar photosphere with typical spatial scales of $\sim 10^3$ km (hereafter 10^3 km=1 Mm) along the two or three spatial dimensions with spatial resolutions of few tens of kilometers (e.g., Grossmann-Doerth et al. 1998; Steiner et al. 1998; Cattaneo et al. 2003; Vögler & Schüssler 2007; Schüssler & Vögler 2008).
The computational cost required to run such simulations is conspicuous. In fact, MHD equation system combined to the equation of state, to describe the relations between the thermodynamical quantities of the fluid, and the radiative transfer equation, to model the energy exchange between gas and radiation, have to be solved. This results in a time consuming task even for high performance machines dedicated to calculus.
As a consequence, to simulate a large computational domain including, for example, a high number of granules is mandatory the use of simplified models.
The following sections of this chapter have the aim of illustrating a simplified model we developed with the intent of reproducing some of the statistical properties of quiet Sun magnetic fields arising from the interactions between small-scale flux tubes and the abvection flow of the photospheric plasma, in a photospheric region four times wider than the one studied in the most recent MHD simulations from Vögler & Schüssler (2007) and Schüssler & Vögler (2008), demanding minor computational costs.
We start the description of the model from the key ingredient: the photospheric advection field based on the model proposed by Rast (2003) which will be used as the driving force of our small-scale magnetic fields whose evolution rules will be exposed in § 2.2.

2.1 Photospheric Velocity Field

The photospheric velocity field is modelled on the basis of the simulation developed by Rast (2003). The horizontal flow is computed through an n-body simulation; the model renders the interaction between downflow plumes by considering only their mutual horizontal advection. The movement of a plume is defined by its advection by all the other plumes. The introduction of new downflows is simplified by imposing the conservation of the total flow and by considering the injection sites to be randomly distributed over the domain. Specifically, our synthetic velocity field is computed on a $L \times L$ domain ($L = 256$ pixels) with periodic boundary conditions. The velocity field is defined by the sum of all plume advection profiles in the domain, and the single advection profile is described by an exponential law (Rast 1998) with a characteristic decay length (σ) that is a free parameter of the model. The radial profiles are truncated at half a domain width.
At the beginning of the simulation, $n(t_0)$ randomly located plumes with profile amplitudes normally distributed around 1 (FWHM=0.5) are introduced into the domain to act as initial attraction seeds. The amplitudes of all profiles decay exponentially with a characteristic decay time $\tau = 10$ (this statement sets a granular lifetime), and a plume is removed from the domain when its amplitude is less than 10^{-3}. Each plume is advected by the vector sum of all other plume profiles computed at its position. Two plumes merge when they are within 1 pixel of each other, creating a new plume profile located in the same position as the strongest one, with an amplitude equal to the sum of the amplitudes of the merging plumes. We force the simulation to conserve the total flow F, defined as the sum over all plume amplitudes, at any time t. Therefore, during the simulation, we add new randomly located plumes to counterbalance the temporal decay, again with an amplitude normally distributed around 1 (FWHM=0.5).
The time of the simulation at the $(k+1)th$ evolution step is defined by

$$t_0 = 0 \tag{2.1}$$

and

$$t_{k+1} = t_k + \frac{r_{min}(t_k)}{v_{max}(t_k)} \tag{2.2}$$

where $r_{min}(t_k)$ is the minimum among all the distances between plumes and $v_{max}(t_k)$ is the maximum among all plume velocities, at time t_k.

Typically, for $\sigma = 20$ pixels, the simulation produces few (one or two) stable plumes sustained by the merging of elementary granular downflows,

while for $\sigma = 5$ pixels, the system is not able to sustain stable and strong plumes. In order to tune the model so as to reproduce the spatial correlations that are present in the photospheric plasma flows (i.e., granulation and mesogranulation scales), we performed several runs spanning different values in the $\sigma - F$ parameter space. The simulations that produced the correct spatial correlations were obtained for values of $F = 1000$ and $\sigma = 10$ pixels (see Figure 2.1). Therefore, we expect granular structures in our simulation to have a scale of about $2\sigma = 20$ pixels. This sets our length unit to be 1 pixel= 0.05 Mm.
The validity of this choice for σ and F has been supported by the hexagonal normalized information entropy analysis (Berrilli et al. 2005) of the photospheric velocity field patterns. This analysis provides a very sensitive measure of the length scales over which structures are present in a system. We studied an ensemble of 100 simulations to compute the hexagonal information entropy and hence measure the spatial scales of downflow organization. We found two scales at which the system organizes itself: the first is $l_G \simeq 1$ Mm consistent with granulation; the second one, with 82 pixels corresponding to $l_M \simeq 4$ Mm, is associated with strong and stable downflows and is representative of mesogranulation. The ratio between mesogranular and granular scale lengths $l_G/l_M \simeq 4$ is in agreement with observations (e.g., Roudier et al. 1998; Domínguez Cerdeña 2003; Del Moro 2004). It is worth noting that the timescales over which the simulated mesogranular patterns organize, are comparable to the imposed lifetime of granular flows. A similar behaviour has been observed in a photospheric data set obtained at the NSO-Dunn telescope (Berrilli et al. 2005), where timescales over which mesogranular features emerge are comparable to granulation timescales.

We can summarize the results exposed in this section saying that the photospheric velocity field obtained from the n-body simulation, implementing only the mutual horizontal interactions between granular downward plumes, self-organizes itself in a way that creates mesogranular time-stable and intense plumes. The spatio-temporal correlations obtained are in agreement with the ones exhibited by the plasma motion in the photosphere (i.e., granulation and mesogranulation).

2.1.1 Nanoflare Statistical Properties

The first application of the n-body velocity field described in § 2.1 was proposed in Viticchié et al. (2006) as part of a dynamic model for the study of the statistical properties of nanoflare energetic events in internetwork re-

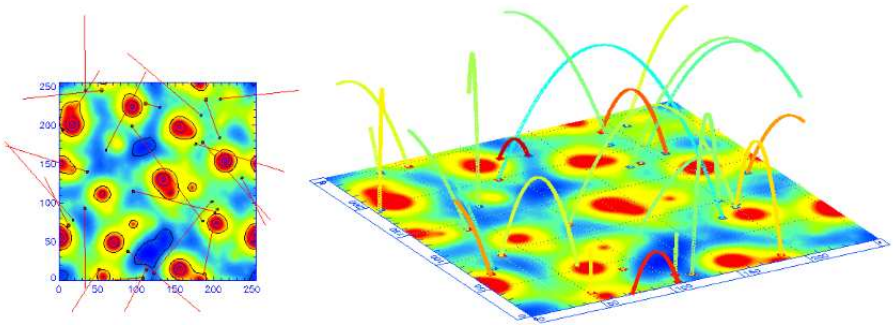

Figure 2.1: Magnetic loops driven by the photospheric velocity field computed for $\sigma = 10$ pixel. *Left panel*: a snapshot of a simulation run as seen from above. Intense and stable mesogranular downflows are qualitatively represented as large circular red spots. Solid lines represent the projections of magnetic loops on the $L \times L$ domain. *Right panel*: The same simulation seen from a different angle. The loop colour is indicative of the associated magnetic energy (Viticchié et al. 2006).

gions; two snapshot images of the model are shown in Figure 2.1. We report here just a brief description of the main results obtained from this application with the intent of pointing out how powerful can be such a simple approach to the description of an extremely complex system as the quiet Sun magnetic field.

In Figure 2.1 is represented the geometry of the magnetic field simplified by considering semicircular loops anchored to a pair of footpoints on the $L \times L$ photosphere domain. Starting from a random configuration of the loops, footpoints are passively advected by the photospheric velocity field; their movement drives the magnetic loops over the $L \times L$ domain and this can cause loops to interact and release energy.

We skip here the description of the details of the magnetic loop system (see § 2.2 in Viticchié et al. 2006) to focus on the results retrieved by the model. In Figure 2.2 the value $E_{\rm M}(t)$ of the total magnetic energy, as a function of time t, for a typical simulation is represented. From this we can calculate the magnetic energy emission of synthetic flares, as a function of time, by calculating the difference $E_{\rm M}(t_{\rm k-1}) - E_{\rm M}(t_{\rm k})$ between two subsequent steps; the energy emission, as function of time, are also reported in Figure 2.2.

By performing eight simulation runs, each one corresponding to $\simeq 600$ min of photospheric evolution, we produced a total of $\simeq 40000$ energy emissions, i.e. synthetic flares. The statistical analysis, over all simulations, of the released magnetic energy yields the relative frequency function presented in Figure 2.3. This function is well approximated by a power-law over three

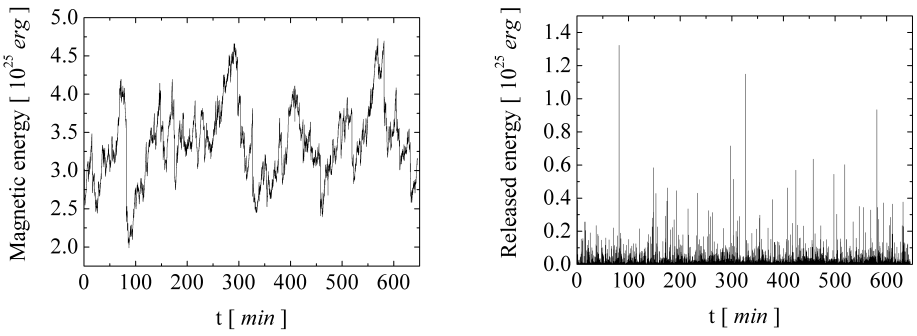

Figure 2.2: *Left panel*: time series of the total magnetic energy of the system for a typical simulation (Viticchié et al. 2006). *Right panel*: time series of the released magnetic energy for the simulation reported in the *left panel* (Viticchié et al. 2006).

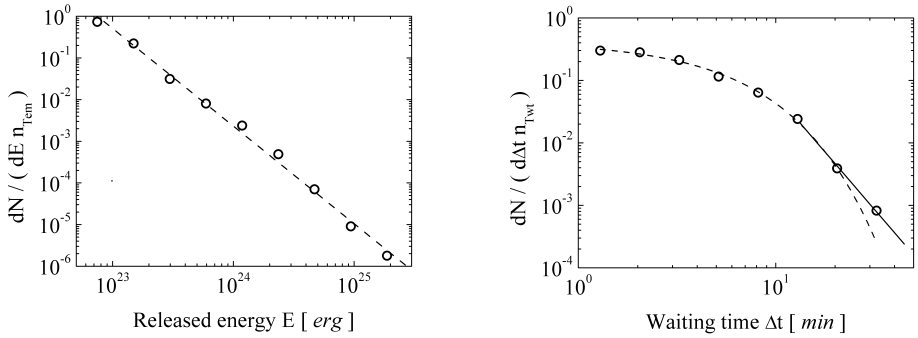

Figure 2.3: *Left panel*: relative frequency function for the released magnetic energy computed from all simulation runs (open circles) and power-law fit for the distribution (dashed line). n_{Tem} in the axis label is the total number of emissions over which the statistics is calculated. The resulting power-law index is $\alpha = 2.4 \pm 0.1$ (the error is given by the standard deviation of the linear fit). *Right panel*: Relative frequency function for waiting times between emissions computed from all simulation runs (open circles). n_{Twt} in the axis label is the total number of time intervals over which the statistics is calculated. Poisson fit for the distribution (dashed line) and linear fit on last three points (solid line) (Viticchié et al. 2006).

decades; the resulting power-law index is $\alpha = 2.4 \pm 0.1$ (the error is given by the standard deviation of the linear fit). Similar power law distributions have been obtained by shell models (Bohr et al. 1998; Boffetta et al. 1999) and by Cellular Automata models (Vlahos et al. 2002; Fragos et al. 2004). Although the energy range explored by Fragos et al. (2004) lies just outside

our upper limit, the power-law seems to blend almost seamlessly.
In Figure 2.3, also the waiting time distribution for the whole dataset is reported. The instantaneous nature of the simulated reconnection processes avoids the uncertainty on the separation of high-energy events (Buchlin et al. 2005). We found that for longer waiting times, waiting time $\geq$ 10 min in our simulations, the statistics moves from Poisson-like to a power-law distribution behaviour.
The computed distribution, with power-law index $\alpha = 2.4 \pm 0.1$, extends over three decades ($10^{23} - 10^{26}$ erg); this energy range is typically connected to the nanoflare energy interval. The computed index is in excellent agreement with nanoflare statistics by Krucker & Benz (1998) and Parnell & Jupp (2000), thus supporting the hypothesis that nanoflares could be decisive for the process of chromospheric and coronal heating, as stated by Hudson (1991). The statistics of waiting times between nanoflares, which extends over two decades, changes, for longer waiting times, from Poisson-like to a power-law distribution behaviour. We wish to emphasize that this model correctly reproduces the observed distributions for both the released magnetic energy and waiting times, whereas classical SOC models do not yield a power-law tail for the waiting time distribution and shell models ignore the details of the spatial structures and their associated topology (Bohr et al. 1998).
The model yields a fairly intuitive interpretation of magnetic reconnections as field reconfigurations triggered by the passive advection of footpoints through spatially and temporally correlated flows in the photosphere.

2.2 Photospheric Magnetic Elements

The magnetic part of the model regulates the dynamics and the evolution of photospheric magnetic elements driven by the photospheric velocity field described in § 2.1 already used in the nanoflare model briefly exposed in § 2.1.1.
Once the velocity field has reached the stationary behaviour, i.e. after the onset of mesogranular scale flows, the time t_k is set to zero and $m = 500$ magnetic elements are distributed at random positions over the $L \times L$ computational domain. The magnetic elements have an associated field strength $B_{in} = 30$ G with random orientation (± 1) and size equal to the spatial resolution element (1 pixel= 0.05 Mm) so that the total flux density is set around zero. Hereafter B stands for the absolute value of the magnetic field strength. We choose such a value for B_{in} since it is approximately the minimum mag-

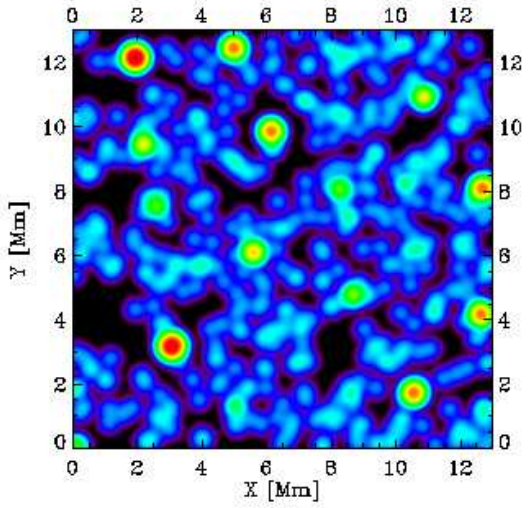

Figure 2.4: Illustrative representation of $|B|$ on the computational domain. Black areas represent daG regions; blue and sky-blue represent daG regions; green represents hG regions; yellow and red represent $\sim$ kG magnetic concentrations. The position of concentrations with $B \sim$ kG correspond to the position of stable downward plumes organized over mesogranular scales.

netic flux density measurable nowadays (e.g., Bommier et al. 2005; Carroll & Kopf 2008).

We let the magnetic elements be passively transported by the photospheric velocity field toward different plume sites. At each plume site, a certain number of magnetic elements converge under the action of the advection field. When two magnetic elements, with associated B_1 and B_2, overlap in the same resolution element, they can produce the following two evolutions:

1. If the two elements have opposite orientation, they are substituted by a new magnetic element in the same site with an associated $B = |B_1 - B_2|$ and the orientation of the strongest. The total flux is conserved so the spatial size of the new element is still one resolution element. In the particular case of $B_1 = B_2$ the elements just cancel each other.

2. If the two elements have the same orientation, they are substituted by a new magnetic element in the same site with an associated $B = B_1 + B_2$ and the same orientation. Again, the total flux is conserved and the spatial size of the new element is one resolution element. This process implicates an amplification of the magnetic field strength.

Different mechanisms have been proposed to concentrate magnetic fields in quiet Sun regions up to the kG range (e.g., Weiss 1966; Parker 1978; Spruit

1979; Sánchez Almeida 2001). Besides, as reported in Sánchez Almeida (2007), all the mechanisms abruptly die out at the maximum field strength imposed by the gas pressure of the quiet Sun photosphere. Therefore, we impose that the amplification process cannot create field strengths greater than $B_{lim} = 2$ kG. B_{lim} can be interpreted as a typical value representative of the maximum field strengths for quiet Sun regions (e.g., Parker 1978; Spruit 1979; Grossmann-Doerth et al. 1998; Steiner 2003; Domínguez Cerdeña et al. 2006; Sánchez Almeida 2007). In detail, whenever the amplification process would produce $B > B_{lim}$, the magnetic elements do not interact and are kept separated.

We implicitly consider that the amplification mechanism is operating on the same time scales as the granulation timescale ($\sim$ 10 min). This hypothesis is consistent with the amplification timescales reported in Parker (1978) and Grossmann-Doerth et al. (1998). In fact, the amplification up to the equipartition value of about 500 G can be ascribed to the granular flows and 5 min are sufficient to produce kG fields from a uniform distribution of 400 G.

To simulate the emergence of new magnetic elements on the solar surface, we continuously add randomly located elements with random orientation and B_{in} magnetic field strength. This injection process maintains the total number of magnetic elements $\simeq m$ compensating the reduction of the total number due to the concentration process.

As proposed by Steiner (2003), starting from an initial PDF $P_{t=0}(B) = \delta(B - B_{in})$, the amplification process will broaden the PDF and extend it up to B_{lim}.

Figure 2.4 shows an illustrative representation of a snapshot of the simulation in the stationary regime. More in detail, we represent the $|B|$ pattern emerging on the computational domain.

2.3 PDF of Field Strengths

In order to derive a representative PDF of the quiet Sun magnetic field strengths we performed ten simulation runs with different advection fields and different initial distribution for the magnetic elements. Each simulation mimicks the evolution of the quiet Sun for an equivalent time of about 2600 min. We analyzed the behaviour of the model by defining the average maximum field strength $max(B)$, the mean unsigned flux density $\langle B \rangle$, and the mean magnetic energy density $\langle B^2 \rangle / 8\pi$, as functions of the mean evolution time t:

$$< B >= \int_0^{B_{lim}} B \cdot P(B) dB, \tag{2.3}$$

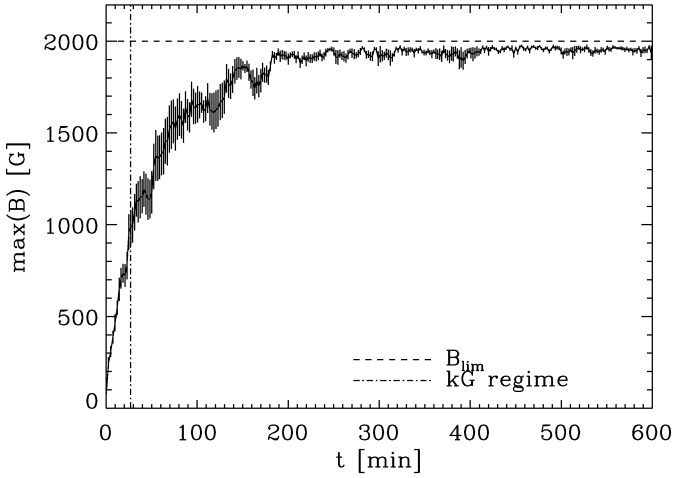

Figure 2.5: Average maximum field strength vs. the evolution time t. The function is obtained averaging the results from $n_{RUN} = 10$ distinct simulation runs and the error bars are calculated as $\frac{\sigma}{\sqrt{n_{RUN}}}$. The horizontal dashed line represents the maximum value allowed for the magnetic flux density (B_{lim}), while the vertical dot-dashed line indicates the instant at which the model produces the first kG elements. The plot shows only a part of the total time domain ($t \simeq 2600$ min).

$$< B^2 >= \int_0^{B_{lim}} B^2 \cdot P(B) dB, \tag{2.4}$$

similarly to Domínguez Cerdeña et al. (2006).
The model creates magnetic concentrations with $B = 1$ kG in about 30 min and $B \simeq B_{lim}$ in about 200 min (Figure 2.5). Figure 2.5 shows that the time scale over which kG fields are produced is $\simeq 30$ min. This is the same time scale over which the mesogranular pattern emerges in the numerical simulation (Viticchié et al. 2006). Different descriptions of the magnetic amplification process (Grossmann-Doerth et al. 1998; Sánchez Almeida 2001) obtained similar results: weak magnetic field structures, standing in a downflow environment, develop field strengths $\sim$ kG in a few minutes. As well, Berrilli et al. (2005) reported that the organization of structures on mesogranular boundaries is very fast, with a typical time scale of $\simeq 10$ min.
Furthermore, the analysis of the position of strong field magnetic elements in our simulation reveals that these are superposed onto stable downward plumes at mesogranular scale (Figure 2.4). Such a correlation between strong magnetic fields and the mesogranular advection scale is in agreement with Domínguez Cerdeña (2003), who found a correlation between mesogranular

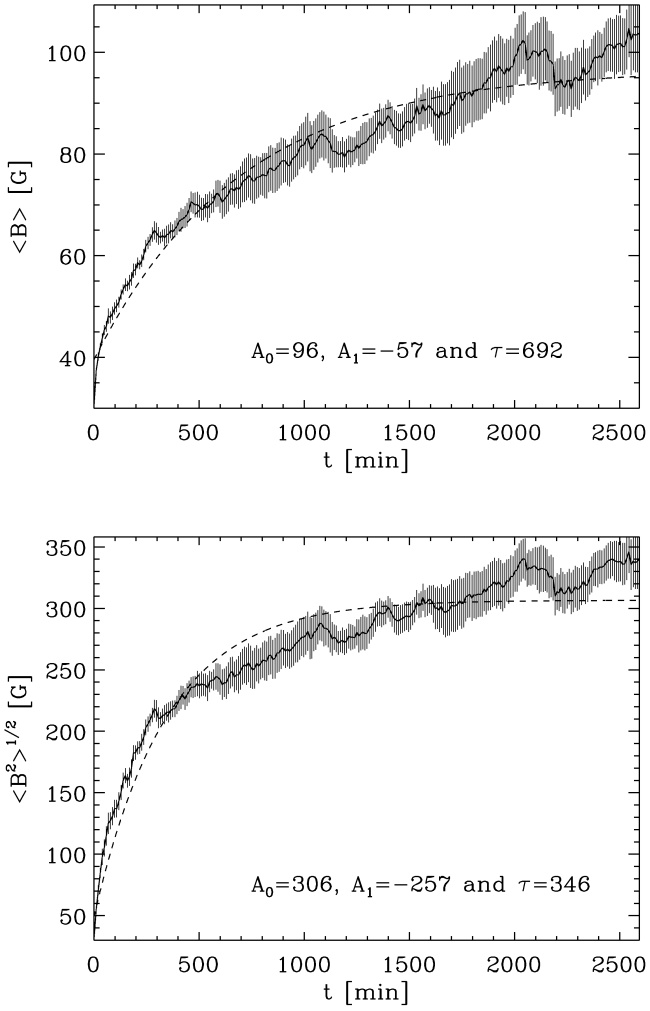

Figure 2.6: Average $\langle B \rangle$ (*upper panel*) and $\langle B^2 \rangle^{1/2}$ (*lower panel*) vs. the evolution time t. The functions are obtained averaging the results from $n_{RUN} = 10$ distinct simulation runs and the error bars are calculated as $\frac{\sigma}{\sqrt{n_{RUN}}}$. The dashed lines represent the $A_0 + A_1 e^{-t/\tau}$ fit performed with the parameters reported in both plots, respectively.

photospheric flows and the pattern observed in magnetograms.
As discussed in § 2.2, we expect to obtain a PDF spanning the entire domain $B = 0 - B_{lim}$. For this reason, the stationary regime must be identified referring to the integral properties of the PDF (i.e., the mean unsigned flux density and the mean magnetic energy density, as defined in Eqs. 2.3 and 2.4).

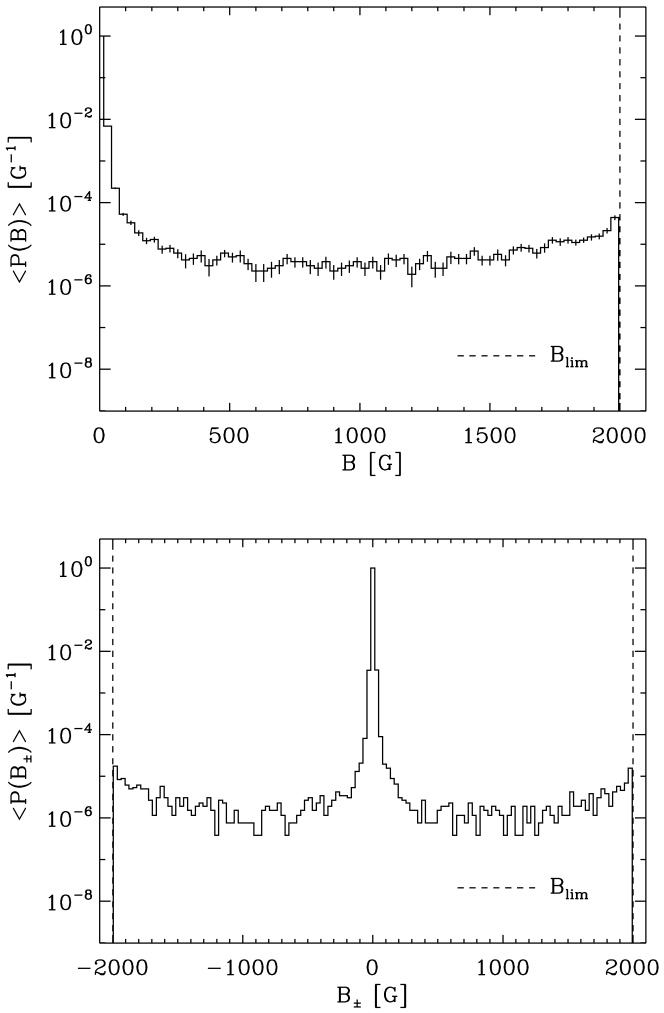

Figure 2.7: *Upper panel*: mean probability density function $\langle P(B)\rangle$ for the magnetic field strength in the stationary regime. $\langle P(B)\rangle$ has been obtained averaging $n_{TOT} = 40$ non-correlated PDFs and the error bars are calculated as $\frac{\sigma}{\sqrt{n_{TOT}}}$. The histogram bin-size is 30 G. The dashed line represents the upper limit for the magnetic amplification process B_{lim}. The maximum at $B = 0$ G is produced by the fraction of the domain free of magnetic elements. *Lower panel*: Mean probability density function $\langle P(B_{\pm})\rangle$ for the signed magnetic field strength in the stationary regime. The histogram bin-size is 30 G. The vertical dashed lines represent the upper and lower limits for the magnetic amplification process $\pm B_{lim}$. The maximum at $B = 0$ G is produced by the fraction of the domain free of magnetic elements.

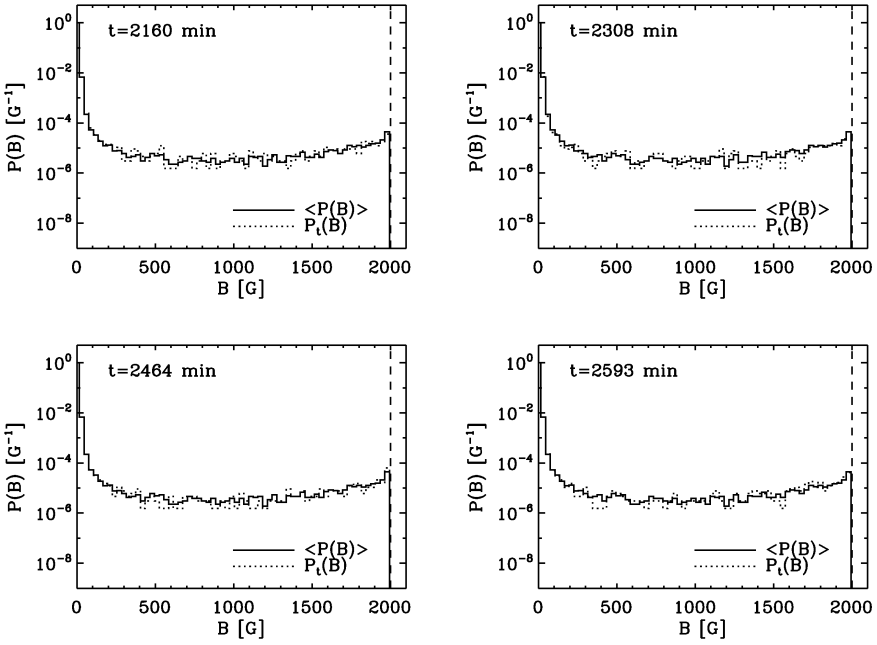

Figure 2.8: Mean probability density function $\langle P(B)\rangle$ (solid line, same as Figure 2.7) compared with four $P_t(B)$ (dotted lines) calculated at different instants of the simulation. Each $P_t(B)$ is the mean of ten PDFs from ten simulation runs at time t. *Top left*: $t = 2160$ min, *top right* $t = 2308$ min, *bottom left* $t = 2464$ min and *bottom right* $t = 2593$ min. The histogram bin-size is 30 G. The vertical dashed lines represent the upper and lower limits for the magnetic amplification process $\pm B_{lim}$. The maximum at $B = 0$ G is produced by the fraction of the domain free of magnetic elements.

$\langle B\rangle$ and $\langle B^2\rangle$ saturate exponentially at $\langle B\rangle_{sat} \simeq 100$ G and $\langle B^2\rangle_{sat}^{1/2} \simeq 350$ G, respectively (Figure 2.6). We interpret such a saturation as an indication that the whole system has reached the stationary regime ($t \gtrsim 2000$ min).
Once in this regime, we compute $\langle P(B)\rangle$ by averaging forty non-correlated PDFs. The computed $\langle P(B)\rangle$ is shown in Figure 2.7. Alternatively, we can compute the mean probability density function $\langle P(B_\pm)\rangle$ for the signed magnetic field strength taking into account the direction of the magnetic fields (also shown in Figure 2.7). As expected, the $\langle P(B_\pm)\rangle$ is rather symmetric with respect to zero.
To verify that the stationary regime has been reached, we compare the $\langle P(B)\rangle$ with four mean PDFs, $P_t(B)$, representative of four different instants of the simulation during the stationary regime (Figure 2.8). More in detail,

each $P_t(B)$ is the mean of ten PDFs at time t. We consider the four $P_t(B)$ to be non-correlated because they are separated by more than 140 min, a time span longer than three times the mean mesogranular lifetime. As shown by Figure 2.8, the deviation between the $\langle P(B)\rangle$ and the four $P_t(B)$ shows no time dependence and the root mean square deviations of all four $P_t(B)$ with respect to the $\langle P(B)\rangle$ are of the order of one part in a thousand.

The values $\langle B\rangle_{sat} \simeq 100$ G and $\langle B^2\rangle_{sat}^{1/2} \simeq 350$ G, reached in the stationary regime, are in good agreement with Domínguez Cerdeña et al. (2006). The percentages of unsigned flux density and magnetic energy density for $B \geq 700$ G are $\simeq 65\%$ and $\simeq 97\%$ respectively, indicating a dominant role for kG fields. The percentages we found are greater than the ones reported by Domínguez Cerdeña et al. (2006); these differences can be explained by referring to the steeper decrease of the $\langle P(B)\rangle$ in the $0-700$ G interval with respect to the log-normal trend found by the authors (see Figure 1.4).

The symmetry of the $\langle P(B_{\pm})\rangle$, reported in Figure 2.7, confirms the equal probability of having concentrations with positive and negative direction. This stems from both the assumptions on the starting configuration and the new element addition criteria during the evolution. Similar symmetries have been obtained in recent simulations (e.g., Vögler & Schüssler 2007) and found in observations of Martínez González et al. (2006a, 2008). In the latter works the authors pointed out that such a symmetry may have deep implications: it may indicate a local dynamo origin for the internetwork magnetic field, i.e., a magnetic field controlled by solar granulation.

The $\langle P(B)\rangle$ presents a maximum for B_{in} in agreement with Domínguez Cerdeña et al. (2006). This result stems from the injection value for the magnetic field strength $B_{in} = 30$ G. At $B \simeq B_{lim}$ the PDF presents a secondary maximum, as found by Steiner (2003), Domínguez Cerdeña et al. (2006) and Sánchez Almeida (2007).

The sharp count decay found at $B = B_{lim}$ is obviously due to the "interaction turn off" imposed at B_{lim} (§ 2.2). Other PDFs reported in the literature show a smooth decay of the peak for $B \simeq 1.8$ kG (Domínguez Cerdeña et al. 2006; Sánchez Almeida 2007), as can be expected in natural PDFs. We could reproduce such a smooth decay for the $\langle P(B)\rangle$ for $B \gtrsim B_{lim}$, by modifying the magnetic element interaction probability, but it is not among the targets of this work to reproduce such a detail of the PDF.

In analogy with Sánchez Almeida (2007), we can state that the secondary maximum in the $\langle P(B)\rangle$ can be interpreted as a consequence of the upper limit imposed to the amplification process at B_{lim}. In fact, when a magnetic amplification process operates, and a limit to this process is set, a pile up around the limit imposed is expected. All the assumptions of the

model contribute in shaping the $\langle P(B) \rangle$: the strong convergence regions of the granular advection pattern create suitable conditions to amplify the magnetic field and, at the same time, support the amplification process by gathering new magnetic elements to also counteract the cancellation process. The secondary maximum of the PDF follows from both the spatial and temporal correlations of the velocity field advecting the magnetic elements and the upper limit of the amplification process at B_{lim}.

Chapter 3

Spectropolarimetry

3.1 Stokes Parameters

Light can be described by means of oscillations of electric field and magnetic field vectors in a plane orthogonal to its propagation direction ($\vec{\Omega}$). Known the relation between these two vectors and the propagation direction, $\vec{B} = \vec{\Omega} \times \vec{E}$, the electric field can provide an exhaustive representation of these oscillations as:

$$E_1(t) = \mathcal{E}_1 e^{-i\omega t},\ E_2(t) = \mathcal{E}_2 e^{-i\omega t}, \tag{3.1}$$

where $\mathcal{E}_1$ and $\mathcal{E}_2$ are complex constants defined as:

$$\mathcal{E}_1 = A_1 e^{i\phi_1},\ \mathcal{E}_2 = A_2 e^{i\phi_2}. \tag{3.2}$$

The constants in Eq. 3.2 contain the information about the amplitude (A_1 and A_2) and the phase (ϕ_1 and ϕ_2) of the oscillations of the projections of the electric field along the orthogonal axes $\vec{e}_1$ and $\vec{e}_2$ ($\vec{e}_1 \perp \vec{e}_2 \perp \vec{\Omega}$).
By imposing the values of the phases so that $\phi_1 = \phi_2$ one obtain, for example, a linear oscillation of $\vec{E}$ fully described by the values of A_1 and A_2. Differently, by imposing $\phi_1 - \phi_2 = \pm\pi/2$ and $A_1 = A_2$ one obtain a circular oscillation of the same vector. In the most general case, the oscillation can be defined as elliptical (see Figure 3.1) with the polarization described by the polarization ellipse parameters: minor axis b, major axis a, and the angle χ. It can be easily shown that the properties of the polarization ellipse are related to $\mathcal{E}_1$ and $\mathcal{E}_2$ by the following quantities:

$$\begin{aligned}
P_I &= \mathcal{E}_1^* \mathcal{E}_1 + \mathcal{E}_2^* \mathcal{E}_2 = A_1^2 + A_2^2, \\
P_Q &= \mathcal{E}_1^* \mathcal{E}_1 - \mathcal{E}_2^* \mathcal{E}_2 = A_1^2 - A_2^2, \\
P_U &= \mathcal{E}_1^* \mathcal{E}_2 + \mathcal{E}_2^* \mathcal{E}_1 = 2A_1 A_2 \cos(\phi_1 - \phi_2), \\
P_V &= i(\mathcal{E}_1^* \mathcal{E}_1 - \mathcal{E}_2^* \mathcal{E}_2) = 2A_1 A_2 \sin(\phi_1 - \phi_2),
\end{aligned} \tag{3.3}$$

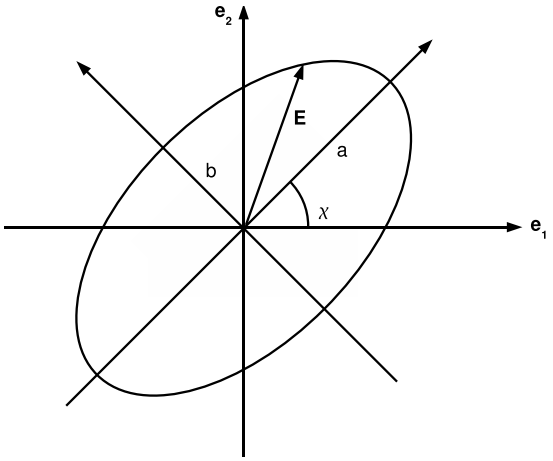

Figure 3.1: Polarization ellipse defined by the electric field vector ($\vec{E}$) in the plane $\vec{e}_1, \vec{e}_2$. The angle χ is the angle between the ellipse major axis (a) and $\vec{e}_1$.

where the asterisk means the complex conjugate, as

$$\begin{aligned} a &= \frac{1}{2}[\sqrt{P_I - P_V} + \sqrt{P_I + P_V}], \\ b &= \frac{1}{2}[\sqrt{P_I - P_V} - \sqrt{P_I + P_V}], \\ \tan(2\chi) &= \frac{P_U}{P_Q}. \end{aligned} \tag{3.4}$$

In the realistic case of $A_1(t)$, $A_2(t)$, $\phi_1(t)$ and $\phi_2(t)$ slowly varying with time[1], the definitions of the quantities in Eq. 3.3 are still valid by using the following temporal averages:

$$\langle \mathcal{E}_i^* \mathcal{E}_j \rangle = \left\langle A_i(t) A_j(t) e^{-i[\phi_i(t) - \phi_j(t)]} \right\rangle . \tag{3.5}$$

Eqs. 3.3 and 3.5 show that the components of the tensor $\mathcal{E}_i^* \mathcal{E}_j$ are the quantities needed to describe the polarization of light.
Finally, from Eq. 3.3 we can define the Stokes parameters as $I = kP_I$, $Q = kP_Q$, $U = kP_U$, $V = kP_V$, where k is a dimensional constant which depends, for example, on the instrument used to measure the polarization.
Before explaining, in the § 3.2, which is the physical process that produces the polarization signals we are interested in, we want to make here a simple explicatory consideration. In our work we'll analyze only Stokes I and V polarization signals emerging from quiet Sun regions. As we'll show in the following

[1]Varying with a typical time $\tau \ll 2\pi/\omega$

sections, Stokes I is the commonly used intensity of radiation, while Stokes V is the parameter carrying information about the circular polarization of light. This can be shown referring to Eq. 3.4 imposing $P_V = 0 \Leftrightarrow V = 0$; in this way, with $b = 0$, the polarization ellipse degenerates on its major axis in a linear polarization state. From this it is easy to understand that the Stokes V parameter it's a measure of the degree of circular polarization of the light.

3.2 Zeeman Effect

Spectral lines in stellar atmospheres are produced by the transition between two levels of an atom (or ion, or molecule). The energy gap between these to levels define the frequency of the absorbed photons causing, at that frequency, a reduction of the mean free path of the photons producing that these escape from higher and cooler layer in the atmosphere. This mechanism manifest itself in Stokes I absorption lines observed at the frequency of the atomic transition.
The atomic levels involved in a transition are usually completely described by the quantum number J where $\vec{J} = \vec{L} + \vec{S}$, with $\vec{L}$ the total orbital angular momentum, and $\vec{S}$ the total electron spin. This picture can change in presence of a magnetic field as happens in the solar photosphere. The magnetic fields filling the atmosphere break the isotropy of the space so that the atomic levels have to be described by the projection of $\vec{J}$ along $\vec{z}$, typically imposed to be parallel to $\vec{B}$; the projection of $\vec{J}$ along $\vec{B}$ is named M.
The complete explanation of the Zeeman effect is provided by the quantum mechanics by adding to the non-perturbed atomic hamiltonian ($\mathcal{H}$) a magnetic hamiltonian defined as:

$$\mathcal{H}_0 = \mu_0(\vec{L} + 2\vec{S}) \cdot \vec{B}. \tag{3.6}$$

with $\mu_0 = \hbar e_0/2mc$ the Bohr magneton.
The perturbation of this term to $\mathcal{H}_0$ can be quantified, considering $\vec{B} \parallel \vec{z}$, as:

$$\Delta E_M = \mu_0 B M g, \tag{3.7}$$

where g is the Landé factor:

$$g(LS) = \frac{3}{2} + \frac{S(S+1) - L(L+1)}{2J(J+1)} \tag{3.8}$$

calculated for levels with $L - S$ coupling.
The single component transition at ν_0 is now splitted in different components

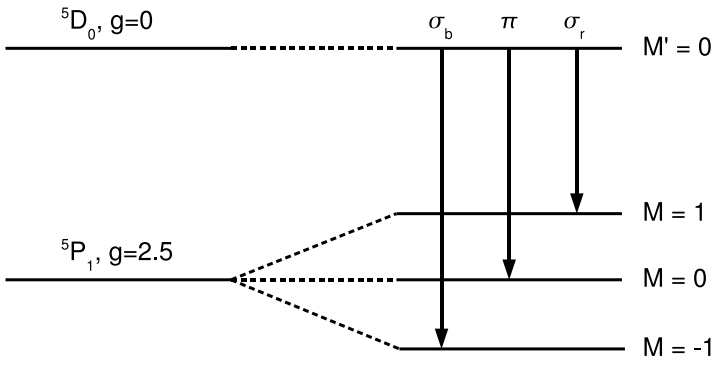

Figure 3.2: Illustrative representation of the level spitting, due to Zeeman effect, for the Fe I λ6302.5 transition. The possible transitions between the levels are represented as arrows; the Landé factors are also reported with the level representation.

whose frequencies are[2]:

$$\nu(M, M') = \nu_0 + \nu_L(gM - g'M'), \tag{3.9}$$

with g, M and g', M' characterizing the lower level and the upper level of the transition respectively, and $\nu_L = eB/4\pi mc$ the Larmor frequency. The selection rule $\Delta M = M' - M = 0, \pm 1$ allows to name the different components as: σ_b for $\Delta M = 1$, σ_r for $\Delta M = -1$, and π for $\Delta M = 0$ (see Figure 3.2).
To confer to each transition a polarization state we can refer to the simple case with $S = 0$, also defined the normal Zeeman effect. Due to the selection rule $\Delta S = 0$ one have $L = J$ and $L' = J'$ and $g = g' = 1$, for a total of three components: $\nu(M, M') = \nu_0 + \nu_L(M - M')$. By observing such an atom as shown in Figure 3.3, the longitudinal measure ($\theta = 0$ with respect to $\vec{B}$) consists of the two σ components circularly polarized. More in detail, the σ_b component is right-hand polarized and the component σ_r is left-hand polarized. The transversal measure ($\theta = \pi/2$ with respect to $\vec{B}$) shows the two linear projections of the σ components on the plane orthogonal to $\vec{B}$ plus

[2] $\Delta E_M = \mu_0 gBM = \frac{\hbar e}{2mc} gMB = \frac{he}{4\pi mc} gBM = \nu_L hgM$

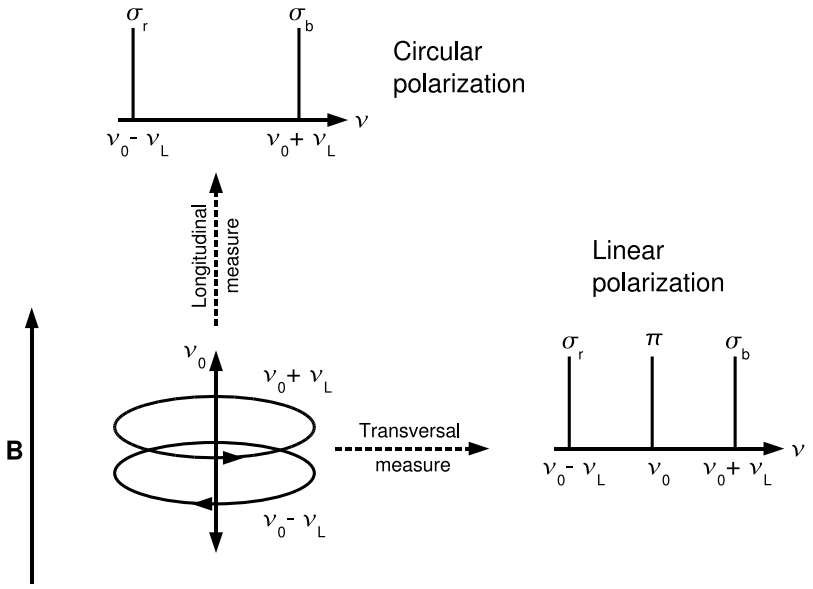

Figure 3.3: Illustrative representation of a polarization measurement in normal Zeeman effect.

the π component that is linearly polarized. For a generic θ the polarization can be thought as a mixture of these two cases[3].
In the case of $S \neq 0$ (anomalous Zeeman effect), the number of possible transitions increases, the polarization properties of the σ and π components remain the same, but a strength for each component is introduced so to weigh its own contribution. The weighs are defined as $S_q(M, M')$, with $q = M - M'$, so that, for a fixed q:

$$\sum_{M,M'} S_q(M, M') = 1. \tag{3.10}$$

In this way, also for the anomalous Zeeman effect, one can show that the center of gravity of the σ and π frequencies can be described similarly to Eq. 3.9 as:

$$X_q = \nu_0 - q\bar{g}\nu_L, \tag{3.11}$$

where:

$$\bar{g} = \frac{1}{2}(g + g') + \frac{1}{4}(g - g')[J(J+1) - J'(J'+1)] \tag{3.12}$$

is the effective Landé factor which describes the magnetic sensitivity, of a certain transition, to the magnetic field.

[3]For a complete description of polarization states associated to selection rules under dipole approximation refer to Bransden & Joachain (1983)

3.3 Radiative Transfer for Polarized Light

In this section we briefly describe how the equation of transport for Stokes parameters can be obtained adopting a classical approach.
Referring to § 3.1 we can state that the transport for polarized light can be described if the equation of transport of the tensor $\mathcal{E}_i^*\mathcal{E}_j$ is known. The propagation of the electric field in an anisotropic medium, permeated by a magnetic field, can be treated adopting an ad-hoc tern of complex vectors $(\vec{v}_\alpha)$, mutually orthogonal, along which the problem can be decomposed. In fact, expressing the electric field as $\vec{E}(\vec{r},t) = \sum_{\alpha=1}^{3} \mathcal{E}_\alpha(\vec{r},t)\vec{v}_\alpha$ one obtain for $\alpha = 1,2,3$:

$$\frac{d}{ds}\mathcal{E}_\alpha(\vec{r},t) = i\frac{\omega}{c}n_\alpha\mathcal{E}_\alpha(\vec{r},t), \tag{3.13}$$

where n_α is the complex refraction index for which $n_1 \neq n_2 \neq n_3$, $s = \vec{r}\cdot\vec{\Omega}$ and ω is the frequency of the wave.
As reported in § 3.1, the polarization tensor has been defined in the reference $\vec{e}_1, \vec{e}_2$ so that the relations between the components of the electric vector in this reference $(\mathcal{E}_k,\ k = 1,2)$ and those in the reference defined by the tern v_α are needed. By defining $C_{\alpha i} = \vec{v_\alpha}\cdot\vec{e}_i$, we can write:

$$\mathcal{E}_i = \sum_{\alpha=1}^{3} C_{\alpha i}\mathcal{E}_\alpha,\ \ \mathcal{E}_\beta = \sum_{k=1}^{2} C^*_{\beta k}\mathcal{E}_k, \tag{3.14}$$

and calculate the key expression for the polarization tensor [4]:

$$\frac{d}{ds}(\mathcal{E}_i^*\mathcal{E}_j) = -\sum_{k=1}^{2}(G^*_{ik}\mathcal{E}^*_k\mathcal{E}_j + G_{jk}\mathcal{E}^*_i\mathcal{E}_k) \tag{3.15}$$

where

$$G_{jk} = -i\frac{\omega}{c}\sum_{\alpha=1}^{3} n_\alpha C_{\alpha j}C^*_{\alpha k}. \tag{3.16}$$

[4]From Eqs. 3.13, 3.14 follows that: $\frac{d\mathcal{E}_j}{ds} = \sum_{\alpha=1}^{3} C_{\alpha j}\frac{d\mathcal{E}_\alpha}{ds} = i\frac{\omega}{c}\sum_{\alpha=1}^{3} n_\alpha C_{\alpha j}\mathcal{E}_\alpha = i\frac{\omega}{c}\sum_{\alpha=1}^{3}\sum_{k=1}^{2} n_\alpha C_{\alpha j}C^*_{\alpha k}\mathcal{E}_k$. Then, one have to take into account that for the polarization tensor: $\frac{d}{ds}(\mathcal{E}_i^*\mathcal{E}_j) = \frac{d\mathcal{E}_i^*}{ds}\mathcal{E}_j + \mathcal{E}_i^*\frac{d\mathcal{E}_j}{ds}$

From the definition of the Stokes parameters given referring to Eqs. 3.3 and from the inverse relations we can write [5]:

$$\frac{d}{ds}\begin{pmatrix} I \\ Q \\ U \\ V \end{pmatrix} = -\begin{pmatrix} \eta_I & \eta_Q & \eta_U & \eta_V \\ \eta_Q & \eta_I & \rho_V & -\rho_U \\ \eta_U & -\rho_V & \eta_I & \rho_Q \\ \eta_V & \rho_U & -\rho_Q & \eta_I \end{pmatrix}\begin{pmatrix} I \\ Q \\ U \\ V \end{pmatrix} \tag{3.17}$$

where $\eta_I = \mathrm{Re}(G_{11} + G_{22})$, $\eta_Q = \mathrm{Re}(G_{11} - G_{22})$, $\eta_U = \mathrm{Re}(G_{12} + G_{21})$, $\eta_V = \mathrm{Im}(G_{12} - G_{21})$, $\rho_Q = -\mathrm{Im}(G_{11} - G_{22})$, $\rho_U = -\mathrm{Im}(G_{12} + G_{21})$, $\rho_V = \mathrm{Re}(G_{12} - G_{21})$.
To define a complete radiative transfer equation for Stokes parameters we have to calculate the elements of the matrix in Eq. 3.17 by calculating the elements of the tensor G_{ij}. More exactly, we have to calculate n_α and the elements of the transformation matix $\mathcal{C}_{\alpha i} = \vec{v}_\alpha \cdot \vec{e}_i$ keeping in mind that, for the tern $\vec{v}_\alpha$, one have $n_1 \neq n_2 \neq n_3$.

As a first step, we calculate the refraction indexes n_α. This can be done, adopting a classical approach for the description of the electron motion (Lorentz atom) due to an electric field, by solving the following equation:

$$\frac{d^2\vec{x}}{dt^2} = -\omega_0^2\vec{x} + \frac{2e_0^2}{3mc^3}\frac{d^3\vec{x}}{dt^3} - \frac{e_0}{mc}\frac{d\vec{x}}{dt} \times \vec{B} - \frac{e_0}{m}\vec{E}_0 e^{-i(\omega t - \varphi)} \tag{3.18}$$

looking for a solution of the type $\vec{x} = \vec{A}e^{-i(\omega t-\varphi)}$ in a reference system defined by $\vec{u}_{-1} = \frac{1}{\sqrt{2}}(\vec{u}_x - i\vec{u}_y)$, $\vec{u}_1 = \frac{1}{\sqrt{2}}(\vec{u}_x + i\vec{u}_y)$, $\vec{u}_0 = \vec{u}_z$ with $\vec{B}$ along $\vec{u}_z$ (see Figure 3.4). In this way it can be shown that the equation can be written as[6]:

$$A_\alpha = \chi_\alpha(E_0)_\alpha,\ \chi_\alpha = -\frac{e_0/m}{\omega_0^2 - \omega^2 + 2\alpha\omega_L\omega - i\gamma\omega}. \tag{3.19}$$

In this expression $\omega_L = e_0B/2mc$ is the Larmor angular frequency and $\gamma = 2e_0^2\omega^2/3mc^3$.
Noting that, for each α, Eq. 3.18 can be treated as an isotropic case one can state that $n_\alpha^2 E_\alpha = E_\alpha + 4\pi P_\alpha$ where, generalizing the solution to N_A atoms per unit of volume the polarization ($\vec{P}$) induced by the electric field on a system of atoms is $\vec{P} = -e_0N_A\vec{A}e^{-i(\omega t-\varphi)}$ so that $P_\alpha = -e_0N_AA_\alpha e^{-i(\omega t-\varphi)} =$

[5] As an example we can calculate here for the Stokes I:
$\frac{dI}{ds} = k\left(\frac{d}{ds}\mathcal{E}_1^*\mathcal{E}_1 + \frac{d}{ds}\mathcal{E}_2^*\mathcal{E}_2\right) = -k\left[\sum_{k=1}^2(G_{1k}^*\mathcal{E}_k^*\mathcal{E}_1 + G_{1k}\mathcal{E}_1^*\mathcal{E}_k) + \sum_{k=1}^2(G_{2k}^*\mathcal{E}_k^*\mathcal{E}_2 + G_{2k}\mathcal{E}_2^*\mathcal{E}_k)\right] =$
$-k\left[G_{11}^*\mathcal{E}_1^*\mathcal{E}_1 + G_{11}\mathcal{E}_1^*\mathcal{E}_1 + G_{12}^*\mathcal{E}_2^*\mathcal{E}_1 + G_{12}\mathcal{E}_1^*\mathcal{E}_2 + G_{21}^*\mathcal{E}_1^*\mathcal{E}_2 + G_{21}\mathcal{E}_2^*\mathcal{E}_1 + G_{22}^*\mathcal{E}_2^*\mathcal{E}_2 + G_{22}\mathcal{E}_2^*\mathcal{E}_2\right] =$
$I\mathrm{Re}(G_{11} + G_{22}) + Q\mathrm{Re}(G_{11} - G_{22}) + U\mathrm{Re}(G_{12} + G_{21}) + V\mathrm{Im}(G_{12} - G_{21})$

[6] For the tern $\vec{u}_\alpha$ it can be shown that $\vec{u}_\alpha \times \vec{u}_0 = i\alpha\vec{u}_\alpha,\ \alpha = \pm 1, 0$

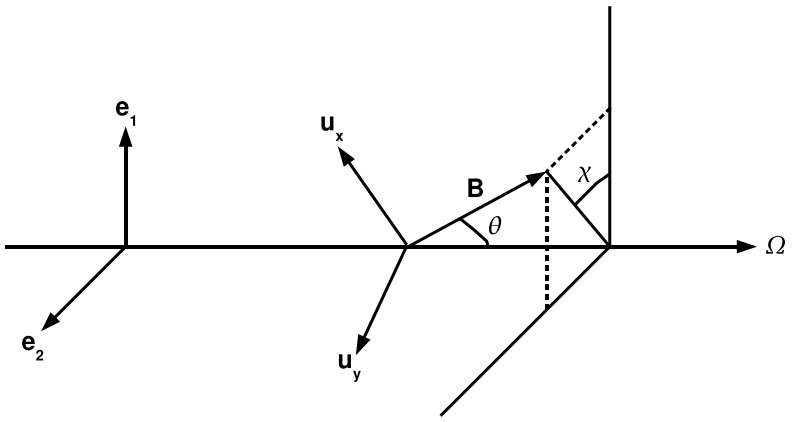

Figure 3.4: Geometry of the coordinate systems used to define the radiative transfer equation for polarized light.

$-e_0 N_A \chi_\alpha E_\alpha$, from which n_α can be derived.

At this point, to generalize the obtained results to a realistic stellar atmosphere permeated by a magnetic field $\vec{B}$, we have to take into account three different points:

- Atoms in a stellar atmosphere follows a Maxwellian distribution of velocities.
- The classical approach only is valid for the normal Zeeman effect, while, in the most general case, we expect to deal with anomalous Zeeman effect.
- The quantum mechanics solution suggests to substitute N_A with the oscillator density $N_b f_{ba}$, with N_b the number of atoms, per unit of volume, at the lower level, and f_{ba} the oscillator strength of the transition.

The final version of the tensor G_{ij} can be written as:

$$G_{ij} = \frac{1}{2}\frac{\pi e_0^2}{mc} N_b f_{ba} \sum_{\alpha=-1}^{1} (\phi_\alpha - i\psi_\alpha) C_{\alpha i} C^*_{\alpha j} \tag{3.20}$$

where:

$$\begin{aligned}
\phi_\alpha &= \frac{1}{\sqrt{\pi}}\frac{1}{\Delta\nu_D}\sum_{M-M'=\alpha} S_{-\alpha}(M,M')H(v-\alpha v_B(M,M'),a),\\
\psi_\alpha &= \frac{1}{\sqrt{\pi}}\frac{1}{\Delta\nu_D}\sum_{M-M'=\alpha} S_{-\alpha}(M,M')L(v-\alpha v_B(M,M'),a),\\
v_B(M,M') &= \frac{(g'M'-gM)\nu_L}{\Delta\nu_D},
\end{aligned} \tag{3.21}$$

In Eq. 3.21 H and L are the Voigt function and the Faraday-Voigt function, respectively, while $v=\frac{\nu-\nu_0}{\Delta\nu_D}$, $\Delta\nu_D=\nu_0\frac{\omega_T}{c}$, $a=\frac{\Gamma_n+\Gamma_c}{\Delta\nu_D}$, where $\Gamma_n=\frac{\gamma}{4\pi}=\frac{2\pi e_0^2\nu_0^2}{3mc^3}$ and $\Gamma_c=\frac{f}{2\pi}$ with f the collision frequency.

From Eq. 3.19 is straightforward to show that for the adopted tern, $\vec{v}_\alpha$, $n_{-1}\neq n_{+1}\neq n_0$. From this, it follows that $\mathcal{C}_{\alpha i}=\vec{u}_\alpha\cdot\vec{e}_i$ is a correct definition for the transformation matrix to obtain Eq. 3.13. The relations between $\vec{e_i}$ and $\vec{u_\alpha}$ directly follow from (see Figure 3.4):

$$\begin{aligned}
\vec{u}_x &= \cos\theta\cos\chi\vec{e}_1+\cos\theta\sin\chi\vec{e}_2-\sin\theta\vec{\Omega},\\
\vec{u}_y &= -\sin\chi\vec{e}_1+\cos\theta\vec{e}_2,\\
\vec{u}_z &= \sin\theta\cos\chi\vec{e}_1+\sin\theta\sin\chi\vec{e}_2+\cos\theta\vec{\Omega},
\end{aligned} \tag{3.22}$$

as

$$\begin{aligned}
\vec{u}_{\pm1} &= \frac{1}{\sqrt{2}}\left[(\cos\theta\cos\chi\mp i\sin\chi)\vec{e}_1+(\cos\theta\sin\chi\pm i\cos\chi)\vec{e}_2-\sin\theta\vec{\Omega}\right],\\
\vec{u}_0 &= \vec{u}_z.
\end{aligned} \tag{3.23}$$

3.4 Solutions for the Radiative Transfer Equation

In § 3.3 we exposed how the radiative transfer for polarized light can be exhaustively defined by knowing the G_{ij} tensor defined in Eq. 3.16. In our work we are interested in the solution of the radiative transfer equation under Local Thermodynamic Equilibrium (LTE). Under this hypothesis Eq. 3.17 can be rewritten as follows:

$$\frac{d}{ds}\begin{pmatrix}I\\Q\\U\\V\end{pmatrix} = -\begin{pmatrix}k_c+\eta_I & \eta_Q & \eta_U & \eta_V\\ \eta_Q & k_c+\eta_I & \rho_V & -\rho_U\\ \eta_U & -\rho_V & k_c+\eta_I & \rho_Q\\ \eta_V & \rho_U & -\rho_U & k_c+\eta_I\end{pmatrix}\begin{pmatrix}I-B_\nu\\Q\\U\\V\end{pmatrix}, \tag{3.24}$$

where we introduced the emission coefficients $\eta_I B_\nu$, $\eta_Q B_\nu$, $\eta_U B_\nu$, $\eta_V B_\nu$, and k_c is the continuum absorption coefficient.
At this point we want to describe two analytical solutions to the radiative transfer problem defined in Eq. 3.24 following from two different hypothesis; however the reader have to keep in mind that the general problem can be only solved adopting numerical techniques.
The first hypothesis is the Weak Field Approximation (WFA) for which the Doppler width of the line, $\Delta\lambda_D = \lambda^2 \frac{\omega_T}{c}$ due to the thermal motion of atoms, is considered larger than the wavelength separation induced by the magnetic field via Zeeman effect, $\Delta\lambda_B = \lambda \frac{\nu_L}{\nu} = \lambda^2 \frac{\nu_L}{c}$. Under this condition it can be shown that the light is not linearly polarized and that:

$$V = -\bar{g}\Delta\lambda_B \cos\theta \frac{dI}{d\lambda}, \tag{3.25}$$

so that, Stokes V amplitude varies linearly with the projection of the magnetic field along the line of sight. This result shows in practice the effect of the simple sketch given in Figure 3.3. Another aspect that is worth to note is the linear dependence of Stokes V from the effective Landé factor; this clearly sets the sensitivity of the circular polarization of the line to the presence of the magnetic field. The derivative of Stokes I with respect to λ is supposed to e constant while varying the magnetic field, this comes directly from the WFA.

The other analytical solution follows from the Milne-Eddington approximation (ME). Under this hypothesis the coefficients of the matrix in Eq. 3.24 are considered constant with the optical depth $d\tau_c = k_c\, ds$ while the Plank function B_ν is supposed to vary linearly with this quantity, i.e. $B_\nu = B_0 + B_1\tau_c$. By defining $h_I = \eta_I/k_c$, $h_Q = \eta_Q/k_c$, $h_U = \eta_U/k_c$, $h_V = \eta_V/k_c$, $f_Q = \rho_Q/k_c$, $f_U = \rho_U/k_c$ and $f_V = \rho_V/k_c$ and $\Delta = (1+h_I)^4 + (1+h_I)^2(f_Q^2 + f_U^2 + f_V^2 - h_Q^2 - h_U^2 - h_V^2) - (h_Q f_Q + h_U f_U + h_V f_V)^2$ one obtain:

$$\begin{aligned}
I =& B_0 + B_1\Delta^{-1}(1+h_I)[(1+h_I)^2 + f_Q^2 + f_U^2 + f_V^2] \\
Q =& -B_1\Delta^{-1}[(1+h_I)^2 h_Q + (1+h_I)(h_V f_U - h_U f_V) + \\
&+ f_Q(h_Q f_Q + h_U f_U + h_V f_V)] \\
U =& -B_1\Delta^{-1}[(1+h_I)^2 h_U + (1+h_I)(h_Q f_V - h_V f_Q) + \\
&+ f_U(h_Q f_Q + h_U f_U + h_V f_V)] \\
V =& -B_1\Delta^{-1}[(1+h_I)^2 h_V + (1+h_I)(h_U f_Q - h_Q f_U) + \\
&+ f_V(h_Q f_Q + h_U f_U + h_V f_V)].
\end{aligned} \tag{3.26}$$

This solution depends on nine independent parameters: B_0 and B_1 accounting for the thermal properties of the atmosphere, B, θ and χ, describing the

properties of the magnetic field vector and $R = \pi e^2 N_A / mck_c$, $\Delta\lambda_D$ and a defining the properties of the spectral line[7].

3.5 Hyperfine Structure of Spectral Lines

The formalism to deal with hyperfine structure (HFS) lines in magnetized atmospheres was developed more than thirty years ago by Landi degl'Innocenti (1975). In his work the author considered spectral lines originating from the transition between two levels of an isotope with nuclear spin $\vec{I}$. The problem can be formulated by taking into account a perturbation Hamiltonian $\mathcal{H}_p$ defined as $\mathcal{H}_p = \mathcal{H}_0 + \mathcal{H}^{(1)}_{HFS} + \mathcal{H}^{(2)}_{HFS}$, where the first term has been already defined in Eq. 3.6 and the last two terms account for the magnetic-dipole and electric-quadrupole interactions.
By defining the total angular momentum $\vec{F} = \vec{J} + \vec{I}$, with projection along the magnetic field (z axis) f, it can be shown that for the HFS part of the perturbation Hamiltonian $\mathcal{H}_p$ the eigenvalues are:

$$\begin{aligned} \Delta E^{(1)}_{HFS} &= \frac{1}{2} K \mathcal{A}, \\ \Delta E^{(2)}_{HFS} &= \mathcal{B}[K(K+1) - \frac{4}{3} I(I+1)J(J+1)], \end{aligned} \tag{3.27}$$

where $\mathcal{A}$ and $\mathcal{B}$ are the HFS constants which account for the the magnetic-dipole coupling, $\mathcal{A}$, and the electric-quadrupole coupling $\mathcal{B}$. These constants can be determined experimentally or theoretically.
Landi degl'Innocenti (1975) showed that the elements of the array in the radiative transport equation in the case of HFS lines are identical to the elements defined in § 3.3. This fact is connected to the selection rules for the quantum number M (see § 3.2) that can be transported to the quantum number f. Consequently, it follows the distinction between linearly polarized components (π with $\Delta f = 0$ and $q = 0$), right-hand circularly polarized components (σ_b with $\Delta f = 1$ and $q = -1$) and left-hand circularly polarized components (σ_r with $\Delta f = -1$ and $q = 1$).

[7]For a detailed treatment about § 3.3 and § 3.4 refer to Landi degl'Innocenti (2007)

Chapter 4

Synthesis and Inversion of Photospheric Lines

§ 1.2.1 illustrates in an extensive manner how much spectropolarimetry techniques are central in the investigation of quiet Sun magnetic fields. Refined measurements based on the Hanle depolarization and Zeeman effect in the visible or infrared spectral lines, combined with improved diagnostic techniques, are beginning to offer researchers a picture of internetwork magnetism whose details are becoming clearer and clearer. For this reason, this chapter, regarding recent improvements in spectropolarimetry techniques for visible spectral lines, defines the main part of this thesis.
In detail, the arguments we are going to deal with can be organized in three main parts. The first one, from § 4.1 to § 4.5, concerning recent applications, as diagnostic tools for quiet Sun magnetic field measurements, of spectropolarimetric features emerging in Stokes profiles from the superposition of Zeeman effect and HFS of manganese atoms. The second one, from § 4.6 to § 4.9, about preliminary results retrieved by an inversion analysis of polarization signals, measured in Fe I λ6301 and Fe I λ6302 spectral lines, by the HINODE SOT/SP instrument. The third one, from § 4.10 to § 4.15, about the sensitivity of the Mn I λ5395 line to the solar activity.

The properties of spectral lines presenting HFS and sensible to magnetic field via Zeeman effect have been recently pointed out by López Ariste et al. (2002) with the aim of improving the spectropolarimetric techniques for the diagnostic of quiet Sun magnetic fields. In § 4.1 – § 4.5 we'll report the work done to analyze in detail the properties of different Mn I lines through the upgrade of a synthesis code able to solve the radiative transfer problem for polarized light under LTE hypothesis (Eq. 3.24) in different model atmospheres, characterized by different degree of realism in the representation of

solar photosphere. More in detail, we'll describe three synthesis procedures: ME, one-dimensional (1D) and MIcro Structured Magnetized Atmosphere (MISMA, Sánchez Almeida et al. 1996; Sánchez Almeida 1997).

4.1 The Synthesis Procedures

The synthesis of Stokes profiles has been carried out using three different approaches to solve the radiative transfer equation for polarized light (Eq. 3.24) that can be expressed in a more compact way as:

$$\frac{d\vec{I}}{ds} = -\mathbf{K}(\vec{I} - \vec{S}), \tag{4.1}$$

where $\vec{I} = (I, Q, U, V)^t$ is the column vector containing the Stokes parameters, $\vec{S} = (B_\nu, 0, 0, 0)^t$ is the source vector with B_ν the LTE source function, $\mathbf{K}$ is the 4×4 absorption matrix and, finally, the variable of integration s corresponds to the length along the line of sight. The three codes differ in the model atmosphere used to describe the photosphere.

The first one solves Eq. 4.1 under ME hypothesis described in § 3.4. As known, the radiative transfer equation admits an analytic solution in terms of the two coefficients of the source function ($B_\nu = B_0 + B_1\tau_c$) and the seven coefficients of the absorption matrix.

The second code solves Eq. 4.1 for 1D atmospheres. Realistic temperatures, pressures and magnetic field vectors are considered, but they only vary along the line of sight so that a single ray suffices to synthesize the spectrum.

The third code solves a different version of Eq. 4.1. It is obtained by a spatial averaging under the MISMA hypothesis (Sánchez Almeida et al. 1996). It assumes the solar atmosphere to have inhomogeneities smaller than the photon mean-free-path whose details are washed out by the radiative transfer process. Only their average properties matter. The new equation to be solved under the MISMA hypothesis is:

$$\frac{d\vec{I}}{ds} = -\langle \mathbf{K} \rangle (\vec{I} - \vec{S}') \tag{4.2}$$

where $\vec{S}' = \langle \mathbf{K} \rangle^{-1} \left\langle \mathbf{K}\vec{S} \right\rangle$ is a mean source vector. The brackets in Eq. 4.2 denote average over a volume whose dimension along the line of sight is of the order of the photon mean-free-path. As a result of the average, $\langle \mathbf{K} \rangle$ and $\vec{S}'$ are slowly varying functions of the variable s, with this variation accounting for the large scale structures in the atmosphere. Pursuing the idea that optically-thin details are irrelevant for the final spectrum, Sánchez Almeida

(1997) puts forward different MISMA models made of distinct components each one characterized by smooth variations with height of temperature, pressure and magnetic field vector. The coexistence of different components imposes a number of physical constraints to be satisfied, in particular, the lateral pressure balance causes the magnetic field to be coupled with the thermodynamic variables. The MISMA models, with their constraints, provide the degree of realism required to carry out our exploratory work. Note that they reproduce all kinds of Stokes profiles observed in the quiet Sun, including those with extreme asymmetries (Sánchez Almeida & Lites 2000; Socas-Navarro & Sánchez Almeida 2002; Domínguez Cerdeña et al. 2006). Eq. 4.1 is formally identical to Eq. 4.2 and they are both integrated using a predictor-corrector method with the variables equi-spaced in a fixed grid of atmospheric heights.

All the codes are based on the FORTRAN procedure HYPER by Landi degl'Innocenti (1978) that computes the Zeeman pattern of any line with HFS. The pattern depends on the externally imposed magnetic field, together with a set of atomic parameters, namely, the hyperfine structure constants, the quantum numbers of the two levels involved in the transition, the relative isotopic abundance, and the isotope shifts. When the Zeeman splitting is comparable to the HFS splitting, the Stokes profiles are strongly disrupted showing typical HFS features. The splitting depends on the so-called HFS constants $\mathcal{A}$ and $\mathcal{B}$ (see Eq. 3.27), which account for the two first terms of the Hamiltonian describing the interaction between the electrons in an atomic level and the nuclear magnetic moment.

The values of $\mathcal{A}$ adopted for our Mn I syntheses are listed in Table 4.1[8]. The footnotes include the appropriate references, which indicate that $\mathcal{B}$ is negligible small in all cases, for this reason the value for $\mathcal{B}$ is set to zero. The other symbols used in the table stand for: lower-level weighted oscillator strength gf, lower-level Landé factor $g_{\rm low}$, upper-level Landé factor $g_{\rm up}$, and lower-level excitation potential χ.

[8] [a]NIST Atomic Spectra Database, `http://physics.nist.gov/PhysRefData/ASD/`,
[b]Lefèbvre et al. (2003),
[c]Blackwell-Whitehead et al. (2005),
[d]Fisher & Peck (1939),
[e]Margrave (1972),
[f]set to match the observed Solar Spectrum with $\log[Mn] = 5.31$,
[g]Asensio Ramos et al. (2007).

Table 4.1: Atomic parameters used in the synthesis of Mn I lines [8]

Line	Wavelength[a] [Å]	Transition	χ^a [eV]	$\log gf$	$g^a_{\rm low}$	$g^a_{\rm up}$	$\mathcal{A}_{\rm low}$ $[10^{-3}{\rm cm}^{-1}]$	$\mathcal{A}_{\rm up}$ $[10^{-3}{\rm cm}^{-1}]$
Mn I λ4457	4457.04	$z^6P^0_{5/2} - e^6D_{3/2}$	3.073	-0.555^a	1.875	1.759	15.6^b	22.8^b
Mn I λ4470	4470.14	$a^4D_{3/2} - z^4D^0_{3/2}$	2.940	-0.444^a	1.198	1.200	1.7^c	6.4^c
Mn I λ4502	4502.22	$a^4D_{5/2} - z^4D^0_{7/2}$	2.919	-0.344^a	1.368	1.427	-4.6^c	1.5^c
Mn I λ4739	4739.11	$a^4D_{3/2} - z^4F^0_{3/2}$	2.940	-0.490^a	1.198	0.400	1.7^c	22.3^c
Mn I λ5420	5420.36	$a^6D_{7/2} - y^6P^0_{5/2}$	2.142	-1.460^a	1.584	1.886	13.5^d	-21.5^d
Mn I λ5516	5516.77	$a^6D_{3/2} - y^6P^0_{3/2}$	2.178	-1.847^a	1.866	2.400	16.5^d	-31.5^d
Mn I λ5538	5537.76	$a^6D_{1/2} - y^6P^0_{3/2}$	2.186	-1.920^e	3.327	2.400	27.8^d	-31.5^d
Mn I λ8741	8740.93	$y^6P^0_{7/2} - e^6D_{9/2}$	4.434	-0.05^f	1.712	1.554	-13^b	15.5^b
Mn I λ15262	15262.70	$e^8S_{7/2} - y^8P^0_{5/2}$	4.889	$+0.45^f$	2.000	2.284	25.2^b	27.5^b

4.1.1 Testing the synthesis procedures

Different types of tests have been carried out by using the line Mn I λ5538 as main target. Intensity profiles have been compared with the unpolarized solar atlas and (ME) Stokes profiles existing in the literature. Moreover, the codes have been cross-checked one with respect to another, and with existing synthesis codes that neglect the HFS. The entire work is summarized next.
The first series of tests is based on non-magnetic atmospheres (i.e., without considering spectropolarimetry). We start by recovering the ME Stokes I profile in López Ariste et al. (2002, Figure 3) when using the appropriate ME parameters (López Ariste 2007, private communication). In addition, Figure 4.1 shows a reasonable ME fit to the FTS solar spectrum using a Doppler width $\Delta\lambda_D = 0.029$ mÅ, a damping constant $a = 0.3$, an absorption coefficient $\eta_0 = 2.7$, a source function given by $B_0 = 1.0$ and $B_1 = 1.1$, and the atomic parameters in Table 4.1. Figure 4.1 also includes a fit to the observed profile using the 1D code. The line is synthesized in the quiet Sun model atmosphere by Maltby et al. (1986) using the atomic parameters in Table 4.1. The fit was carried out by trial-and-error varying the velocity along the line of sight, the macroturbulence (v_{mac}, set to 1.3 km s^{-1}), and the Mn abundance (log[Mn], set to 5.30 in the scale where log[H]=12). The MISMA code was also tested against the observed Stokes I assuming the thermodynamic parameters of the model atmosphere to be given by the model quiet Sun in Sánchez Almeida (1997). As in the case of 1D atmospheres, the atomic parameters are those listed in Table 4.1, and we vary the velocity along the LOS, the macroturbulence (v_{mac} =1.5 km s^{-1}), and the Mn abundance (log[Mn]=5.31). One additional consistency test was carried out with the 1D code. We compare the synthesis obtained neglecting the hyperfine structure (i.e., imposing $\mathcal{A} = \mathcal{B} = 0$) with the intensity of the 1D

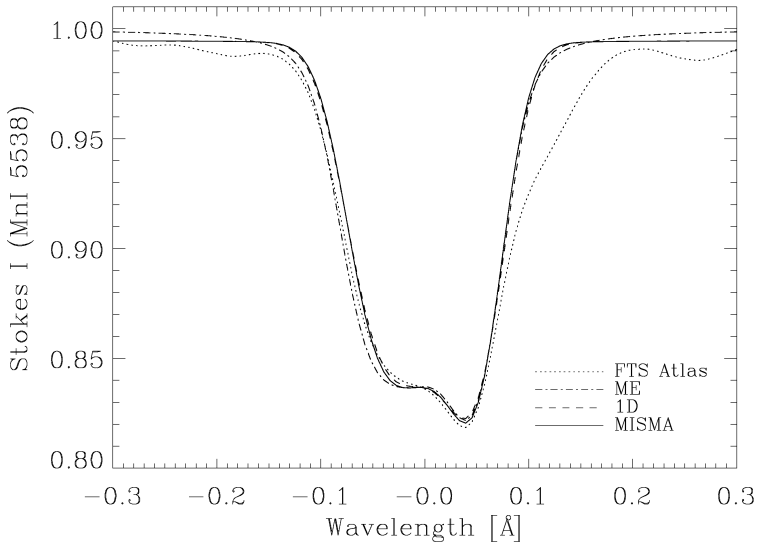

Figure 4.1: Mn I λ5538 Stokes I profiles synthesized using the three codes and compared with the profile from the solar FTS atlas. The inset identifies the different codes and the observation. The wavelengths, in units of Å, are referred to the laboratory wavelength of the line. The profiles are normalized to the quiet Sun continuum intensity.

code from which we inherited the absorption coefficient routines (Sanchez Almeida 1992). The profiles of the two syntheses are identical within the numerical precision.

The second series of tests refers to magnetic atmospheres. Employing the atomic parameters and the atmospheres described above, we include a constant magnetic field vector. We use three different magnetic field strengths, $B = 100$ G, 300 G, and 900 G, with the same inclination, $\theta = 60°$, and azimuth, $\phi = 0°$. The ME syntheses reproduce the Stokes profiles in Figure 4 of López Ariste et al. (2002). Stokes V profiles synthesized with the three codes are shown in Figure 4.2. The agreement between the syntheses supports their internal consistency, i.e., if the codes are tuned to produce similar Stokes I profiles (Figure 4.1), then for the same field strength they also produce similar Stokes V. The Stokes V profiles represented in Figure 4.2 correspond to (and are consistent with) the two behaviours of Mn I λ5538 described by López Ariste et al. (2002). The left panel in Figure 4.2 shows the kind of profile for $B \lesssim 700$ G, with a characteristic reversal not far from the line core due to the HFS in the absorption pattern (hereafter HFS hump). The

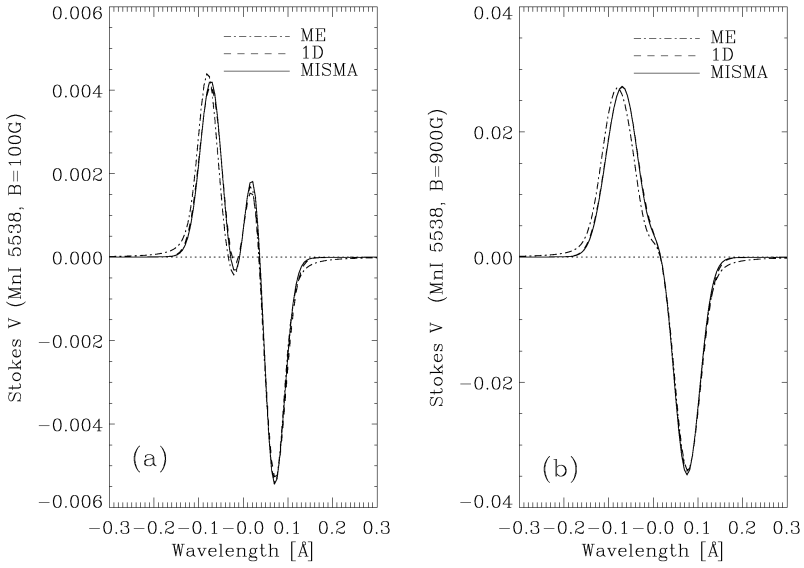

Figure 4.2: Mn I λ5538 Stokes V profiles synthesized using the three codes with $B = 100$ G (a) and $B = 900$ G (b). The insets pair each type of line with the corresponding synthesis code. The profiles are normalized to the quiet Sun continuum intensity, and the wavelengths are refereed to the laboratory wavelength of the line.

right panel corresponds to $B \gtrsim 700$ G, which do not generate HFS humps at the core. The presence or absence of such reversal is used by López Ariste and co-workers to distinguish between sub-kG fields (present) and kG fields (absent).

The results in § 4.5 can be regarded as a third independent test. The same non-magnetic quiet Sun model MISMA that reproduces the observed intensity of Mn I λ5538 also account for eight additional Mn I lines with very different HFS patterns. Such agreement shows the realism and self-consistency of the syntheses.

4.2 1D Syntheses

The weak magnetic field approximation introduced in § 3.4 is routinely used in solar magnetometry to, e.g., calibrate magnetograms. For the remarks reported in § 3.5 we can state that it is also valid for lines with HFS because the radiative transport equation in the case of HFS lines is identical to the case without HFS (Landi degl'Innocenti 1975). For this reason it was used

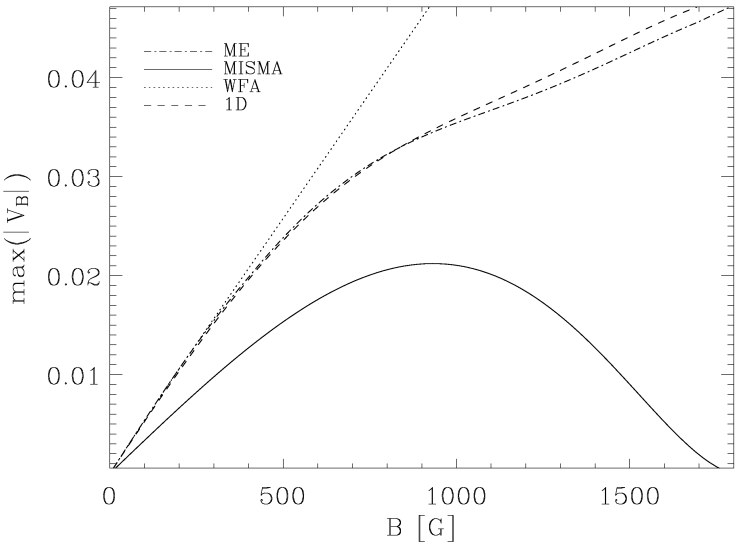

Figure 4.3: Maximum Stokes V amplitude as a function of the magnetic field strength for ME, 1D, and MISMA model atmospheres. The prediction corresponding to the weak field approximation is represented as the dotted line. All magnetic field inclinations are set to 60°. Magnetic field strengths are given in G.

by López Ariste et al. (2006) to estimate the relative contribution of weak and strong fields to the observed quiet Sun signals of Mn I λ5538. When the approximation holds the Stokes V profile is proportional to the longitudinal component of the magnetic field $B\cos\theta$ (Eq. 3.25),

$$V = -c\frac{dI}{d\lambda}B\cos\theta, \tag{4.3}$$

where the constant c depends on the particular spectral line, and the derivative of the intensity profile, $dI/d\lambda$, gives the variation with wavelength of Stokes V.

We tested the approximation with the quiet Sun model atmospheres described in § 4.1.1, which are realistic in the sense that they reproduce the observed intensity profile when the magnetic field strength is close to zero (Figure 4.1). The syntheses assume the magnetic field to be constant along the LOS, with the inclination θ set to 60°. Figure 4.3 shows the variation of the maximum Stokes V signal as a function of the magnetic field strength. The weak field approximation breaks down for fairly low magnetic field strengths, i.e., $B \gtrsim 400$ G (compare the dashed line and the dotted line

in Figure 4.3). Even more, the deviations are very important for kG magnetic field strengths. When the field strength is 1.5 kG the weak field approximation yields a Stokes V signal twice larger than the synthetic signals in 1D model atmospheres (Figure 4.3). In order to test the dependence on $\cos\theta$ predicted by Eq. 4.3, we also carried out syntheses with various magnetic field inclinations. This dependence turns out to be closely followed by the synthetic signals, even for strong kG magnetic field strengths. The behaviour was to be expected since Mn I λ5538 is a weak line satisfying the weakly polarizing medium approximation (Sánchez Almeida & Trujillo Bueno 1999). In this approximation Stokes V scales with its specific absorption coefficient, which is proportional to $\cos\theta$ independently of whether or no the spectral line has HFS.

The quiet Sun contains plasmas with all magnetic field strengths from 0 to 2 kG (§ 1.2). According to a mechanism originally put forward by Spruit (1976) and now well established, one expects a strong correlation between the magnetic field strength and the temperature of the observable photospheric layers. Plasmas having kG fields must be strongly evacuated to stay in mechanical balance within the photosphere. Consequently, strongly magnetized plasmas are transparent, showing light coming from deep and therefore hot (sub-)photospheric layers. In order to explore the dependence of the Mn I λ5538 Stokes V signals on the thermodynamics, we compare synthetic profiles formed under different thermodynamic conditions but the same magnetic field strength. The line is synthesized in a quiet Sun model atmosphere (Maltby et al. 1986), a network model atmosphere (Solanki 1986; Solanki & Steenbock 1988), and a plage model atmosphere (Solanki 1986; Solanki & Steenbock 1988), with the temperature increasing from quiet Sun to network. The results are shown in Figure 4.4.

First, note that the continuum intensity of Stokes I increases from quiet Sun (the coolest model) to network (the hottest model). In anticorrelation with continuum intensity, the Stokes V signals decrease with increasing temperature (Figure 4.4, right panel). This behaviour is not attributable to the HFS, but it is due to the ionization balance of manganese in the photosphere. Mn I is the minor species so that a small modification of the ionization equilibrium does not alter the Mn II abundance but it drastically changes the number of Mn I atoms available for absorption. Increasing the temperature increases the ionization, and the Mn I lines weaken. Figure 4.5 shows the relative abundance of Mn I as a function of height in the atmosphere for a constant density representative of the layers where the lines are formed (say, 100 km above continuum optical depth equals one). According to Figure 4.5, if the presence of a strong magnetic field decreases the formation height of a spectral line by 100 km, then the Mn I is depleted by more than one order

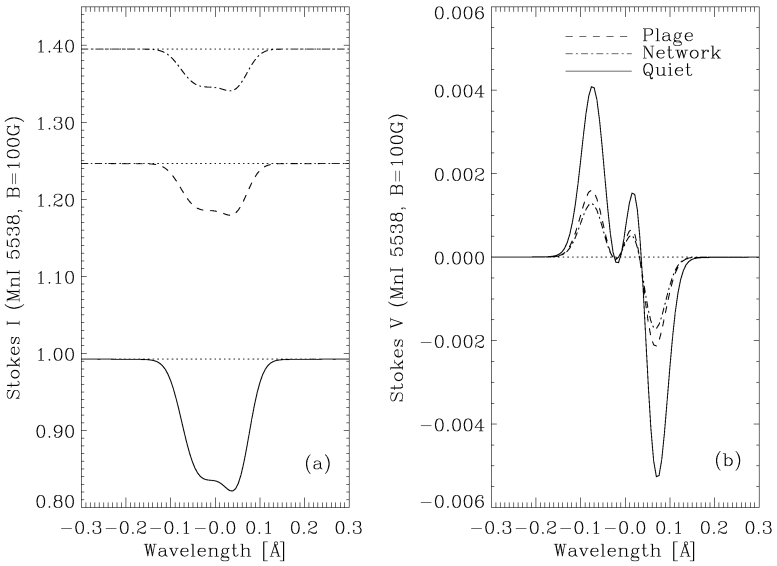

Figure 4.4: Stokes I and V profiles synthesized in three 1D model atmospheres corresponding to the quiet Sun (the solid line), network (the dotted dashed line), and plage (the dashed line). The magnetic field is constant with a strength of 100 G and an inclination of 60°. All profiles have been normalized to the quiet Sun continuum intensity. The dotted line is just a reference to show the continuum level.

of magnitude (compare the values at 100 km and 0 km). Note that this behaviour is common to all Mn I lines, and it is also typical of other minor species like Fe I (e.g., the dotted line in Figure 4.5). In short, the Mn I lines are expected to weaken with increasing magnetic field strength.
The coupling between magnetic field strength and temperature is fully accounted for in the MISMA syntheses, which partly explains the dimming of the kG Stokes V signals shown in Figure 4.3 (the solid line).

4.3 Multicomponent Syntheses

The syntheses carried out so far assume very simple magnetic configurations. The magnetic field is either constant or, in the case of MISMA models, one magnetic component varies along the LOS. Due to the complex topology of the quiet Sun magnetic fields, our limited angular resolution, and the spatial averages carried out to obtain appropriate signals, those simplifications are insufficient to represent observed Stokes profiles. Real polarization sig-

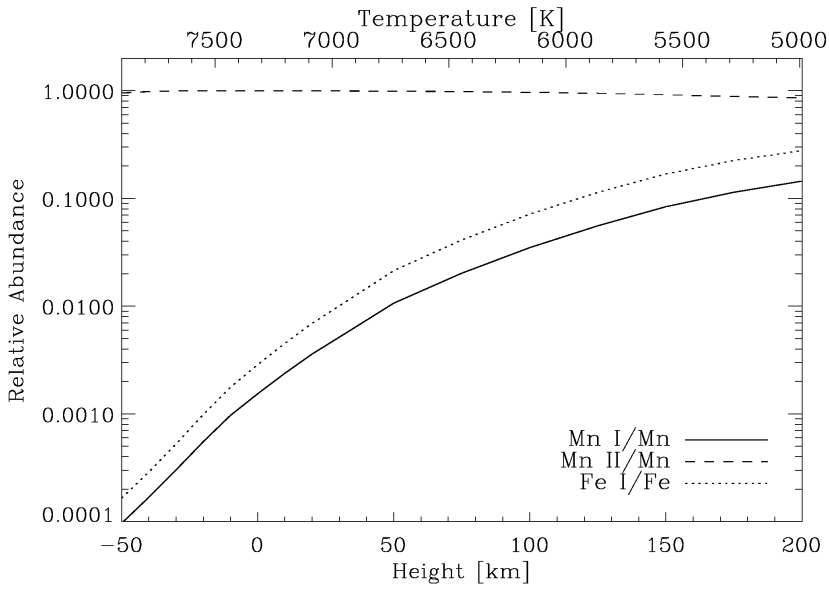

Figure 4.5: Relative abundance of Mn I and Mn II as a function of the height in the atmosphere for a quiet Sun stratification of temperatures (the temperature corresponding to each height appears on the top of the figure). The gas pressure is the same for all the heights, and it has been chosen to match the gas pressure of the non-magnetic quiet Sun some 100 km above the continuum optical depth equals one. The Fe I abundance is included for comparison; its overabundance with respect to Mn I is due to its higher ionization potential.

nals are formed in plasmas having a range of magnetic properties, therefore, we improve the realism of the synthesis assuming multi-component model atmospheres. Specifically, we assume:

$$I = \int_0^{B_{\max}} P(B)\, I_B\, dB, \tag{4.4}$$

and

$$V = \int_0^{B_{\max}} \langle \cos\theta \rangle\, P(B)\, V_B\, dB, \tag{4.5}$$

where $\langle \cos\theta \rangle$ is defined as

$$\langle \cos\theta \rangle = \frac{1}{P(B)} \int_0^{2\pi} \int_0^{\pi} \cos\theta\ \mathcal{P}(B,\theta,\phi)\, d\theta d\phi. \tag{4.6}$$

to absorb the general dependence of the most general probability density function $\mathcal{P}(B,\theta,\phi)$ on the direction of $\vec{B}$ described by the inclination θ and

the azimuth ϕ.
The symbols I_B and V_B in Eqs. 4.4 and 4.5 represent the Stokes I and V profiles produced by an atmosphere with a single longitudinal magnetic field of strength B, whereas $P(B)$ stands for the fraction of resolution element occupied by such atmosphere. The $P(B)$ is the PDF already introduced in § 1.2. The function is normalized to one, and it can be envisaged as the filling factor corresponding to each B. The maximum field strength existing in the quiet Sun sets $B_{\max}$ to some 2 kG (e.g., Spruit 1979). We have to clarify, however, that the PDF approach for representing the complications of the quiet Sun magnetic fields also has limitations. Eqs. 4.4 and 4.5 imply a one-to-one relationship between the magnetic field and the thermodynamic structure of the atmosphere. Although a coupling between magnetic field and thermodynamics is to be expected, the real relationship should have a significant scatter (e.g., Vögler et al. 2003). Magnetic field variations along the LOS are restricted, and the overlapping along the LOS of structures with different magnetic fields is ignored. Our PDF approach is only a first approximation to the problem.
The four PDFs in Figure 1.4 are used for synthesis. They correspond to one of the semi-empirical quiet Sun PDFs obtained by Domínguez Cerdeña et al. (2006) (labelled DC), plus the PDFs of the three magneto-convection numerical simulations by Vögler et al. (2003), representing magnetic fluxes of 10 G, 50 G and 200 G (V10, V50 and V200, respectively). When ME atmospheres, 1D atmospheres, and MISMA models are combined according to these PDFs, one obtains the Stokes V profiles shown in Figure 4.6. In this case the magnetic field inclination is constant and set to 60°, i.e., $\langle \cos\theta \rangle = 1/2$. The corresponding Stokes I profiles for the ME and the 1D cases are practically identical to those in Figure 4.1. The MISMA synthesis has a continuum intensity 5% lower than that of the quiet Sun, since the thermodynamic structure of the model MISMA used for synthesis is cooler than the typical quiet Sun model atmospheres (see Figure 11 in Sánchez Almeida & Lites 2000).
Note that the Stokes V profiles in Figure 4.6 always show HFS humps. This result warns us against simplistic interpretations of the presence of HFS features as the unequivocal signature of an atmosphere dominated by hG magnetic fields. Despite the fact that most of the atmospheric volume has very low field strengths, the magnetic flux and the magnetic energy of some of the PDFs used for synthesis are dominated by the tail of kG fields. The extreme case corresponds to V200 in Figure 1.4, where 60% of the magnetic flux and 87% of the energy, computed as the two first moments of the PDF, is in field strengths larger than 700 G, which is the field strength where the HFS hump disappears according to the ME syntheses. Even in this case the

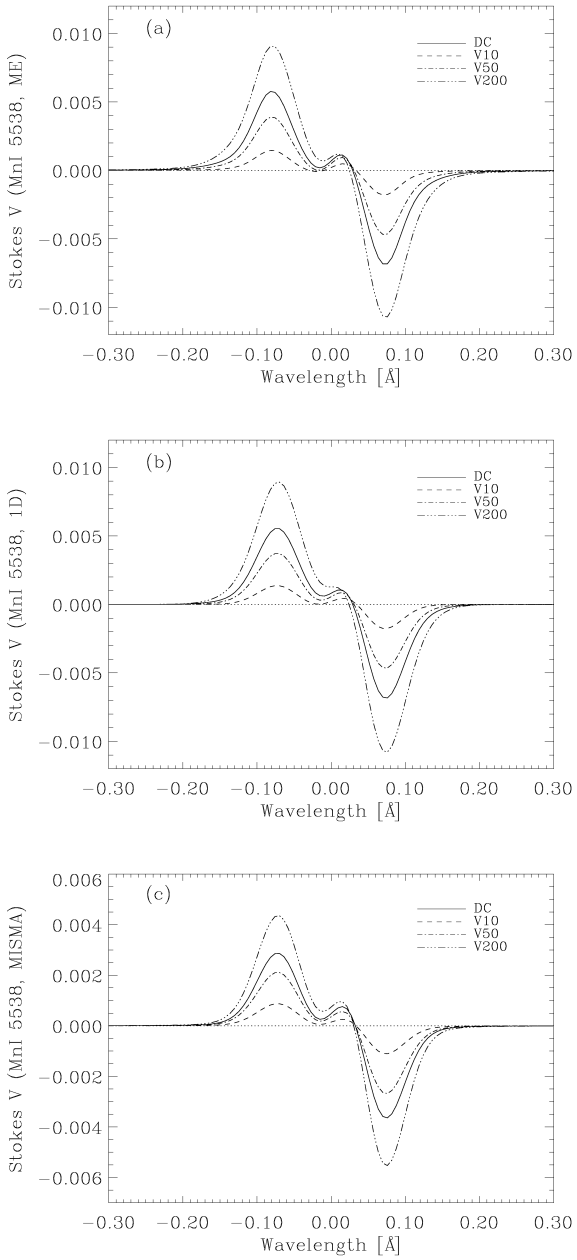

Figure 4.6: Multi-component Stokes V profiles synthesized using ME atmospheres (a), 1D atmospheres (b), and MISMAs (c). The labels and the lines in the insets refer to the PDFs in Figure 1.4. The profiles are normalized to the quiet Sun continuum intensity.

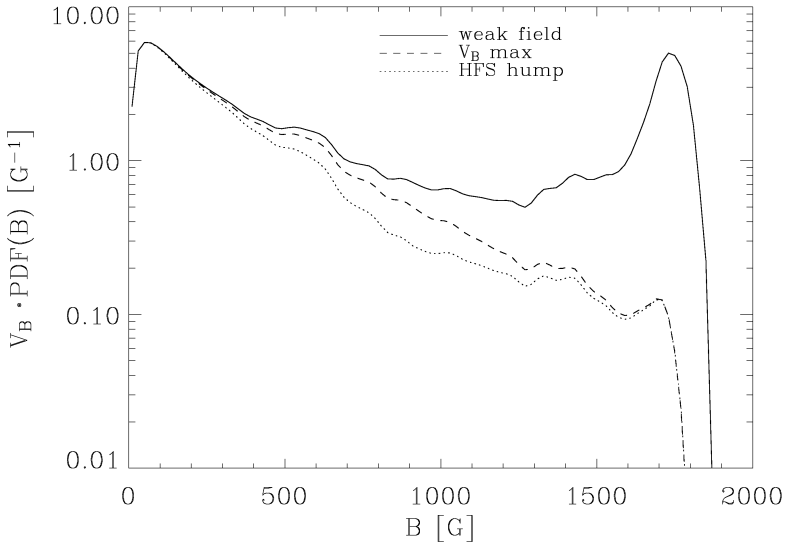

Figure 4.7: Relative contribution to the average Stokes V profile of a multi-component atmosphere characterized by the PDF labelled as DC in Figure 1.4. The integral of the function represented in the plot is proportional to the Stokes V signal at a particular wavelength. The three curves correspond to any wavelength under the weak field approximation (the solid line), the wavelength where the average Stokes V signals is maximum (the dashed line), and the wavelengths where the HFS hump shows up (the dotted line). The units of the ordinates are relative since the curves have been scaled to the solid line when $B \to 0$.

Stokes V profiles present clear HFS humps (see Figure 4.6, the triple dotted-dashed lines).

In order to understand this behaviour one has to realize that the various magnetic field strengths existing in the atmosphere do not contribute to the observable signal in proportion to their magnetic flux, as expected if the weak magnetic field approximation would be satisfied (Eq. 4.3). The strong kG fields are always under-represented (§ 4.2), and this bias is particularly severe at line center where the HFS hump shows up. The effect is shown in Figure 4.7 which contains the integrand of Eq. 4.5 for one of the PDFs in Figure 1.4 (DC). The integrand is given in three cases, (a) assuming the weak field approximation to hold (the solid line), (b) at the wavelength where the average Stokes V is maximum (the dashed line), and (c) at the line core (the dotted line).

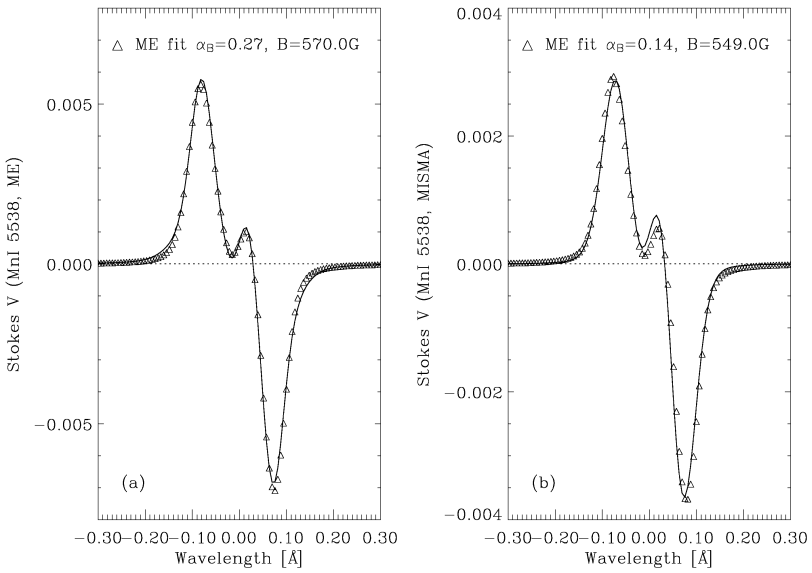

Figure 4.8: Least squares fits of Stokes V profiles synthesized in multi-component atmospheres (the solid lines) using single-component ME atmospheres (the symbols). (a) The multi-component Stokes V profile is synthesized in ME atmospheres. (b) The multi-component Stokes V profile is synthesized in model MISMAs. The values for α_B and B retrieved from the fits are included in the figures. The two synthetic profiles correspond to the same PDF (DC). The profiles are normalized to the quiet Sun continuum intensity.

4.3.1 On the diagnostic of HFS hump

The observations of Mn I λ5538 analyzed in the literature employ single component ME atmospheres (see § 1.2). The observed Stokes V profiles are fitted with synthetic profiles to obtain mean magnetic field strengths. In order to explore the diagnostic content of such inversion technique when applied to complex magnetic atmospheres, we developed a simple least squares minimization procedure to fit single-component ME profiles V_B to the synthetic multi-component V. The procedure fits

$$V = \alpha_B \cdot V_B, \tag{4.7}$$

where the factor α_B and the field strength B are the only two unknowns. Figure 4.8 shows the single-component ME fit of the multi-component Stokes V produced by the DC PDF. In the case that the syntheses are based on ME atmospheres (Figure 4.8a), the match is excellent. If the synthesis is based

on model MISMAs, the fit worsens a bit but still the agreement is fair (Figure 4.8b). In both cases the field strength resulting from the ME inversion is about 550 G. We have unsuccessfully tried to link this average magnetic field strength with a particular property of the underlying PDF (the solid line in Figure 1.4). It is neither the unsigned flux ($\simeq$ 150 G) nor the most probable field strength ($\simeq$ 13 G). In Figure 4.7, the solid line, shows $B \cdot P(B)$, i.e., the unsigned flux per unit of magnetic field strength. It peaks at 50 G and 1700 G which, again, do not seem to bear any obvious relationship with the average ME magnetic field strength ($\simeq$ 550 G).

In order to understand the relationship between the HFS hump and the magnetic fields existing in the multi-component atmosphere, we adopt a strategy avoiding ME fits. The presence or absence of a hump is certainly associated with the balance between weak fields and strong fields, but it is unclear how the hump is related with the fraction of atmosphere filled by weak and strong fields. One can quantify the presence of the hump using the derivative of the Stokes V profile at a wavelength λ_c slightly bluewards of the HFS maximum (i.e., centred in linear growth that ends up in the hump; see Figure 4.2a where $\lambda_c \simeq 0$). Then the sign of:

$$\frac{dV}{d\lambda}\Big|_{\lambda_c}, \tag{4.8}$$

indicates the presence (> 0) or absence (< 0) of a hump[9]. According to Eq. 4.5,

$$\frac{dV}{d\lambda}\Big|_{\lambda_c} = \int_0^{B_{\max}} \langle \cos\theta \rangle \, P(B) \, \frac{dV_B}{d\lambda}\Big|_{\lambda_c} \, dB, \tag{4.9}$$

so the slope of the mean Stokes V is just a weighted mean of the slopes that characterize each field strength. Consequently, $dV_B/d\lambda|_{\lambda_c}$ yields the contribution of each field strength to the sign of the mean profile or, in other words, it yields the contribution of each field strength to the presence or absence of a hump in the average profile.

We have applied Eq. 4.9 to understand the HFS humps of the synthetic profiles in Figure 4.6. Figure 4.9a shows the Stokes V derivative at line core ($\lambda_c = 0$) for the ME, the 1D and the MISMA model atmospheres. The magnetic field strength where this derivative is zero indicates when V_B changes from having to laking of a hump. As the figure shows, this transition field strength depends on the model atmosphere. The positive and negative lobes of the curves in Figure 4.9a have similar amplitudes, which indicates that for the average Stokes profile to lack of a hump, the filling factor of the

[9]This criterion assumes positive magnetic polarity, implying a positive Stokes V blue lobe. The same rule applies to negative polarity if one reverses the sense of the inequalities.

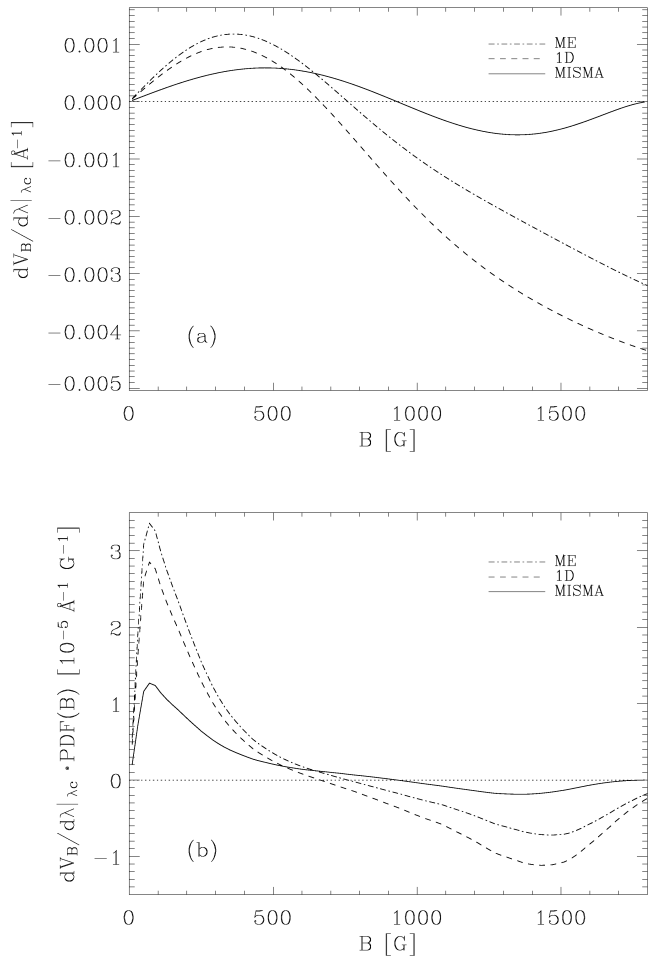

Figure 4.9: (a) Sensitivity of the HFS hump to the distribution of magnetic field strengths in the resolution element. The hump appears or goes away depending on the integral of $dV_B/d\lambda|_{\lambda_c}$ weighted with the PDF. The three curves correspond to the three model atmospheres used for multi-component synthesis (see the inset). (b) The derivative shown in (a) weighted with the V200 PDF. The integral is positive meaning that the resulting Stokes V profiles have HFS humps; see the triple dotted-dashed lines in Figure 4.6.

kG fields in the atmosphere has to be similar to the filling factor in weak fields. The requirement is not fulfilled by the PDFs in Figure 1.4, whose filling factors are dominated by weak fields. Such superiority explains why all profiles in Figure 4.6 show HFS humps. Eq. 4.9 also explains why the magnetic flux in the form of kG structures has to exceed by far the flux

in weak fields for the HFS hump to disappear. The HFS hump goes away when weak fields and strong fields have similar filling factors, but then the kG fields dominate the flux since the (unsigned) magnetic flux scales as the filling factor times the field strength. Among the three curves in Figure 4.9a, the one corresponding to MISMA model reflects the solar conditions best, since it includes the dimming of the line with increasing field strength. This curve has positive and negative lobes of approximately the same area, therefore, the presence-absence of HFS humps in the Mn I λ5538 Stokes V profiles is controlled by the fraction of photospheric atmosphere with field strengths smaller-larger than some 1 kG (i.e., the zero crossing point of the curve). Interpreting real observations with this rule-of-thumb requires disregarding the atmospheric volume having very weak magnetic fields, which produce no polarization and therefore do not contribute to the observed signal (see Figure 4.9b).

4.4 Mixed Polarities and Unresolved Velocities

We expect the quiet Sun resolution elements to contain mixed polarities (Sánchez Almeida & Lites 2000; Socas-Navarro & Sánchez Almeida 2002), which leads to a reduction of the Stokes V signals. In the multi-component approximation framework (Eq. 4.5), having unresolved mixed polarities implies,

$$\langle \cos\theta \rangle \ll \langle |\cos\theta| \rangle, \tag{4.10}$$

since positive and negative $\cos\theta$ tend to cancel when carrying out the averages. If the positive polarity ($\cos\theta > 0$) and the negative polarity ($\cos\theta < 0$) have the same distribution of inclinations but they fill different fractions of resolution element, then

$$\langle \cos\theta \rangle = \langle |\cos\theta| \rangle \, (2f - 1), \tag{4.11}$$

with f the fraction filled by the magnetic fields of positive polarity. If f does not depend on the magnetic field strength, the effect of mixed polarities is only a global scaling of the Stokes V profile with no effect on Stokes I (Eqs. 4.4, 4.5, and 4.11). However, the above view of the effect produced by unresolved mixed polarities is too simplistic. It implicitly neglects the existence of unresolved velocities in the resolution element coupled with changes of polarity. When the sense of the velocity and the polarity are correlated, the Stokes V of opposite polarities are Doppler shifted. They do not perfectly cancel, leaving observable residuals. Such coupling has been observed

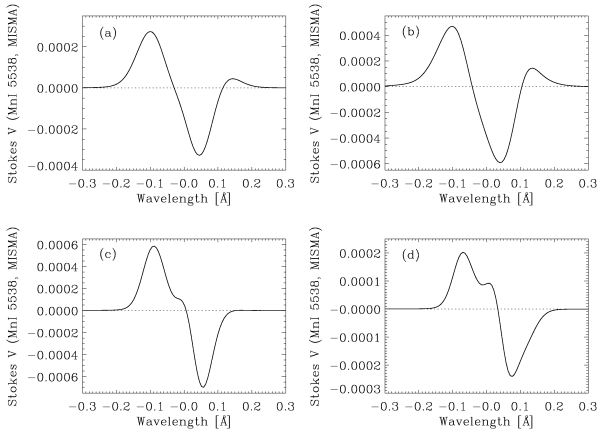

Figure 4.10: Examples of Stokes V profiles synthesized in semi-empirical model MISMAs having unresolved mixed polarities correlated with velocities. They correspond to different classes in Sánchez Almeida & Lites (2000): (a) class 6, (b) class 9, and (c) class 7. (d) Offspring of the class 7 model atmosphere where the two polarities have the same sign and the velocity difference has been increased. The profiles are normalized to the quiet Sun continuum intensity.

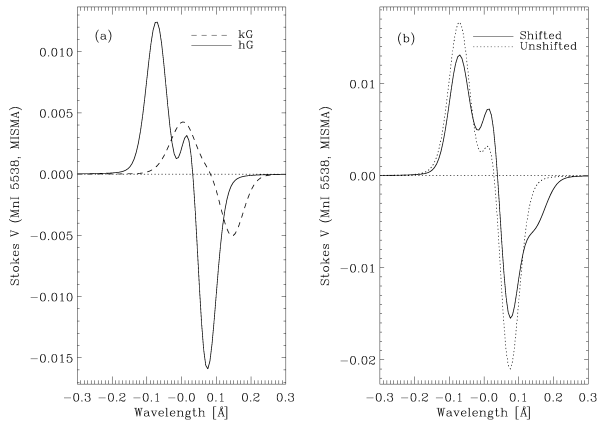

Figure 4.11: Two component Stokes V synthesis of weak and strong fields having different Doppler shifts. The strong fields are blueshifted with respect to the weak fields (a). The sum of the profiles in (a) leads to the profiles in (b), the solid line. If the relative Doppler shift is not considered, then the average Stokes V corresponds to the dotted line in (b). The profiles are normalized to the quiet Sun continuum intensity.

in Fe I lines, and it produces very asymmetric Stokes V profiles (Sánchez Almeida & Lites 2000). In order to illustrate the effect, Figure 4.10 shows Stokes V profiles of Mn I λ5538 synthesized in empirical model MISMAs with mixed polarities and different velocities (Sánchez Almeida & Lites 2000).
Velocities and other magnetic quantities are also expected to be coupled. For example, strong kG fields appear in intergranular lanes with downflows, whereas weak fields prefer granules with upflows (e.g., Cattaneo 1999). This combination of Doppler shifts and magnetic field strengths renders profiles like the two component average shown in Figure 4.11b, the solid line. It corresponds to the sum of the profiles in Figure 4.11a, which are shifted by some 3.5 km s^{-1}. The HFS hump now appears elevated from the zero level, and the Stokes V blue wing is broadened with a conspicuous double absorption structure. These two features are common among the observed Stokes V profiles of Mn I λ5538 (López Ariste et al. 2006, Figures 8 and 9). The same features appear in the MISMA synthesis of Figure 4.10d.
In short, mixed polarities and velocity gradients are properties of the real quiet Sun magnetic fields that affect the observed polarization in a significant way. They are not easy to deal with but must be taken into account for a realistic interpretation of the observations.

4.5 Synthesis of other Mn I Lines

The purpose of synthesizing Mn I lines different from Mn I λ5538 is threefold. First, it confirms that our LTE syntheses reproduce all kinds of observed HFS patterns. Second, it offers a chance to explore whether other Mn I lines show a sensitivity to magnetic fields complementary to Mn I λ5538. Finally, it proves that the uncertainty of the HFS constants do not limit the use of Mn I lines for magnetometry.
All the syntheses in this section employ the non-magnetic quiet Sun MISMA that reproduces the Mn I λ5538 profile in Figure 4.1. Varying the macroturbulence and, in some cases also tuning the oscillator strength, we managed to fit the observed Stokes I profiles of all the lines we tried. A total of eight Mn I lines reproduced by the code are shown in Figures 4.12 and 4.13. They are split in two sets; Figure 4.12 includes lines without obvious HFS features in the observed solar spectrum, whereas Figure 4.13 shows lines with varied and assorted HFS. The agreement between the synthetic profiles and the solar atlas is good, an impression reinforced by the fact that the HFS constants determining the HFS patterns have not been tuned, but they come directly from the literature (Table 4.1).
The dependence of the various lines on magnetic field strengths has been

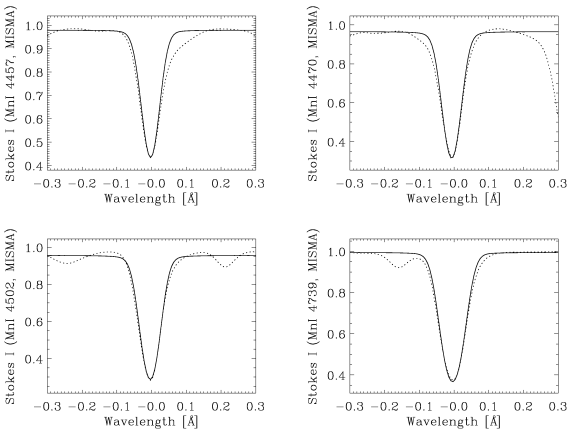

Figure 4.12: Mn I lines without obvious HFS features in the observed solar spectrum. The solid lines show our syntheses whereas the dotted lines correspond to the solar atlas. Wavelengths, given in Å, are refereed to the laboratory wavelength of the lines. Each line is identified by the wavelength in the label of the ordinate axis. The profiles are normalized to the quiet Sun continuum intensity.

studied by synthesizing them in the magnetic quiet Sun model MISMA used in § 4.3, increasing the field strength from $\simeq$ 100 G to $\simeq$ 2000 G. All the lines share a common behaviour: they weaken with increasing field strength, and the HFS features tend to disappear. This behaviour is also shared by the near infrared line Mn I λ15262 recently pointed out by Asensio Ramos et al. (2007) (Figure 4.13, bottom right). On top of this general trend, and depending on the actual HFS constants, the Stokes V profiles of different lines present specific features. The line Mn I λ5516 behaves like Mn I λ5538, with a single HFS reversal at the line core. Then it is possible to relate the presence or absence of the hump with the distribution of field strengths in the atmosphere, exactly as the analysis carried out in § 4.3.1. The patterns of Mn I λ5420 and Mn I λ8741 are more complicated, and we have not been able to agree on a particular feature of the Stokes V profiles that can be treated as in § 4.3.1.

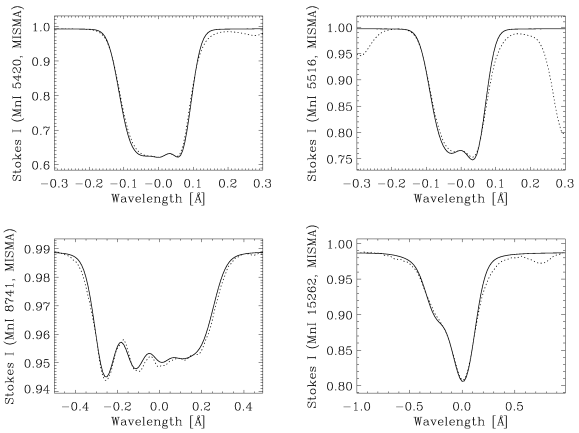

Figure 4.13: Mn I lines with HFS features. The solid lines correspond to our syntheses whereas the dotted lines show the solar atlas. Wavelengths, given in Å, are refereed to the laboratory wavelength of the lines. Each line is identified by the wavelength in the label of the ordinate axis. The profiles are normalized to the quiet Sun continuum intensity.

Fe I λ6301 and Fe I λ6302 lines are the most commonly used lines for spectropolarimetric observations of the solar photosphere (§ 1.2.1) and maybe the lines that are known better due to their ordinary use.
In § 4.6 – § 4.9 we'll report the preliminary results retrieved by the inversion under the MISMA hypothesis (Sánchez Almeida et al. 1996) of Stokes I and V profiles of Fe I λ6301 and Fe I λ6302 lines observed at solar disk center with the spectropolarimeter of the Solar Optical Telescope aboard the HINODE satellite (Lites et al. 2001; Kosugi et al. 2007). The complete analysis has, as a final goal, the definition of a PDF for the statistical description of the quiet Sun magnetic field vector for a direct comparison with recently published results reported in Orozco Suárez et al. (2007).

4.6 HINODE Satellite and SOT/SP Instrument

The HINODE spacecraft (formerly Solar-B) of the Institute of Space and Astronautical Science, Japan Aerospace Exploration Agency (ISAS/JAXA), was launched on 22 September 2006, at 21:36 GMT. The principal scientific goals of the HINODE mission are the following:

- To understand the processes of magnetic field generation and transport

including the magnetic modulation of the Sun's luminosity.

- To investigate the processes responsible for energy transfer from the photosphere to the corona and for the heating and structuring of the chromosphere and the corona.

- To determine the mechanisms responsible for eruptive phenomena, such as flares and coronal mass ejections, and understand these phenomena in the context of the space weather of the Sun-Earth System.

This mission is the follow-on to Yohkoh, an ISAS mission with significant NASA and United Kingdom participation that was launched in 1991 (Ogawara et al. 1991) and continued taking observations for nearly a solar cycle.
HINODE is designed to address the fundamental question of how magnetic fields interact with the ionized atmosphere to produce solar variability. Measuring the properties of the Sun's magnetic field is the fundamental observational goal of HINODE and differentiates it from previous solar missions. Three instruments were selected to observe the response of the chromosphere and corona to changes in the photospheric magnetic field. To achieve this end HINODE makes quantitative measurements of all three components of vector magnetic fields. This allows calculation of the free energy of the magnetic field, which powers solar activity through the action of electric currents. The major scientific instrument on HINODE, the Solar Optical Telescope (SOT), makes these observations from space. The response of the solar atmosphere to magnetic field changes is measured by the EUV Imaging Spectrometer (EIS) and the X-Ray Telescope (XRT).
The SOT is the largest solar optical telescope flown in space (Tsuneta et al. 2008). It consists of the Optical Telescope Assembly and its Focal Plane Package (Suematsu et al. 2008; Tarbell 2007). The Optical Telescope Assembly is a 50-cm clear aperture telescope with a diffraction limit of $0.2'' - 0.3''$ between 3880 Å and 6700 Å. The Focal Plane Package has four optical paths: the Narrowband Filter Imager (NFI), the Broadband Filter Imager (BFI), the Spectro Polarimeter (SP), and the Correlation Tracker (CT); here we focus our attention on the SP spectropolarimeter.
In detail, the SP instrument (Lites et al. 2001) obtains Stokes profiles of the two magnetically sensitive Fe I lines at 6301.5 Å and 6302.5 Å and nearby continuum, using a $0.16'' \times 164''$ slit that can move to map an area up to the full $320''$ wide field of view. The SP only has a few modes of operation: Normal Map, Fast Map, Dynamics, and Deep Magnetogram. The Normal Map mode produces polarimetric accuracy of 0.1 % with the spatial sampling of $0.16'' \times 0.16''$. It takes 83 min to scan a $160''$ wide area: enough to cover a moderate-sized active region. By reducing the scanning size, the cadence

becomes faster (50 sec for mapping of 1.6″ wide area), which can be useful for studying dynamics of small magnetic features. The Fast Map mode of observation can provide 30 min cadence for the 160″ wide scanning with polarimetric accuracy of 0.1 % but 0.32″ resolution. The Dynamics mode of observation provides higher cadence (18 sec for 1.6″ wide area) with 0.16″ resolution, although at lower polarimetric accuracy. The Deep Magnetogram mode achieves a very high polarization accuracy at the expense of time resolution. In spite of its high polarimetric accuracy and spatial resolution, an important limit of the SOT/SP instrument is the absence of a temporal coherence of observations. In fact, only by reducing the scanning size down to few arcseconds it is possible to obtain "instantaneous" measurements (here "instantaneous" means on times shorter than the granulation timescale, i.e. about 10 min). This doesn't permit an appropriate study of the temporal evolution of magnetic fields over extended fields of view.

4.7 The Dataset

The selected dataset consists of full Stokes measurements of a quiet Sun region of about 302″ × 162″ observed at disk center on March 10 between 11 : 37 UT and 14 : 37 UT. The spectropolarimeter SP aboard of HINODE obtained polarization profiles of Fe I lines at 6301.5 Å and 6302.5 Å in the Normal Map mode (see § 4.6) with a wavelength sampling of 2.15 pm pixel^{-1} and a scanning step of 0.1476″. The used exposure time for slit position is 4.8 s. The data reduction and calibration have been performed by the `sp_prep.pro` routine (Ichimoto et al. 2008) available in the SolarSoft. The routine corrects the data for the dark current, flat field and instrumental cross talk. The wavelength axis for the Stokes profiles is the same used in Orozco Suárez et al. (2007); to obtain a correct wavelength calibration a correction for the gravitational redshift of 613 m s^{-1} is needed.

We first evaluated the values for the continuum (I_C) and the noise level for the Stokes Q, U and V parameters (respectively σ_Q, σ_U and σ_V, normalized to I_C). The calculation has been performed taking into account the whole dataset by evaluating the mean of Stokes I and the standard deviation of Stokes Q, U and V in the spectral range $6302.92 - 6303.14$ Å, considered a good continuum range. The values for the noise level is 1.1×10^{-3} in Stokes V and 1.2×10^{-3} in Stokes Q and U. The continuum image of the dataset is shown in Figure 4.14. It presents an rms intensity contrast of $\simeq$ 7.4%. The values for the rms intensity contrast, I_C, σ_Q, σ_U and σ_V are in full agreement with Orozco Suárez et al. (2007) and Lites et al. (2008). Our domain has a

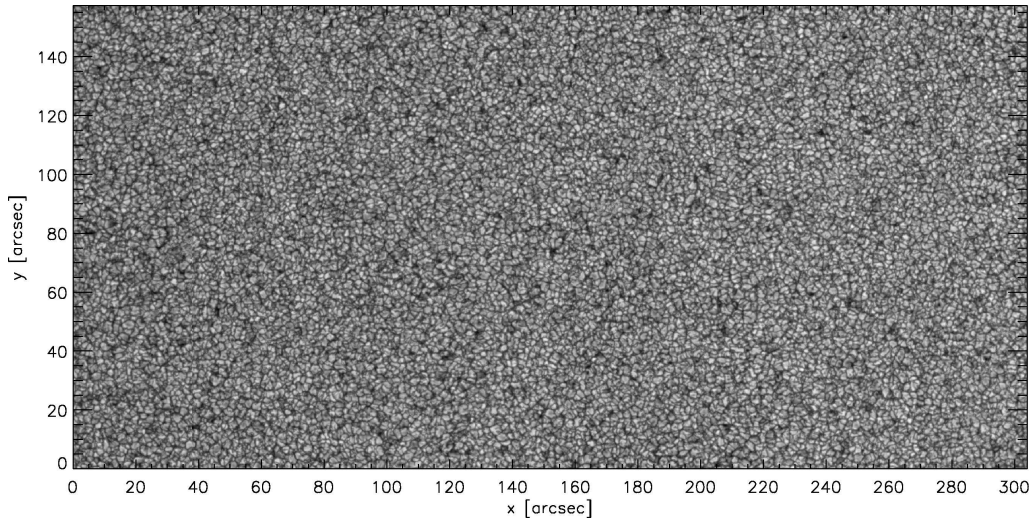

Figure 4.14: Continuum intensity I_c from the dataset. The image has been obtained by averaging the intensity profiles in the spectral range $6302.92 - 6303.14$ Å at each point of the field of view.

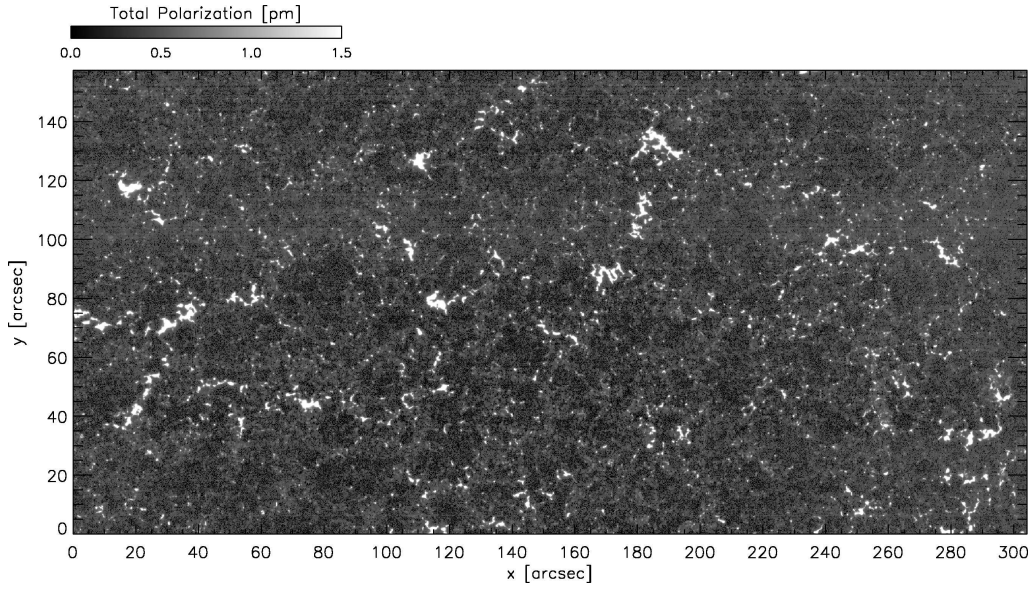

Figure 4.15: Total polarization signal from the dataset. The grey scale bar reported in the figure is expressed if pm and saturates at 1.5 pm. Null polarization is associated to the regions where the maximum amplitude of polarization is smaller than three times the associated noise level. The null polarization region is about 16% of the total image.

reduced Y dimension compared with the figure in Lites et al. (2008) because we exclude from the analysis a part of the dataset (30 $\times$ 2048 pixel) due to problems at the upper and lower margins of the slit (see the base of Figure 1 in Lites et al. 2008).
An important aspect in the calculation of the noise level of the different Stokes parameters is related to the correction for the gravitational redshift. In fact, shifting the data, on the original wavelength domain, by an interpolation (e.g., interpol or spline function of IDL) causes the reduction of the noise level (e.g., $\sigma_V = 0.8 \times 10^{-3}$ instead of 1.1×10^{-3}). For this reason we applied the correction directly on the wavelength domain maintaining unchanged the data. This does not cause problems for the inversion that needs just the Stokes profiles as functions of wavelength to work correctly.
To visualize the polarization pattern, we represent the map of the total polarization calculated as $\int (Q^2+U^2+V^2)^{1/2} d\lambda / I_C$ shown in Figure 4.15. It has been defined considering the regions whose linear or circular polarization is larger than three times the noise associated to the corresponding polarization state. About 84% of the image presents polarization signals which fulfil this requirement. We forced the values of the polarization to saturate at 1.5 pm while the maximum polarization values reach $\simeq$ 6 pm. In Figure 4.15 the network pattern is clearly recognizable as saturated and connected features; in § 4.9 we'll describe a method to separate the network component of the dataset from the quiet Sun one.

4.8 The MISMA Inversion

The analysis of the dataset has been performed adopting an inversion technique based on the MISMA hypothesis already introduced in § 4.1. More in detail, the code used for the analysis is the same adopted for the syntheses of Mn I lines. Here, on the contrary, the code is used to fit Stokes I and V profiles observed by HINODE SOT/SP.
The inversion code under the MISMA hypothesis was developed by Sánchez Almeida (1997). It solves Eq. 4.2 under LTE. The inversion has been carried out taking into account both Fe I lines and adopting, as initial guess models, the ones proposed in Sánchez Almeida & Lites (2000) characterized by the following properties:

- There are $N = 3$ distinct components defining a single model atmosphere. One non-magnetic component and two magnetized component. The two magnetized components have the aim of describing the statistical properties of a distribution of magnetic field strengths that is supposed to exist in one pixel of our dataset. The single non-magnetic

component represents the field free photospheric environment which is considered to produce the non-polarized scattered light contribution (also named stray light).

- The magnetic field components have vertical magnetic fields since here we want to invert exclusively Stokes I and V profiles and since Stokes Q and U carry most of the information of the orientation of the magnetic field vector.

- The temperature of the three components of the atmosphere is the same at every geometrical height, i.e.,the radiative exchange between the MISMA components equilibrate the temperatures over typical timescales of the order of few seconds (Spiegel 1957).

- The three components are in lateral pressure equilibrium at every height, which means that they have the same total pressure (magnetic pressure plus gas pressure). This condition automatically puts into relation magnetic field strength and thermodynamics. This constraint plus the assumption of hydrostatic equilibrium along the field line provide the stratification of the magnetic field strength once specified one value at a certain height.

- Plasma motion along the line of sight is allowed for each component.

In spite of the complexity of the model outlined above a full description of the MISMA scenario is realized by means of the following quantities. The temperature profile is defined by four nodes at four fixed heights. The parameters for each component of the atmosphere are inferred from conditions imposed at the base of the integration domain. More in detail, for each component the code controls the magnetic field strength, the occupation fraction, the velocity along the line of sight, the Doppler width and the damping constant. Note that the magnetic field inclination and azimuth are not considered for the inversion since they are fixed parameters. To take into account the effect of stray light, macroturbulence and instrumental broadening (due to limited spectral resolution) three more quantities are needed. The resulting number of free parameters of such a model is 20, a number comparable with the number of free parameters used by other inversion codes (e.g., Bellot Rubio et al. 1997; Frutiger & Solanki 1998).

The adopted inversion strategy is extremely simple at this stage. We refer to a subset of seven models selected among the ten MISMA models of Sánchez Almeida & Lites (2000) as starting models to invert each observed

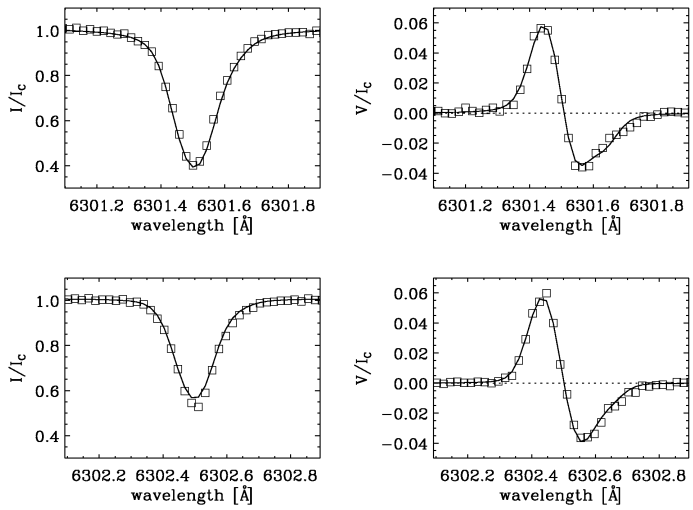

Figure 4.16: Inversion of Stokes I and V profiles for the Fe I lines at 6301.5 Å (*upper row*) and 6302.5 Å (*lower row*). The synthetized profiles are represented with solid lines while the data are represented with squares.

profile. The discarded models are the ones used by the authors to represent extremely complex profiles. After performing seven inversions for each profile, the model atmosphere considered representative for that profile profile is the one able to fit it with the minimum χ^2 among the seven different inversions performed. Once obtained the model atmosphere we are able to obtain information about the magnetic field strength at the photosphere. Two examples of the inversion of observed profiles, and of the model atmosphere obtained from the same inversion, are reported in Figure 4.16 and Figure 4.17 respectively.
Deriving the magnetic field strength at the base of the photosphere in a model as the one shown in Figure 4.17 is straightforward. Because of the lateral pressure balance with the non-magnetic quiet Sun, the base corresponds to the height where the total gas pressure is $P_g = 1.3 \times 10^5$ dyn cm^{-2}.

4.9 Preliminary Results

The inversion strategy described above has been successfully applied to invert about 15000 profiles to obtain two main results. The first one is a preliminary PDF for the magnetic field strength representative of the statistical proper-

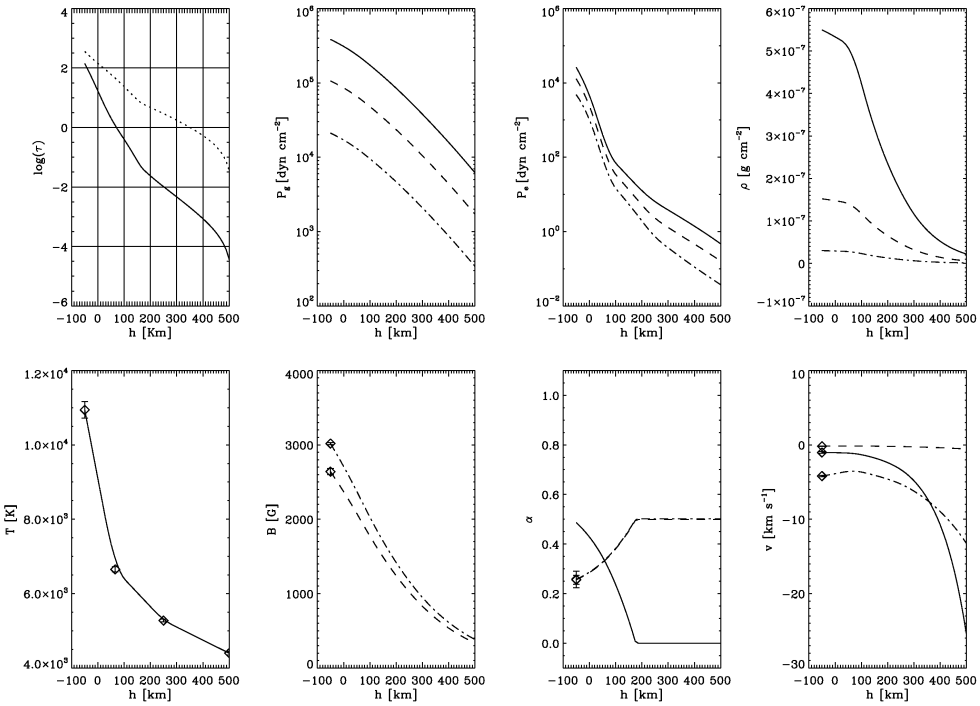

Figure 4.17: Model MISMA retrieved from the inversion of the profiles in Figure 4.16. The logarithm of the continuum optical depth (solid line) and the line center optical depth (dotted line) are reported in the top-left panel. The remaining panels represent the stratification of gas pressure P, electron pressure P_e, gas density ρ, temperature T, magnetic field strength B, occupation fraction α and plasma velocity along the line of sight v for the different components of the model MISMA. Each component is represented with different type of line.

ties of the observed field of view. The second one are two maps of magnetic field values obtained from the inversion of two selected square regions having dimension of $15''$.

The preliminary PDF for the magnetic field strength has been obtained by inverting a total of 8000 profiles. These have been picked up randomly from the whole dataset with the only constraint that both Stokes V profiles of the two Fe I lines to have a maximum amplitude larger than $3 \cdot \sigma_V$ (see § 4.7). The main results obtained from this inversion are reported in Figure 4.18 and Figure 4.19.
Figure 4.18 has been defined taking into account both values of the magnetic field strength retrieved by the inversion code for each profile. More exactly,

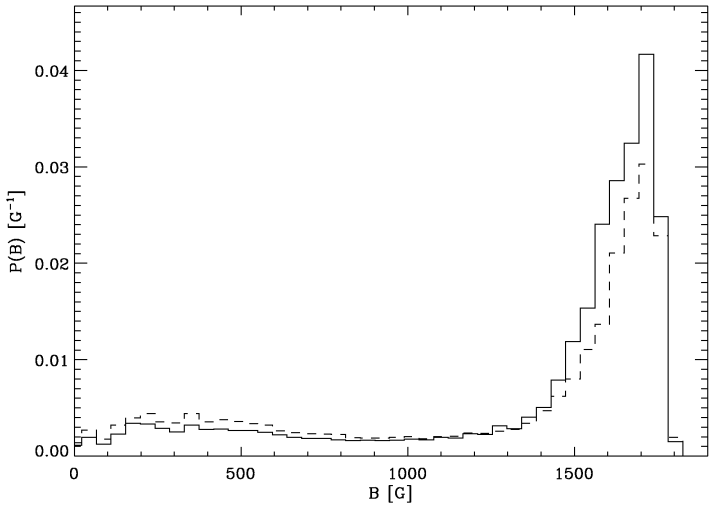

Figure 4.18: PDF of the magnetic field strength obtained from the inversion of 8000 profiles randomly selected in the field of view shown in Figure 4.15. The solid line represents the statistics defined over the whole dataset while the dashed line represents the statistics defined selecting quiet Sun regions.

the contribution of each value of B to the definition of the PDF is equal to the filling factor of the corresponding magnetized component of the model atmosphere. The two histograms reported in Figure 4.18 have been defined taking into account the whole set of $2 \cdot 8000$ magnetic field values (solid lines) and a sub-set of values selected from quiet Sun regions (see § 1.2) using the following procedure.

From Harvey-Angle (1993), we know that quiet Sun magnetic fields occupy more than 90% of the solar photosphere. Referring to this information we defined a simple procedure to cut from the total polarization image the non quiet Sun contribution. The procedure is divided in two steps. First, we calculate a threshold on the total polarization over which we are able to cut few percents of the total field (e.g., 2%). Once found this threshold we are able to define a two level image with connected regions related to the network pattern. In the second phase we check the size of each network region. If a region is formed of a number of pixels smaller than ten we consider it as a quiet Sun region. The number of pixels defining the thresholdhas been set arbitrarely. After the second phase the fraction of cut surface is $\simeq 1.7\%$ (slightly less than 2%). In this way we are taking into account concentrated regions with high polarization signals typically found in the interior of net-

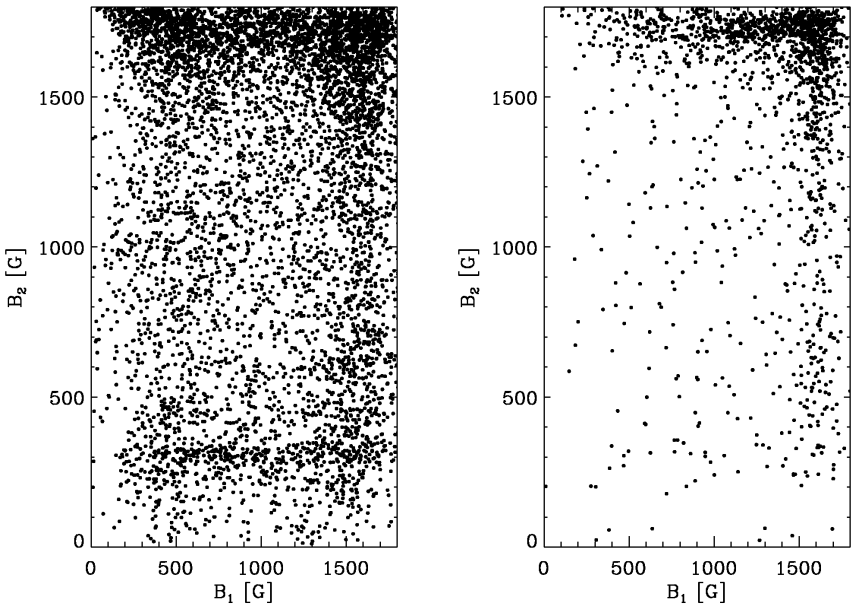

Figure 4.19: Scatter plots defined from the values of the magnetic field strengths (B_1 and B_2) for the two magnetized components of the 8000 model atmospheres retrieved from the inversion. Each point of the scatter plots is defined by a couple of values of magnetic fields. The *left panel* has been defined taking into account the whole dataset while the *right panel* has been defined over the network regions.

work cells. To complete the procedure we dilated the network regions with a circular kernel having a diameter of ten pixels. The result of the masking is reported in Figure 4.20. At the end of the procedure we are able to mask $\simeq 8\%$ of the whole field of view.

The dashed line PDF in Figure 4.18 obtained from the inversion of the two visible Fe I lines reveals a quiet Sun dominated by strong kG fields. This result is in full agreement with the results obtained by Sánchez Almeida et al. (2003a) when applying the MISMA code to invert the same two lines observed using the Vacuum Tower Telescope and THEMIS telescopes at the Observatorio del Teide. On the contrary, the preliminary PDF we propose here differs from the one reported in Orozco Suárez et al. (2007) in which the authors inverted the whole dataset by means of a ME code; in fact, the quiet Sun magnetic field PDF they obtained presents a maximum for weak hG fields. An important point that is worth noting in this discussion is that Orozco Suárez et al. (2007) performed the full Stokes inversion of the

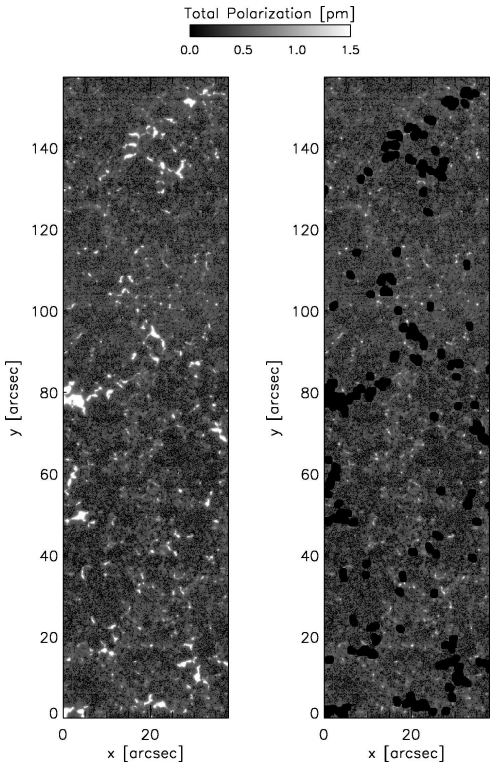

Figure 4.20: *Left panel*: total polarization image for a portion of Figure 4.15. The grey scale bar reported in the figure is expressed if pm and saturates at 1.5 pm. *Right panel*: same region of the left panel, dark regions represent the erased network contribution obtained with our selection procedure.

dataset concluding on the nearly horizontal nature of quiet Sun magnetic fields. Our inversion is "blind" to this component of the magnetic field revealed by HINODE SOT/SP so that we expect to be able to reveal the presence of hG fields from a full Stokes inversion performed by the code we adopted.

In Figure 4.19 we reported two scatter plots in which each point is defined by the two values of the fields of the magnetized components of each model atmosphere obtained from the inversion of the dataset. In the left panel we represented the results from the whole dataset while, in the right panel, the network component, selected as done for Figure 4.18, is reported. For network profiles the points are grouped mainly in the upper-right corner of the $B_1 - B_2$ domain. This means that the code is using two strong kG components to represent network regions. On the contrary, in quiet Sun regions hG and kG fields coexist spreading the points all over the same domain.

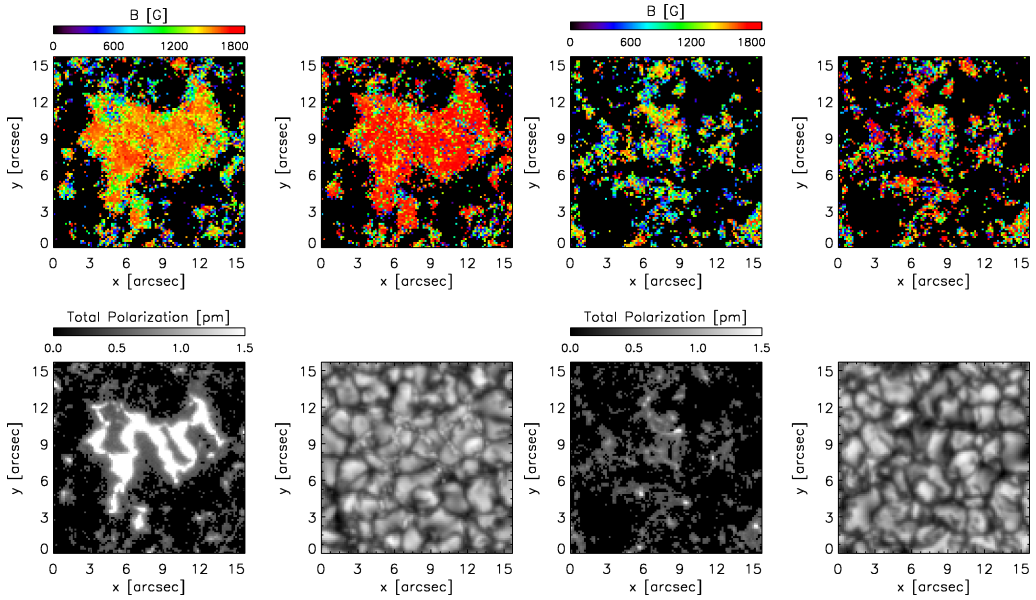

Figure 4.21: Magnetic field maps for the two magnetized components obtained from the inversion. The selected panels are representative of a network region (*four panels on the left*) and quiet Sun region (*four panels on the right*). Both the panels are composed of four images: absolute value of the magnetic field at the photosphere for the first magnetized component (*upper left*) and second magnetized component (*upper right*) respectively. The lower left images show the total polarization emerging from the regions while the lower right images show the continuum.

These results are in agreement with the maps in Figure 4.21 in which two examples of network and quiet Sun regions respectively are reported. The maps have been obtained by inverting about 7000 profiles. The network patch consists of strong kG fields while the quiet Sun region hG and kG coexist. B_2 values are typically larger than B_1 values; this is due to the initial conditions which define the starting point of the inversion. It is worth noting how, in the quiet Sun region, B_2 is large where the total polarization image shows high values.

In § 4.10 – § 4.15 we analyze the formation of the solar Mn I λ5395 line in the context of its global sensitivity to solar activity, a subject which has received considerable attention based on the extensive observations of this line by Livingston and coworkers and Vince and coworkers (Livingston & Wallace 1987; Vince & Erkapic 1998; Danilovic et al. 2005; Vince et al. 2005a,b; Livingston et al. 2007). More than fifty years ago Abt (1952) pointed out that the unusual widths of Mn I lines in the solar spectrum are due to hyperfine structure, as found also in § 4.5. In the following discussion we'll show how Abt's hyperfine structure is the key to understand the activity sensitivity of Mn I λ5395 through the reduction of spectral-line sensitivity to thermal and convective Dopplershifts outside magnetic concentrations.

4.10 Activity Modulation

Livingston's inclusion of the Mn I λ5395 line into his long-term full-disk "sun-as-a-star" line profile monitoring from 1979 onwards was suggested by Elste who had pointed out that their large hyperfine structure makes the Mn I lines less sensitive to the questionable microturbulence parameter than other ground-state neutral-metal lines that may serve as temperature diagnostic (Elste & Teske 1978; Elste 1987). It turned out that this line is the only photospheric line in the Kitt Peak full-disk monitoring that shows appreciable variation with the cycle, in good concert with the Ca II full-disk intensity variation. Livingston & Wallace (1987) found that its equivalent width in the irradiance spectrum varies by up to 2%. Figure 16 in the overview paper by Livingston et al. (2007) displays the variation in line center depth (as fraction of the continuum intensity measured from the latter, upside down and therefore labelled central intensity) during the two monitoring periods without problematic instrument changes. The same data are plotted as line depth in Figure 2 of Danilović et al. (2007), overlaid by a theoretical modelling curve. The line-center intensity increases about 2% from cycle minimum to maximum, slightly more than the corresponding decrease in equivalent width.
Vince et al. (2005a) used observations at the Crimea Observatory including Zeeman polarimetry to measure the changes in Mn I λ5395 line between plages with different apparent magnetic flux density. They found that the line weakens with increasing flux, as concluded already by Elste & Teske (1978) and Elste (1987). The full width at half maximum of the line-depth profile does not change much, so that the equivalent width weakening tracks the line-center brightening.

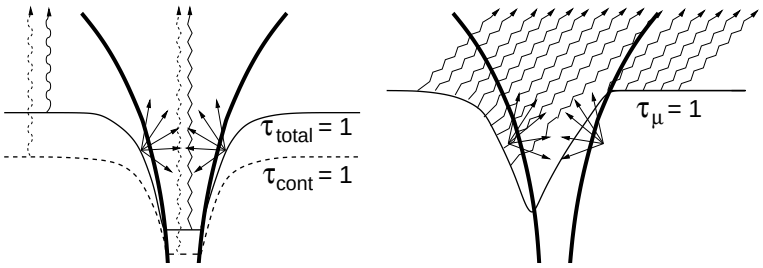

Figure 4.22: Schematic G-band bright-point enhancement in a magnetic concentration, portrayed here as a vertical cut through an idealized flaring fluxtube (thick curves) containing strong field, embedded in field-free quiet photosphere. *Left Panel*: in radial viewing the Wilson depression due to magnetic-pressure evacuation deepens the photon escape layer characterized as $\tau = 1$ surface to far below the outside surface. The magnetic concentrations are much cooler there than the subsurface surroundings due to suppressed convection, but hotter than the outside photon escape layer due to the large depth and hot-wall irradiation, and have flatter temperature gradients. The correspondingly larger degree of dissociation of the CH molecules that make up the G-band cause a yet larger effective Wilson depression in this spectral feature, producing larger brightness enhancement than in the continuum. *Right Panel*: In near-limb viewing the same lack of opacity along the slanted line of sight causes deeper, facular "bright-stalk" sampling of hot granules behind magnetic concentrations. Courtesy of Rutten (1999), see also Figure 1 of Spruit (1976).

4.11 Photospheric Interpretation

Height of formation estimates for the optical Mn I lines based on standard modelling suggests that they are purely photospheric (Gurtovenko & Kostyk 1989; Vitas 2005). Observational evidence that Mn I λ5395 is photospheric has been collected by Vince et al. (2005b) who showed that Mn I λ5395 bisectors show characteristic photospheric shapes and center-limb behaviour, and by Malanushenko et al. (2004) who compared spectroheliogram scans in Mn I λ5395 and the nearby Mn I λ5420 line with other lines and a magnetogram. The Mn I lines show network bright, closely mimicking the unsigned magnetogram signal which is purely photospheric. These observational indications of photospheric formation suggest that the propensity of Mn I lines to track solar activity in their line-center brightness may be akin to the contrast brightening that network and plage show in the G-band. We therefore summarize G-band bright-point formation, where bright points stands for kG magnetic concentrations (§ 1.2.1). Bright-points enhanced photospheric brightness in continuum intensity and further contrast increase in

G-band imaging has been studied in extenso and is well understood, both for their on-disk appearance as filigree and near-limb appearance as faculae. A brief review with the key references is given in the introduction of de Wijn et al. (2005); the cartoon in Figure 4.22 schematizes the explanation in terms of the magnetostatic fluxtube paradigm of Zwaan (1967) and Spruit (1976). The latest numerical verifications of this concept are the MHD simulations of Keller et al. (2004), Carlsson et al. (2004), and Shelyag et al. (2004). The upshot is that the G-band shows magnetic concentrations with enhanced contrast because its considerable line opacity lessens through molecular dissociation within the concentrations while its LTE formation implies good temperature mapping. Hence, for manganese we seek a property that enhances the reduction of line opacity in fluxtubes over that in comparable lines say from Fe I lines, enhancing the corresponding "line gap" phenomenon. A first consideration is that Mn I is relatively sensitive to temperature, as pointed out already by Elste & Teske (1978), because it originates from a neutral-metal ground state. In addition, Mn I λ5395 is also a somewhat forbidden intersystem transition which makes its source function obey LTE more closely than for higher-probability lines. However, both these properties are unlikely to play an important role since Malanushenko et al. (2004) found that Mn I λ5420, a member of multiplet 4 at 2.14 eV excitation, brightens about as much in network.

The obvious remaining property which makes Mn I lines differ from others is their large hyperfine structure. How can this cause unusual brightness enhancement in strong-field magnetic concentrations? Elste & Teske (1978) pointed out that it lessens sensitivity to the "turbulence" that was needed to explain other lines in classical one-dimensional modelling of the spatially-averaged solar spectrum. The illfamous microturbulence and macroturbulence parameters are supposed to emulate the reality of convective and oscillatory inhomogeneities which affect Fraunhofer lines and make a solar-atlas line profile represent a spatio-temporal average over widely fluctuating and Dopplershifted instantaneous local profiles. Lines that should be deep and narrow are so smeared into shallower depressions. However, lines that are already wide intrinsically through hyperfine broadening suffer less shallowing by being less sensitive to Dopplershifts. The culprit may therefore not be the hyperfine structure of Mn I lines but rather the heavy hydrodynamic smearing of all the other, narrow lines that occurs in the granulation outside magnetic concentrations. We test this idea below and find it is correct, turning the analysis into a discussion of general Fe I line formation rather than specific Mn I line formation.

Table 4.2: Line parameters .

Line	Mn I	Fe I
Wavelength [Å]	5394.67	5395.21
Transition	$a^6S_{5/2} - z^8P^0_{7/2}$	$z^5G^0_2 - g^5F_1$
Excitation energy [eV]	0.0	4.446
$\log gf$	-3.503	-1.74
Landé factor lower level	2.001	0.335
Landé factor upper level	1.938	0.0
$\mathcal{A}_{\rm low}$ [10^{-3} cm^{-1}]	-2.41	–
$\mathcal{A}_{\rm up}$ [10^{-3} cm^{-1}]	18.23	–
Ionization energy [eV]	7.44	7.87
Abundance	5.35	7.51

4.12 Assumptions and Methods

We started the analysis with a wider line selection but for the sake of clarity and conciseness we limit our analysis to Mn I λ5395 and the neighbouring Fe I λ5395 line, following the example of Danilović et al. (2007) who show and modelled the activity modulation of both lines in parallel. The Fe I λ5395 line serves here as prototype for all comparable narrow lines. The line parameters are given in Table 4.2. The Mn I λ5395 hyperfine structure constants $\mathcal{A}$ come from Blackwell-Whitehead et al. (2005). All other values were taken from the NIST (see reference in Table 4.1).

4.13 Line Synthesis

We perform line synthesis in the presence of magnetic fields with the code of described in § 4.1 which is able to solve the radiative transfer equation for polarized light in a given one-dimensional atmosphere. It yields the full Stokes vector but here we only use the intensity. The code includes evaluation of the Zeeman pattern for lines with hyperfine structure using the routine of Landi degl'Innocenti (1978). We consider $\mathcal{B}$ negligible here, again following the synthesis procedure adopted in § 4.1 that successfully reproduces multiple Mn I line profiles with different HFS patterns (see § 4.5).

4.13.1 1D Modelling

We use the standard model for fluxtubes making up plage that was derived in the 1980s by Solanki and coworkers from spectropolarimetry of photospheric lines (Solanki 1986; Solanki & Steenbock 1988; Solanki & Brigljevic 1992). Since we only intend demonstration here, we do not apply spatial averaging

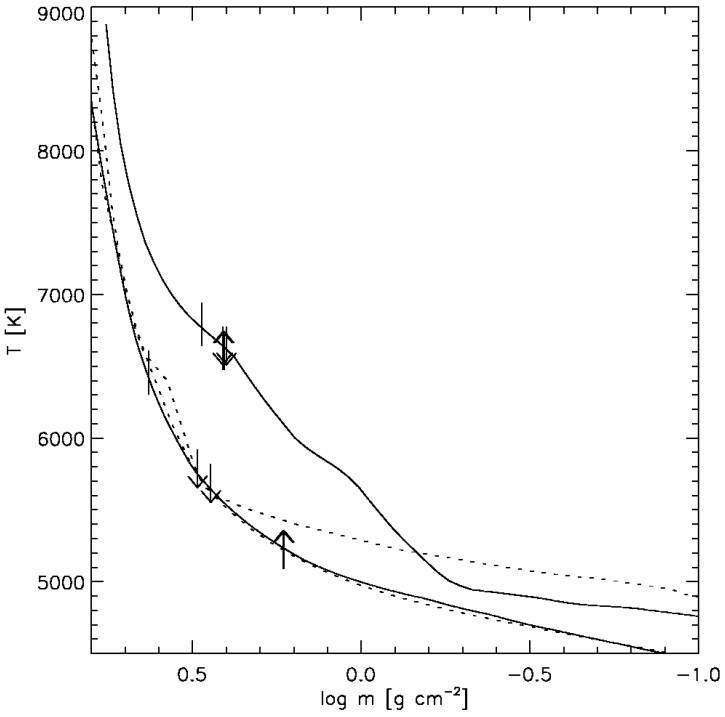

Figure 4.23: 1D standard models plotted as temperature against column mass density. The solid curve is the quiet Sun model by Maltby et al. (1986), the dashed curve is the plage model of Solanki & Brigljevic (1992). The tick marks on these two curves specify $\tau_\lambda = 1$ locations for the line center of Mn I λ5395 (upward arrows), the line center of Fe I λ5395 (downward arrows), and the continuum in between (arrow-less). Extra $\tau_\lambda = 1$ ticks are added for the line synthesis when not applying turbulent smearing, but for the Mn I line this makes no difference. The two dotted additional models were defined by Unruh et al. (1999) as basis for solar irradiance modelling discussed in § 4.15. The lower one, close to the Maltby et al. (1986) model, is the quiet Sun, the upper one is the plage model.

over upward-expanding and canopy-merging magnetostatic fluxtubes as in Buente et al. (1993) but simply use it as on-axis representation of a fully-resolved fluxtube as in the cartoon in Figure 4.23, with constant field strength along the axis. The same was done in Figure 4.4. This fluxtube model is shown in Figure 4.23 together with the standard quiet Sun model of Maltby et al. (1986) which we use to represent the nonmagnetic atmosphere outside fluxtubes. Figure 4.23 shows two additional models from Unruh et al. (1999) that are discussed in § 4.15.

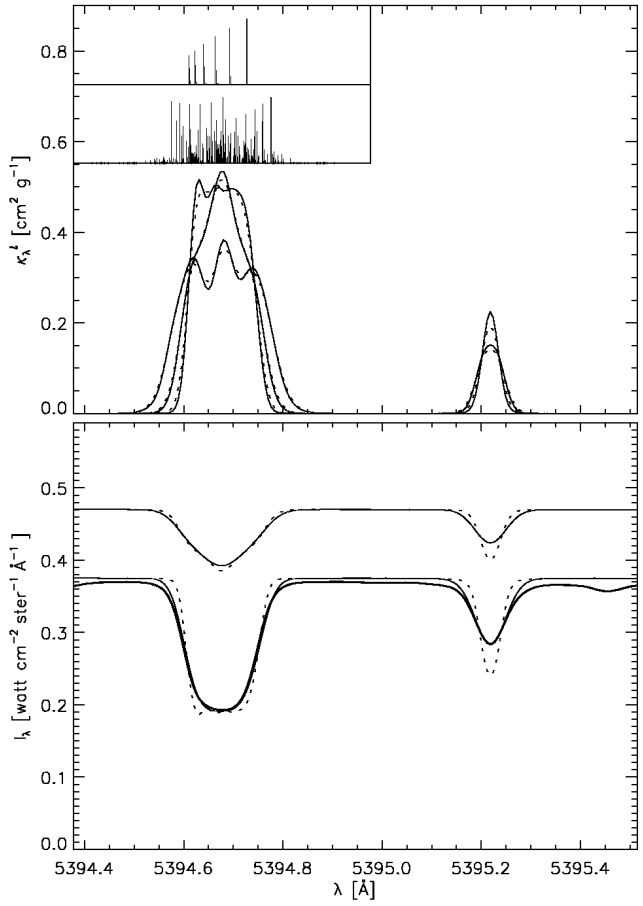

Figure 4.24: *Upper Panel*: line extinction coefficient for Mn I λ5395 (*left*) and Fe I λ5395 (*right*), for temperature $T = 5000$ K and longitudinal magnetic field strength $B = 0$ G (top solid curve), and 2000 G (lowest solid curve). For the Mn I λ5395 line there is also an intermediate profile for $B = 1000$ G. The dotted curves result when temperature $T = 7000$ K is inserted into the Dopplerwidth. The insets specify the splitting pattern of Mn I λ5395 for $B = 0$ G (*upper*) and $B = 2000$ G (*lower*). *Lower Panel*: line profiles resulting from classical 1D spectral synthesis. The lower solid curve in the lower trio is the quiet Sun disk-center spectrum in the atlas of Neckel (1999) which is an absolute-intensity version of the NSO/FTS atlas of Wallace et al. (1998). The other solid curve in the lower trio is the spectrum computed from the Maltby et al. (1986) model including micro- and macroturbulence. The dotted curve results when these fudge parameters are omitted. The two upper spectra result from the plage model with $B = 1000$ G, also with and without turbulent smearing.

4.13.2 3D Simulation

We use a single snapshot from a time-dependent simulation with the MURaM (MPS/University of Chicago Radiative MHD) code (Vögler & Schüssler 2003; Vögler 2004; Vögler et al. 2005). We give only a brief summary here. MURaM solves the three-dimensional time-dependent MHD equations including non-local and non-grey radiative transfer and accounting for partial ionization. The horizontal extent of the simulation used here is 6 Mm sampled in 288 grid points per axis, the vertical extent 1.4 Mm with 100 grid points. The particular snapshot used here is taken from a simulation as the one described by Vögler et al. (2005). It was started with a homogeneous vertical seed field of 200 G. Magnetoconvection gave it an appearance similar to active network with strong-field magnetic concentrations in intergranular lanes. A relatively quiet subcube was selected for line synthesis here. It has 2.5×2.5 Mm horizontal extent and contains a large granule and a field-free intergranular lane, in addition to lanes containing magnetic concentrations of varying field strength (Figure 4.25). The line synthesis performed for this paper used the code described above, treating the vertical columns in the subcube as independent lines of sight.

4.14 Results

Figure 4.24 presents results of our 1D modelling. The solid curves in the upper panel show the spectral variation of the extinction coefficient for both lines for temperature $T = 5000$ K and field strengths $B = 0$ G and $B = 2000$ G, plus the intermediate profile for $B = 1000$ G for the Mn I λ5395 line. For the Fe I λ5395 line the Zeeman effect produces simple broadening but for the Mn I λ5395 line the many hyperfine components, each with its own magnetic splitting, cause an intricate pattern shown in the lower part of the inset. The resulting profile widens in the wings but the core first becomes peaked at $B = 1000$ G and then splits into three collective peaks at $B = 2000$ G.

The dotted curves result from inserting temperature $T = 7000$ K into the Dopplerwidth but not into other variables, in order to show the effect of larger thermal broadening while keeping all other things equal. The Fe I λ5395 profile for $B = 0$ G looses appreciable amplitude while the Mn I λ5395 profile does not.

The lower panel of Figure 4.24 shows emergent intensity profiles for the two lines. The lowest solid curve is the observed spatially-averaged disk-center spectrum. It is closely matched by the Maltby quiet Sun when applying stan-

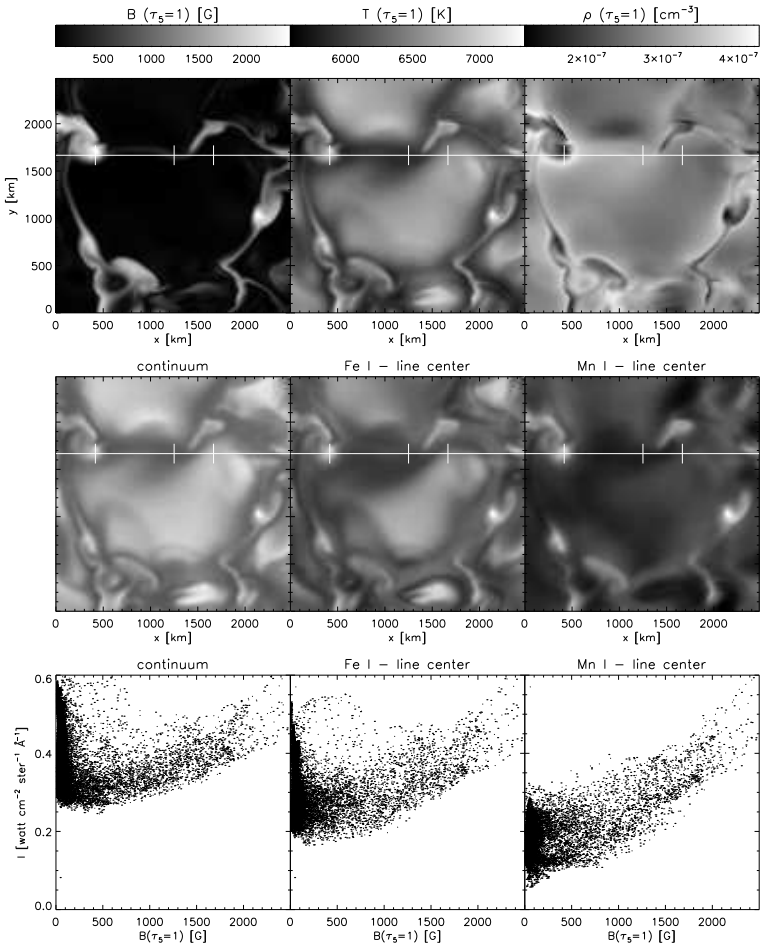

Figure 4.25: Results from the MURaM snapshot. *First row*: magnetic field strength, temperature, and gas density across the $\tau_5 = 1$ continuum-escape surface. Greyscale calibration bars are shown on top. The field is monopolar. The white line specifies the cut used in Figures 4.26–4.27 to display formation parameters in a vertical plane through the simulation volume. It represents a spectrograph slit in Figure 4.28. The three superimposed ticks specify locations analyzed in detail in Figure 4.28: a magnetic concentration, an intergranular lane, and the edge of the large granule in the center. *Second row*: synthetic intensity images for the continuum between the two lines and the nominal wavelengths of Fe I λ5395 and Mn I λ5395. They share the same intensity greyscale. These images represent predicted observations with a telescope matching the MURaM resolution by being diffraction-limited at 2.4-m aperture. *Third row*: the same intensities plotted as scatter diagrams per pixel against the magnetic field strength at the $\tau_5 = 1$ level for that pixel.

dard microturbulence (1 km s^{-1}) and best-fit macroturbulence (1.28 km s^{-1} for Mn I λ5395, 1.55 km s^{-1} for Fe I λ5395). When this artificial broadening is not applied the computed Fe I line becomes too deep, but the depth of the Mn I line does not change thanks to its flat-bottomed core. The upper curves result from the plage model with $B = 1000$ G, again with (solid) and without (dotted) turbulent smearing. The smearing again affects only the Fe I line. It causes a corresponding shift of the Fe I $\tau_\lambda = 1$ location along the quiet Sun in Figure 4.23.
Comparison of these quiet Sun and plage results shows that the spectrum brightens at all wavelengths but most in the Mn I line, by a factor 2. Turbulent smearing does not affect this line but it produces large difference for the Fe I line. In particular, if it is applied to the quiet Sun prediction but not to the plage profile, the Fe I line-center brightness increase is only a factor 1.4. This difference in line-center brightening suggests that the Fe I line suffers more from thermal broadening and the thermodynamic fine structuring that was traditionally modelled with micro- and macroturbulence. The apparent sensitivity of the Mn I line to magnetic activity may therefore indeed result from non-magnetic quiet Sun Doppler smearing of the Fe I line, lessening the latter's sensitivity.

The results from the MURaM simulation are shown in Figure 4.25. The three panels in the upper row show basic state parameters across the $\tau_5 = 1$ surface where τ_5 is the continuum optical depth at $\lambda = 5000$ Å determined separately for each simulation column. The middle row displays synthetic intensity images for our three diagnostics: the continuum between the two lines and the nominal line-center wavelengths of Fe I and Mn I lines. The bottom row shows these intensities in the form of pixel-by-pixel scatter plots against the magnetic field strength at $\tau_5 = 1$. The three images demonstrate directly why Mn I shows larger brightness contrast between non-magnetic and magnetic areas: the magnetic bright points reach similar brightness in all three panels but the granulation is markedly darker in this line. Darker granulation implies larger sensitivity to activity, i.e. addition of more magnetic bright points. The three scatter plots in the bottom row of Figure 4.25 quantify this behaviour. In the continuum plot at left the darkest pixels lie in field-free or weak-field intergranular lanes. Addition of magnetic field within the lanes brightens them, more for stronger fields, and for the strongest fields almost up to the maximum brightness of field-free granular centers. The scatter diagram for Fe I (bottom-center panel) shows a similar hook shape. The cloud of granulation pixels at left lies lower since the line is an absorption line. However, the pixels with the strongest field still brighten to the same values as in the continuum panel, implying that the line vanishes completely

at its nominal wavelength. The scatter diagram for Mn I line shows similar behaviour, but it loses the hook shape. The line is yet darker in field-free granulation. In this case the corresponding dark cloud of low-field pixels at left does not have an upward tail. However, the upward tail of pixels with increasing field still stretches all the way from the dark lanes to the continuum values, which again implies line vanishing. If magnetic field is added to field-free granulation, this addition takes away points from the bottom left of the distribution (corresponding to dark intergranular lanes) and adds "magnetic bright points" at the upper right. Its effect is more dramatic in the ensemble average of the Mn I line than in that of the Fe I line because the latter already has bright contributions from field-free granules; in the Fe I line the field-free granulation covers the same brightness range as the field-filled lanes. Thus, field addition means larger spatially-averaged brightness increase in the Mn I line than in the Fe I line.
We conclude that the MURaM synthesis duplicates the sun in having larger brightness response to more activity in the Mn I λ5395 line than in the Fe I λ5395 line through showing granulation darker.

4.14.1 Explanation

Unlike the sun, the MURaM simulation offers the opportunity to not only inspect the emergent spectrum but also to dissect the behaviour of pertinent physical parameters throughout the simulation volume. So, we add here an analysis of the MURaM results to diagnose why the granulation appears darker in the Mn I λ5395 line or rather, why it appears brighter in the Fe I λ5395 line.
The white line with three ticks in the grey-scale panels of Figure 4.25 specifies the spatial samples that are selected in Figures 4.26–4.27. This particular cut and the tick locations were chosen to sample a strong-field magnetic concentration that appears as a bright point in the intensity images (lefthand tick), a non-magnetic dark lane (middle tick), and a granule (righthand tick). Unfortunately, this cut samples only the edge rather than the center of the large granule covering the center part of the field but otherwise we wouldn't have sampled both a bright point and a non-magnetic lane. A magnetic lane less extreme than the bright point is sampled at the far right.
Figure 4.26 diagnoses MURaM physics in the vertical plane defined by this cut. It shows behaviour that is characteristic of solar magnetoconvection near the surface. The overlaid curves specify the $\tau_5 = 1$ continuum surface. The very low gas density (4th panel) in the magnetic concentration at $x \simeq 400$ km produces a large Wilson depression of about 200 km. The deep dip in the $\tau_5 = 1$ curve so samples relatively high temperature, as well

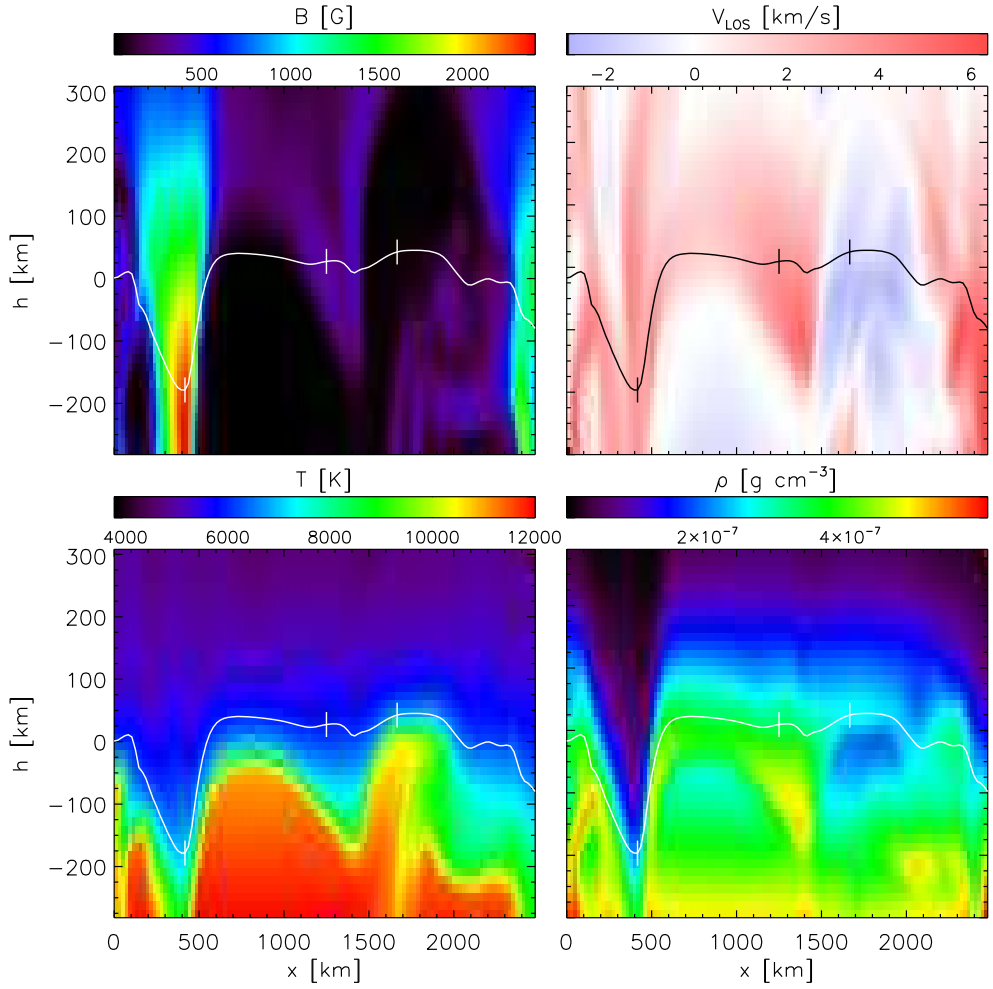

Figure 4.26: Various quantities in the MURaM snapshot across the vertical plane marked by the white horizontal line in Figure 4.25. The *upper panels* show the magnetic field strength and radial velocity as a function of geometrical height versus horizontal location along the cut. The height scale has $h = 0$ km at the mean $\tau_5 = 1$ level, averaged over all columns. It extends 882 km below and 518 km above that level in the simulation but only the pertinent height range is shown here. The velocity colouring is red for downdraft (redshift) and blue for updraft (blueshift). The *lower panels* show the temperature and the gas density. The overlaid curves specify $\tau_5 = 1$ continuum formation depths. The three ticks mark the locations analyzed in Figure 4.28.

as a relatively flat vertical temperature gradient. The intergranular lane at $x \simeq 1300$ km combines low temperature with high density and strong down-

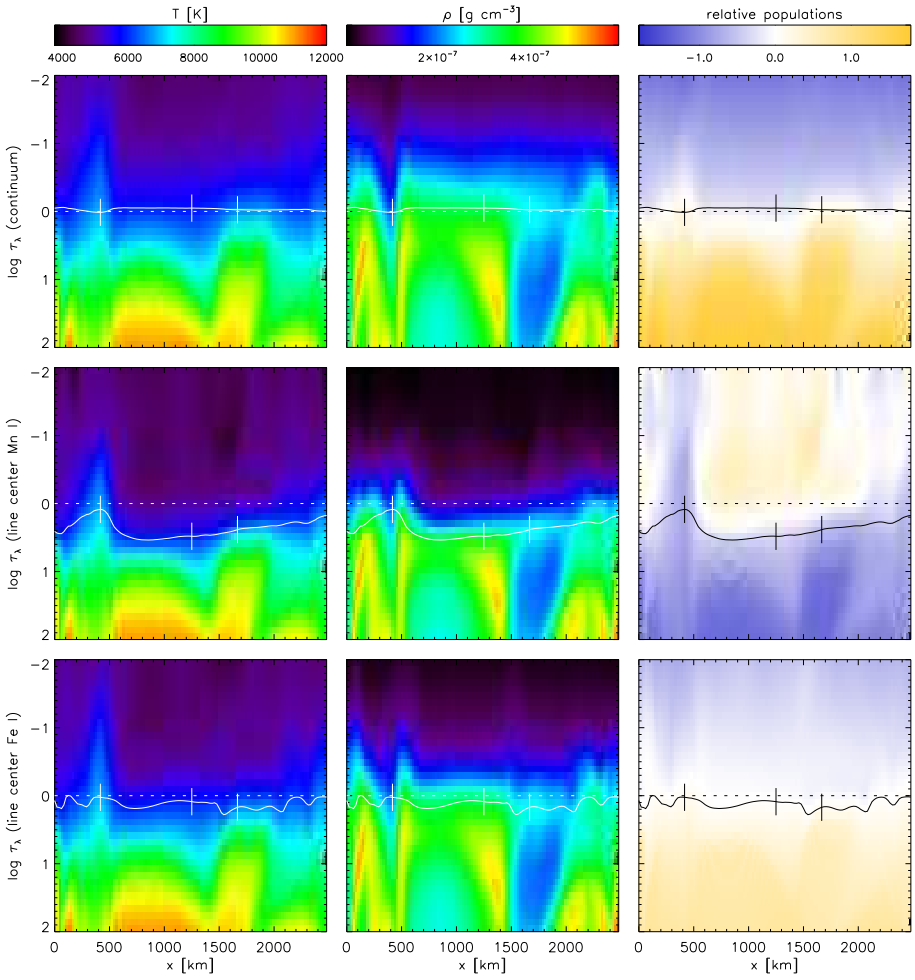

Figure 4.27: Temperature, gas density, and population variations across the vertical cut through the MURaM simulation plotted per column on radial optical depth scales for the nominal continuum (*top row*), Mn I λ5395 (*middle row*), and Fe I λ5395 (*bottom row*) wavelengths. The solid curves specify $\tau_5 = 1$ depths, the horizontal dotted lines feature-specific $\tau_\lambda = 1$ depths. The third column displays fractional population offsets. These are the lower-level populations for H^- bound-free transitions, the Mn I line, and the Fe I line, each normalized by the total element density (hydrogen, manganese, iron) per location and shown in logarithmic units scaled to the mean value at $\tau_\lambda = 1$ along the cut. Positive offsets are coloured amber, negative bluish. The scale runs from -1.8 to $+1.8$.

draft; the granule edge at $x \simeq 1650$ km combines higher temperature with gentler updraft and low subsurface density.

Figure 4.27 repeats this vertical-plane display of temperature and density

but plotted per column on the radial optical depth scale that belongs to each diagnostic. The panels in the first and second columns show the atmosphere "as seen" by each spectral feature at its nominal wavelength. The dotted horizontal lines at $\log \tau_\lambda = 0$ indicate their formation heights. The solid curves are the $\tau_5 = 1$ locations. The third column shows relative behaviour of the corresponding opacities in the form of fractional lower-level population variations.

The top panels of Figure 4.27 show only slight differences between the $\tau = 1$ locations along the cut. The magnetic concentration has an appreciable hump in $T(\tau_\lambda)$ and dip in $\rho(\tau_\lambda)$ around $\tau_5 = 1$. The relatively high temperature and low density there combine into increased electron-donor ionization. This is illustrated by the sixth panel showing the fractional population variation of the lower level of Mn I λ5395, which is the Mn I ground state. Its behaviour equals the depletion by manganese ionization apart from a minor correction for the temperature sensitivity of the Mn I partition function. Manganese has too small abundance to be an important electron donor, but it ionizes similarly to iron (Table 4.2) so that this panel illustrates characteristic electron-donor ionization, with neutral-stage depletion occurring within magnetic concentrations and at large depth. The corresponding increase of the free-electron density produces larger H^- opacity, evident as overall colour gradient reversal between the top and center panels in the third column. It results in an upward enhancement peak at the magnetic concentration in the H^- population panel. This relative increase of the continuum opacity explains that $\tau_\lambda = 1$ is reached at lower density in the magnetic concentration than in the adjacent intergranular lane (second panel); the Wilson depression is smaller than one would estimate from pressure balancing alone. The flat temperature gradient in the magnetic concentration produces a marked upward extension in $T(\tau_\lambda)$ in the first panel. It contributes brightness enhancement along much of the intensity contribution function and so makes magnetic concentrations appear bright with respect to non-magnetic lanes. However, the hook pattern in the continuum scatter plot in Figure 4.25 shows that this lane brightening does not exceed granular brightness.

The center row of Figure 4.27 shows that Mn I line is generally formed higher than the continuum, but not in the magnetic concentration where the upward hump in the $\tau_5 = 1$ curve nearly reaches the $\tau_\lambda = 1$ level. This is because the relatively high temperature and low density there increase the degree of manganese ionization, as evident in the third panel which shows a marked upward blue extension. The line weakens so much that the brightest Mn I pixels in Figure 4.25 reach the same intensity as in the continuum, also sampling the upward high-temperature extension (first column). Conversely, the largest line-to-continuous opacity ratio (i.e., the largest separation between

the $\tau_\lambda = 1$ and $\tau_5 = 1$ locations) is reached along the intergranular lane where the neutral-stage population is larger due to relatively large density and low temperature. Thus, the curve separation maps the variation of the fractional ionization along the dotted line. Since the temperature increases inward anywhere, the deeper sampling within the magnetic concentration and the higher sampling in the granulation, especially in the lanes, together increase the brightness contrast between bright point and granulation compared to that in the continuum. This effect of increased ionization is similar to the effect of CH dissociation in the G-band. It enhances the magnetic lane brightening so that that exceeds granular brightnesses, undoing the hook shape of the continuum scatter plot.

The bottom row of Figure 4.27 shows the corresponding plots for Fe I λ5395. Iron and manganese ionize similarly so that low-excitation Fe I lines suffer the same depletion in magnetic concentrations. However, Fe I is a high-excitation line; its Boltzmann sensitivity to higher temperature largely compensates for the enhanced ionization so that the panel in the third column looks much more like the top one for H^- than like the second one for Mn I λ5395: the overall colour gradient flips back again. The line again vanishes in the magnetic concentration, so that the strongest-field pixels in Figure 4.25 again reach the continuum intensities. One might expect that the curve separation in the bottom panels would follow the temperature pattern under the dotted line in the first column, but this is not the case; for example, the line also nearly vanishes (at its nominal wavelength) in the intergranular lane. This discordant variation is caused by the Dopplershifts imposed on the line extinction by the flows displayed in the upper-right panel of Figure 4.26. Comparison shows that the unsigned amplitude of the flow variation along the cut at $100 - 200$ km above the $\tau_5 = 1$ curve there is mapped precisely into reversed modulation of the $\tau_5 = 1$ curve for Fe I λ5395 here. Thus, the line vanishes because it is shifted aside from its nominal wavelength.

We demonstrate the Doppler-related formation differences between the two lines further in Figure 4.28. The upper two panels display spectral representations along the cut defined in Figure 4.25, in the form of a spectral image and of profile samples. The top panel shows what would have appeared in an observational spectrogram from a telescope with MURaM resolution. Both lines show a bright "line gap" in the magnetic concentration near the bottom. At $x \simeq 2500$ km the intergranular lane with less strong field still causes a noticeable gap. Large Dopplershifts occur in the field-free lane and the granular edge.

The second panel shows the product of data reduction of this spectrogram. Both panels illustrate that the line-center intensity of the Mn I λ5395 line is not very sensitive to Dopplershifts, whereas the Fe I λ5395 line shifts well

away from its nominal wavelength nearly everywhere. It also weakens more in the granule edge from larger thermal broadening (Figure 4.24). Taking the spatial mean at each nominal wavelength does a fair job of intensity averaging for the Mn I line but misses nearly all dark cores in the Fe I line, especially in the lanes but also in granules. Note that this particular cut does not represent hot granules well; more samples of these would add many profiles with weakened cores blueward of the nominal Fe I λ5395 wavelength. The third panel shows the spectral profiles for the three sample locations along the cut. The nominal Fe I λ5395 line-center wavelength misses all three cores! Thus, the brightness average at this wavelength is much higher than it would be for an undisturbed line of this opacity. The Mn I λ5395 line-center wavelength, however, only misses the deepest part of the magnetic-concentration profile which is weak anyhow. This disparity in Doppler sensitivity explains why the granulation in Figure 4.25 is much darker in Mn I than in Fe I.

Also note the sharpening of the Mn I λ5395 line profile from boxy to more pointed in some of the intermediate profiles in the second panel, which follows the extinction coefficient behaviour in Figure 4.24. It contributes to the decrease in equivalent width of Mn I at larger activity, which is not analyzed here.

The bottom panels of Figure 4.28 show the vertical temperature stratifications at the three sample locations, at left against geometrical height with $h = 0$ at $\tau_5 = 1$ for the simulation mean, at right against column mass per feature. These graphs link the simulation results back to the classical fluxtube modelling in § 4.13.1. They display familiar properties of granulation and magnetic concentrations: the temperature gradient is steepest in granules, flatter in intergranular lanes, with a mid-photosphere cross-over producing "reversed granulation", and flattest in fluxtubes. The heights of formation, marked by ticks specifying the $\tau_\lambda = 1$ locations, are similar per line in the granular edge and the lane but much deeper in the magnetic concentration which is the coolest feature at equal geometrical height but the hottest at equal column mass and at the $\tau_{\rm cont} = 1$ location per feature. The Wilson depression is about 200 km in the continuum and twice as large for the Mn I line through enhanced ionization within the magnetic concentration, but not for the Fe I line due to its Doppler-deepened granulation sampling. Both lines weaken severely in the magnetic concentration through this deep sampling, and both are redshifted away from their nominal wavelength, Fe I λ5395 all the way so that its $\tau_\lambda = 1$ tick coincides with the continuum one.

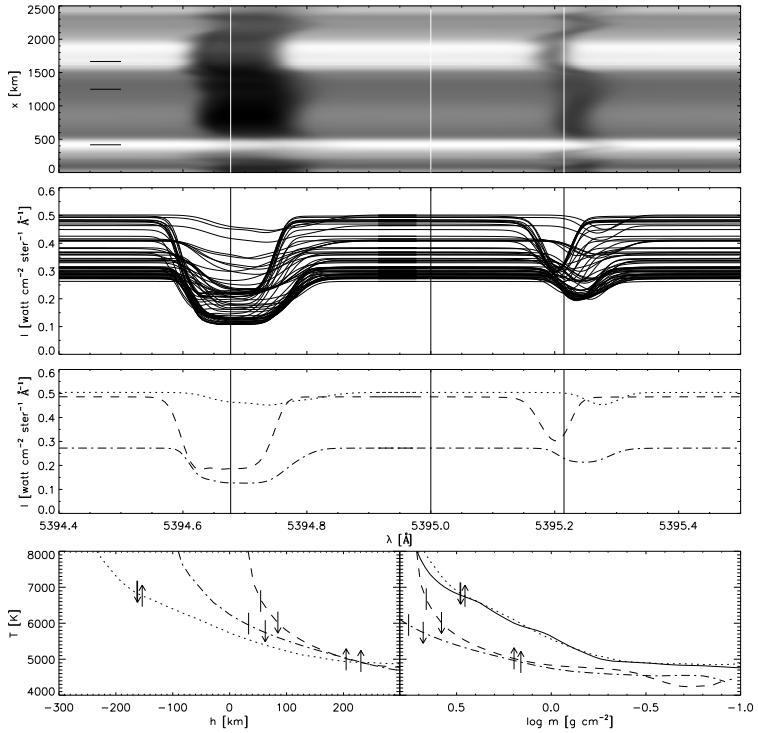

Figure 4.28: Further analysis of the formation of Mn I λ5395, Fe I λ5395, and the intermediate continuum in the MURaM simulation. *Top panel*: spectrum synthesized from the computed emergent intensities. The vertical coordinate corresponds to the x sampling along the cut specified in Figure 4.25. The three black horizontal markers correspond to the ticks selecting the bright point (lowest), field-free intergranular lane (middle), and granule edge (highest). The three vertical lines specify the nominal wavelengths for Mn I line (left), Fe I line (right), and the intermediate continuum (center). *Second panel*: spectral profiles for every second pixel along the cut. *Third panel*: spectral profiles for the three locations specified by ticks in Figure 4.25 and black markers in the top panel. *Dotted*: magnetic concentration. *Dot-dashed*: intergranular lane. *Dashed*: granule edge. *Bottom panels*: temperature stratifications for the three selected locations, at left against geometrical height, at right against column mass as in Figure 4.23. The solid curve is the plage model, as in Figure 4.23. The tick marks specify the $\tau_\lambda = 1$ locations for the nominal wavelengths of Mn I λ5395 (upward arrows), of Fe I λ5395 (downward arrows), and of the continuum in between (arrowless). In the magnetic concentration the Fe I λ5395 tick coincides nearly with the continuum one. The Wilson depression is much larger for the Mn I line than for the continuum and the Fe I line.

4.15 Discussion

We have used both classical empirical fluxtube modelling (§ 4.13.1) and modern MHD simulation (§ 4.13.2). The bottom panels of Figure 4.28 connect the latter with the former. The righthand panel shows remarkably close agreement between the plage model and the MURaM magnetic-concentration stratification. This may be taken as mutual vindication of these very different techniques, but not as proof of correctness since both assumed LTE ionization while the sun does not.
The simulation resolves the granular Dopplershifts that were emulated by turbulence in the classical modelling. The simulation analysis in § 4.14.1 confirms that Mn I λ5395 activity-brightens more than Fe I λ5395 because its intrinsic hyperfine-structure broadening suppresses thermal and Doppler brightening in non-magnetic granulation. This was already indicated by the 1D demonstration in Figure 4.24.

In our approach we have not made the step from radial viewing to full-disk averaging. The demonstration in § 4.13.1 used Solanki's one-dimensional empirical model for a fluxtube in plage but without adding flaring fluxtube geometry, granular presence next to a fluxtube and behind it in slanted facular viewing, multiple-tube interface geometry, spatial averaging over these geometries, the multi-angle evaluation needed to emulate center-to-limb viewing, and without full-disk averaging and consideration of spatial distributions over the solar surface and their variations with the solar cycle. All these non-trivial aspects would need careful quantification to the demonstration of enhanced sensitivity in § 4.13.1 into a quantitative estimate for comparison with Livingston's irradiance data. The simulations in § 4.13.2 yielded profile synthesis for a small area of solar surface containing strong-field concentrations that may be considered more realistic than idealized magnetostatic fluxtubes but, nevertheless, generation of full-disk signals comparable to Livingston's data still requires all the above quantifications. This effort is not done here. In contrast, the step from one-dimensional line synthesis to emulation of the full-disk and cycle-dependent integrated signal was recently made by Danilović et al. (2007) using the SATIRE (Spectral And Total Irradiance Reconstruction) approach of Fligge et al. (2000), Krivova et al. (2003) and Wenzler et al. (2005, 2006). In this technique the spatial distributions of spots and plage are extracted from full-disk magnetograms and continuum images to derive disk-coverage distributions throughout the more recent activity cycles. Each component (quiet Sun, plage, spots) is represented by a standard one-dimensional model atmosphere. The first two are shown as dotted curves in Figure 4.23. The lower one for quiet Sun is the radiative equilibrium model

of Kurucz (1979, 1992a,b) which is nearly identical to the Maltby quiet Sun. The upper one for plage was made by Unruh et al. (1999) by smoothing model P of Fontenla et al. (1993) and deleting its chromospheric temperature rise. For spots a Kurucz radiative-equilibrium model with low effective temperature is used, but not shown here. Danilović et al. (2007) found that using these models with the empirically established SATIRE coverage fractions gives a good reproduction of Livingston's data both for Mn I λ5395 and Fe I λ5395. Such use of the dotted models in Figure 4.23 is an ad-hoc trick to reproduce the larger brightness of plage. The Mn I line activity-brightens more than Fe I one in this simplistic modelling because it is a stronger line, hence formed higher, hence getting more out of the divergence between the two models with height. Any line as strong would show the same brightening. Stronger lines would brighten more; in particular, Fe I lines with deeper cores than Mn I λ5393 would show larger activity modulation in conflict with the observations. Actually, as illustrated in Figure 4.22 and demonstrated in Figures 4.25–4.27, plage thanks its disk-center brightening in any photospheric diagnostic not to being hotter at equal height but to below-the-surface viewing of hot-wall heat within magnetic concentrations. The SATIRE modelling does not evaluate Wilson depressions, but as long as the SATIRE models are used in one-dimensional radial fashion on their own column mass or optical depth scale this does not matter. In this sense the Unruh plage model does recognize that the local temperature gradient around local $\tau = 1$ within magnetic concentrations tends to be less steep than in the granulation, as in the bottom panels of Figure 4.28. However, the approximation breaks down for non-vertical fluxtube viewing for which the "Zürich wine-glass" geometry of Buente et al. (1993) with slanted rays passing through the glasses was a much more realistic description, and it fails for limbward faculae because slanted viewing of hot granule innards through empty fluxtubes (Figure 4.22) should not be described by the vertical temperature stratification within magnetic concentrations.

Plage and faculae were much better treated by the older Solanki-style fluxtube models which diverge with depth instead of with height between magnetic and non-magnetic (compare the plage and Unruh plage models in Figure 4.23 and plage with the MURaM stratification in Figure 4.28). Obviously, outward divergence supplies a zero-order approximation to increasing facular contrast in limbward viewing, but no more than that and inherently wrong. The same criticisms apply to the similar photospheric feature modelling through outward-diverging temperature stratifications by Fontenla et al. (1993, 2006) who add more ad-hoc adjustment parameters in the form of a deep-seated chromospheric temperature rise, comparable to the ones invoked by Doyle et al. (2001), that was rightfully removed by Unruh et al. (1999)

in their plage model – the chromosphere has nothing to do with network and plage visibility in photospheric diagnostics. Nevertheless, the success of the SATIRE modelling by Danilović et al. (2007) implies that, given any trick to make a single magnetic concentration brighter in Mn I λ5395 than in Fe I λ5395 by the amount given by SATIRE's two-model divergence, that trick will reproduce Livingston's data similarly. Thus, although we have not performed any full-disk modelling, our trick is likely to reproduce these data too. Our trick entails better understanding of why Mn I lines activity-brighten more than other lines: the latter brighten more in normal granulation.

Chapter 5

Thesis Conclusions

Three different approaches are adopted in this PhD thesis to analyze the properties of quiet Sun magnetic fields and to improve the techniques used to measure them: description, through dynamical models, of the temporal evolution of magnetic fields, development of a new synthesis code for the study of the properties conferred to Mn I lines by photospheric magnetic fields and the inversion of standard visible Fe I lines observed by the HINODE satellite.
In the following four sections we expose the main conclusions drawn from our work.

5.1 Conclusions on the Dynamical Model

The dynamical model described in § 2.1 and § 2.2 mimicks the dynamics and evolution of photospheric magnetic elements passively driven by an horizontal velocity field which presents spatio-temporal correlations in agreement with those observed in the solar photosphere. The description of the velocity field follows Rast (1998, 2003). In their evolution, the magnetic elements interact and increase their magnetic field strengths through an amplification process assumed to work on a time scale comparable with the granular timescale and able to create kG concentrations. The imposed injection scale at $B_{in} = 30$ G and the upper limit at $B_{lim} = 2$ kG are both derived from observations (e.g., Carroll & Kopf 2008) and physical constraints (e.g., Parker 1978).
We investigated the statistical properties of the field strengths associated with the magnetic elements using a series of numerical simulations. The main conclusions are:

1. The model produces kG fields in a time interval of the order of the meso-granulation time scale. Such strong fields are organized in a pattern

superposed onto the mesogranulation pattern of the advection field.

2. In the stationary regime, the probability density function (PDF) of the magnetic field strength presents an exponential decay from the absolute maximum at $B_{in} = 30$ G to about 1 kG and an evident secondary maximum at the upper limit set at 2 kG.

3. The associated mean unsigned flux density and mean magnetic energy density, calculated as the first and the second momentum of the PDF, are $\langle B \rangle \simeq 100$ G and $\langle B^2 \rangle^{1/2} \simeq 350$ G, respectively.

4. The magnetic element system described by such a PDF is strongly dominated by kG magnetic fields; in fact, the fractions of unsigned flux density and magnetic energy density for $B \geq 700$ G are $\simeq 65\%$ and $\simeq 97\%$, respectively.

The quiet Sun is certainly more complex than the model presented here. However, a reduced approach, based on the advection field proposed by Rast (2003), reproduced the observed distributions for the released magnetic energy and waiting times of nanoflare events (Viticchié et al. 2006). In this PhD thesis, we showed how the same approach can also be exploited to successfully reproduce some of the statistical properties of the quiet Sun magnetic fields. As already pointed out in Viticchié et al. (2006), the role of the spatio-temporal correlations of the adopted velocity field, here combined with the upper limit for the magnetic field strength at B_{lim}, are essential in defining the statistical properties of the quiet Sun magnetic fields in the kG range. The conclusions outlined in this section are published in Berrilli et al. (2008).

5.2 Conclusions on the Synthesis

The Zeeman pattern of the Mn I lines depends on hyperfine structure (HFS), which confers them a sensitivity to hG magnetic field strengths different from the lines traditionally used in solar magnetometry. This peculiarity has been used to measure magnetic field strengths in quiet Sun regions (see § 1.2.1). In this PhD thesis we describe three complementary LTE synthesis codes (from § 4.1 to § 4.5; Milne-Eddington, one-dimensional, and MIcro Structured Magnetized Atmosphere) that have been written to study in detail the properties of lines presenting HFS (with particular attention to Mn I λ5538). These provide a number of relevant results:

1. They reproduce the observed Mn I patterns of spectral line profiles of nine assorted lines showing different HFS sensitivities (§ 4.5).

2. The study focused the Mn I λ5538 line shows how the scaling on the magnetic field strength proposed by the Weak Field Approximation breaks down when $B \geq 400$ G. When the expected coupling between the thermodynamic conditions and the magnetic field strengths is taken into account, a dimming of the kG Stokes V signals is found; this can be as large as two orders of magnitude (see Figures 4.3 and 4.7). This has significant observational implications for all Mn I lines.

3. If the resolution elements contains both weak and strong fields, then the kG fields tend to be under-represented in the average profile. We have modelled the bias assuming a multi component atmosphere, where the synthetic signals are weighted means of the Stokes profiles corresponding to each field strength. According to our modelling, even when the magnetic flux and the magnetic energy are dominated by kG magnetic fields, the Stokes V profile of Mn I λ5538 can show HFS reversal feature at line core characteristic of hG fields (Figure 4.6).

4. A pure morphological inspection of the Stokes profiles does not suffice to infer which is the dominant magnetic field strength in the resolution element. For the HFS hump of Mn I λ5538 to disappear the kG filling factor has to be larger than the sub-kG filling factor. Consequently, when the HFS hump disappears the magnetic flux and magnetic energy of the atmosphere are completely dominated by kG fields (§ 4.3.1). Detecting Stokes V profiles with HFS features indicates the presence of hG fields in the resolution element. However, this sole observation does not reveal whether the hG field strengths dominate.

There seem to be two extreme alternatives to exploit the diagnostic potential of Mn I lines. First, improving the spatial resolution of the observations to a point where the quiet Sun magnetic structures can be regarded as spatially resolved. Unfortunately, this possibility is not feasible at present. On the other hand we can develop inversion techniques where complex magnetic atmospheres are included into the diagnostics. Using appropriate constraints, the number of free parameters required to describe such atmospheres can be maintained within reasonable limits (e.g., the MISMA models in Sánchez Almeida 1997). Dealing with unresolved velocities also favors detailed inversion codes (§ 4.4).
The conclusions outlined in this section are published in Sánchez Almeida et al. (2008).

5.3 Conclusions on the Inversion

In § 4.6 – § 4.9 we illustrated the preliminary results of the inversion of Stokes I and V profiles, observed with the HINODE satellite. The inversion was performed under the MISMA hypothesis (Sánchez Almeida et al. 1996) that provides the degree of realism required to invert the complex polarization profiles emerging in quiet Sun regions.
The simple inversion strategy illustrated in § 4.8 worked for the inversion of a sample of about 15000 profile allowing us to obtain the following preliminary conclusions:

1. The statistical description of quiet Sun via magnetic field PDF reveal a quiet Sun dominated by strong kG fields. This result is in contrast with recent statistical description obtained from full Stokes Milne-Eddington inversion proposed by Orozco Suárez et al. (2007). This disagreement can be ascribed to the partial inversion we performed of HINODE SOT/SP data. For this reason we are planing to perform a new inversion analysis to take into account Stokes Q and U data.

2. The MISMA scenarios emerging from network and quiet Sun regions are the following: network patches are almost totally composed of fields above 10^3 G while quiet in quiet Sun regions hG and kG fields coexist. It is worth noting that the description based on MISMA models can give us much more information than the sole magnetic field strength we took into account at the present stage, e.g., velocity along the line of sight, filling factors of the magnetic fields, orientation of the magnetic field vector. In this framework the results here presented can be considered as a starting point for a complete work on the MISMA interpretation of full Stokes HINODE SOT/SP data.

5.4 Conclusions on the Activity Modulation

From § 4.10 to § 4.15 we analyzed the magnetic sensitivity of Mn I λ5395. From the work done we can outline the following conclusions:

1. The explanation of the activity sensitivity of Mn I λ5395 concerns deep photosphere line formation only. Intergranular magnetic concentrations are brighter than field-free intergranular lanes because of the high and flat-gradient temperatures sampled by the emerging radiation (Figure 4.26 and Figure 4.27). For normal, narrow photospheric lines this brightening has less effect in full-disk averaging through their

loss of line depth in normal granulation (Figure 4.28) that was traditionally mimicked by applying micro- and macroturbulent smearing (Figure 4.24). The flat-bottomed profile which Mn I λ5395 possesses thanks to its hyperfine structure (Figure 4.24) makes this line much less susceptible to granular Doppler smearing and thermal broadening. As a consequence, Mn I λ5395 line weakens less in normal granulation (Figure 4.28) and displays larger brightness contrast between quiet and magnetic areas (Figure 4.25).

2. From above follows that Mn I λ5395 line is a proxy for magnetic fields sensitive to the magnetic concentrations that constitute on-disk network and plage and near-limb faculae. As a proxy magnetometer, Mn I λ5395 is similar to the G-band in which the contrast enhancement arises from the general addition of CH line opacity and local reduction of that through dissociation in magnetic concentrations. However, the G-band is the most useful of these two proxies by being a wide-band spectral feature.

We conclude that the principal usefulness of photospheric Mn I lines lies not in their unusual activity sensitivity but in their hyperfine-structured richness as weak-field diagnostic in full-Stokes polarimetry with high angular resolution and sensitivity as exposed in § 4.1 to § 4.5.
The conclusions outlined in this section are published in Vitas et al. (2008).

References

Abt, A. 1952, ApJ, 115, 199

Asensio Ramos, A., Martínez González, M. J., López Ariste, A., Trujillo Bueno, J., & Collados, M. 2007, ApJ, 659, 829

Auffret, H. & Muller, R. 1991, A&A, 246, 264

Bellot Rubio, L. R., Ruiz Cobo, B., & Collados, M. 1997, ApJL, 478, L45+

Bercik, D. J. 2002, PhD thesis, AA(MICHIGAN STATE UNIVERSITY)

Berger, T. E., Schrijver, C. J., Shine, R. A., et al. 1995, ApJ, 454, 531

Berger, T. E. & Title, A. M. 1996, ApJ, 463, 365

Berrilli, F., Consolini, G., Pietropaolo, E., et al. 2002, A&A, 381, 253

Berrilli, F., Del Moro, D., Russo, S., Consolini, G., & Straus, T. 2005, ApJ, 632, 677

Berrilli, F., Del Moro, D., & Viticchiè, B. 2008, ArXiv e-prints, 807

Bianda, M., Stenflo, J. O., & Solanki, S. K. 1999, A&A, 350, 1060

Blackwell-Whitehead, R. J., Pickering, J. C., Pearse, O., & Nave, G. 2005, ApJS, 157, 402

Boffetta, G., Carbone, V., Giuliani, P., Veltri, P., & Vulpiani, A. 1999, Physical Review Letters, 83, 4662

Bohr, T., Jensen, M. H., Paladin, G., & Vulpiani, A. 1998, Dynamical Systems Approach to Turbulence (Dynamical Systems Approach to Turbulence, by Tomas Bohr and Mogens H. Jensen and Giovanni Paladin and Angelo Vulpiani, pp. 370. ISBN 0521475147. Cambridge, UK: Cambridge University Press, August 1998.)

Bommier, V., Derouich, M., Landi degl'Innocenti, E., Molodij, G., & Sahal-Bréchot, S. 2005, A&A, 432, 295

Bransden, B. H. & Joachain, C. J. 1983, Physics of Atoms and Mulecules (Prentice Hall, Pearson Education)

Buchlin, E., Galtier, S., & Velli, M. 2005, A&A, 436, 355

Buente, M., Solanki, S. K., & Steiner, O. 1993, A&A, 268, 736

Carlsson, M., Stein, R. F., Nordlund, Å., & Scharmer, G. B. 2004, ApJL, 610, L137

Carroll, T. A. & Kopf, M. 2008, A&A, 481, L37

Cattaneo, F. 1999, ApJL, 515, L39

Cattaneo, F., Emonet, T., & Weiss, N. 2003, ApJ, 588, 1183

Collados, M. 2001, in Astronomical Society of the Pacific Conference Series, Vol. 236, Advanced Solar Polarimetry – Theory, Observation, and Instrumentation, ed. M. Sigwarth, 255–+

Cowling, T. G. 1933, MNRAS, 94, 39

Danilović, S., Solanki, S. K., Livingston, W., Krivova, N., & Vince, I. 2007, in Modern solar facilities - advanced solar science, ed. F. Kneer, K. G. Puschmann, & A. D. Wittmann, 189–+

Danilovic, S., Vince, I., Vitas, N., & Jovanovic, P. 2005, Serbian Astronomical Journal, 170, 79

de Wijn, A. G., Rutten, R. J., Haverkamp, E. M. W. P., & Sütterlin, P. 2005, A&A, 441, 1183

Del Moro, D. 2004, A&A, 428, 1007

Del Moro, D., Giordano, S., & Berrilli, F. 2007, A&A, 472, 599

Domínguez Cerdeña, I. 2003, A&A, 412, L65

Domínguez Cerdeña, I., Kneer, F., & Sánchez Almeida, J. 2003a, ApJL, 582, L55

Domínguez Cerdeña, I., Sánchez Almeida, J., & Kneer, F. 2003b, A&A, 407, 741

Domínguez Cerdeña, I., Sánchez Almeida, J., & Kneer, F. 2006, ApJ, 636, 496

Doyle, J. G., Jevremović, D., Short, C. I., et al. 2001, A&A, 369, L13

Dunn, R. B. & Zirker, J. B. 1973, Sol. Phys., 33, 281

Elste, G. 1987, Sol. Phys., 107, 47

Elste, G. & Teske, R. G. 1978, Sol. Phys., 59, 275

Emonet, T. & Cattaneo, F. 2001a, in Astronomical Society of the Pacific Conference Series, Vol. 236, Advanced Solar Polarimetry – Theory, Observation, and Instrumentation, ed. M. Sigwarth, 355–+

Emonet, T. & Cattaneo, F. 2001b, ApJL, 560, L197

Faurobert-Scholl, M. 1993, A&A, 268, 765

Faurobert-Scholl, M., Feautrier, N., Machefert, F., Petrovay, K., & Spielfiedel, A. 1995, A&A, 298, 289

Fisher, R. A. & Peck, E. R. 1939, Phys. Rev., 55, 270

Fligge, M., Solanki, S. K., & Unruh, Y. C. 2000, A&A, 353, 380

Fontenla, J. M., Avrett, E., Thuillier, G., & Harder, J. 2006, ApJ, 639, 441

Fontenla, J. M., Avrett, E. H., & Loeser, R. 1993, ApJ, 406, 319

Fragos, T., Rantsiou, E., & Vlahos, L. 2004, A&A, 420, 719

Frutiger, C. & Solanki, S. K. 1998, A&A, 336, L65

Grossmann-Doerth, U., Schuessler, M., & Steiner, O. 1998, A&A, 337, 928

Gurtovenko, E. A. & Kostyk, R. I. 1989, Fraungoferov spektr i sistema solnechnykh sil ostsilliatorov (Kiev : Nauk. dumka, 1989.)

Harvey-Angle, K. L. 1993, PhD thesis, , Utrecht University, The Netherlands, (1993)

Hudson, H. S. 1991, Solar Phys., 133, 357

Ichimoto, K., Lites, B., Elmore, D., et al. 2008, Sol. Phys., 249, 233

Keller, C. U., Schüssler, M., Vögler, A., & Zakharov, V. 2004, ApJL, 607, L59

Khomenko, E. V., Collados, M., Solanki, S. K., Lagg, A., & Trujillo Bueno, J. 2003, A&A, 408, 1115

Khomenko, E. V., Shelyag, S., Solanki, S. K., & Vögler, A. 2005, A&A, 442, 1059

Kosugi, T., Matsuzaki, K., Sakao, T., et al. 2007, Sol. Phys., 243, 3

Krivova, N. A., Solanki, S. K., Fligge, M., & Unruh, Y. C. 2003, A&A, 399, L1

Krucker, S. & Benz, A. O. 1998, ApJL, 501, L213+

Kurucz, R. L. 1979, ApJS, 40, 1

Kurucz, R. L. 1992a, Revista Mexicana de Astronomia y Astrofisica, vol. 23, 23, 181

Kurucz, R. L. 1992b, Revista Mexicana de Astronomia y Astrofisica, vol. 23, 23, 187

Landi degl'Innocenti, E. 1975, A&A, 45, 269

Landi degl'Innocenti, E. 1978, A&AS, 33, 157

Landi degl'Innocenti, E. 1998, Nature, 392, 256

Landi degl'Innocenti, E. 2007, Fisica Solare (Springer)

Larmor, J. 1919, Brit. Ass. Rep., 159

Lefèbvre, P.-H., Garnir, H.-P., & Biémont, E. 2003, A&A, 404, 1153

Lin, H. 1995, ApJ, 446, 421

Lin, H. & Rimmele, T. 1999, ApJ, 514, 448

Lites, B. W. 2002, ApJ, 573, 431

Lites, B. W., Elmore, D. F., & Streander, K. V. 2001, in Astronomical Society of the Pacific Conference Series, Vol. 236, Advanced Solar Polarimetry – Theory, Observation, and Instrumentation, ed. M. Sigwarth, 33–+

Lites, B. W., Kubo, M., Socas-Navarro, H., et al. 2008, ApJ, 672, 1237

Livingston, W. & Wallace, L. 1987, ApJ, 314, 808

Livingston, W., Wallace, L., White, O. R., & Giampapa, M. S. 2007, ApJ, 657, 1137

Livingston, W. C. & Harvey, J. 1975, in Bulletin of the American Astronomical Society, Vol. 7, Bulletin of the American Astronomical Society, 346–+

Loefdahl, M. G., Berger, T. E., Shine, R. S., & Title, A. M. 1998, ApJ, 495, 965

López Ariste, A., Martínez González, M. J., & Ramírez Vélez, J. C. 2007, A&A, 464, 351

López Ariste, A., Tomczyk, S., & Casini, R. 2002, ApJ, 580, 519

López Ariste, A., Tomczyk, S., & Casini, R. 2006, A&A, 454, 663

Malanushenko, O., Jones, H. P., & Livingston, W. 2004, in IAU Symposium, Vol. 223, Multi-Wavelength Investigations of Solar Activity, ed. A. V. Stepanov, E. E. Benevolenskaya, & A. G. Kosovichev, 645–646

Maltby, P., Avrett, E. H., Carlsson, M., et al. 1986, ApJ, 306, 284

Manso Sainz, R., Landi Degl'Innocenti, E., & Trujillo Bueno, J. 2004, ApJL, 614, L89

Margrave, Jr., T. E. 1972, Sol. Phys., 27, 294

Martínez González, M. J., Collados, M., & Ruiz Cobo, B. 2006a, in Astronomical Society of the Pacific Conference Series, Vol. 358, Astronomical Society of the Pacific Conference Series, ed. R. Casini & B. W. Lites, 36–+

Martínez González, M. J., Collados, M., & Ruiz Cobo, B. 2006b, A&A, 456, 1159

Martínez González, M. J., Collados, M., Ruiz Cobo, B., & Beck, C. 2008, A&A, 477, 953

Muller, R., Hulot, J. C., & Roudier, T. 1989, Sol. Phys., 119, 229

Muller, R., Roudier, T., Vigneau, J., & Auffret, H. 1994, A&A, 283, 232

Neckel, H. 1999, Sol. Phys., 184, 421

Nordlund, A. 1983, in IAU Symposium, Vol. 102, Solar and Stellar Magnetic Fields: Origins and Coronal Effects, ed. J. O. Stenflo, 79–83

Nordlund, Å. & Stein, R. F. 1990, in IAU Symposium, Vol. 138, Solar Photosphere: Structure, Convection, and Magnetic Fields, ed. J. O. Stenflo, 191–+

Ogawara, Y., Takano, T., Kato, T., et al. 1991, Sol. Phys., 136, 1

Orozco Suárez, D., Bellot Rubio, L. R., del Toro Iniesta, J. C., et al. 2007, ApJL, 670, L61

Parker, E. N. 1955, ApJ, 122, 293

Parker, E. N. 1978, ApJ, 221, 368

Parker, E. N. 1988, ApJ, 330, 474

Parnell, C. E. & Jupp, P. E. 2000, ApJ, 529, 554

Ramirez Velez, J. C., Lopez Ariste, A., & Semel, M. 2008, ArXiv e-prints, 806

Rast, M. P. 1998, Journal of Fluid Mechanics, 369, 125

Rast, M. P. 2003, ApJ, 597, 1200

Rees, D. E., López Ariste, A., Thatcher, J., & Semel, M. 2000, A&A, 355, 759

Roudier, T., Malherbe, J. M., Vigneau, J., & Pfeiffer, B. 1998, A&A, 330, 1136

Rutten, R. J. 1999, in Astronomical Society of the Pacific Conference Series, Vol. 184, Third Advances in Solar Physics Euroconference: Magnetic Fields and Oscillations, ed. B. Schmieder, A. Hofmann, & J. Staude, 181–200

Rutten, R. J., Kiselman, D., Rouppe van der Voort, L., & Plez, B. 2001, in Astronomical Society of the Pacific Conference Series, Vol. 236, Advanced Solar Polarimetry – Theory, Observation, and Instrumentation, ed. M. Sigwarth, 445–+

Sanchez Almeida, J. 1992, Sol. Phys., 137, 1

Sánchez Almeida, J. 1997, ApJ, 491, 993

Sánchez Almeida, J. 1998, in Astronomical Society of the Pacific Conference Series, Vol. 155, Three-Dimensional Structure of Solar Active Regions, ed. C. E. Alissandrakis & B. Schmieder, 54–+

Sánchez Almeida, J. 2001, ApJ, 556, 928

Sánchez Almeida, J. 2004, in Astronomical Society of the Pacific Conference Series, Vol. 325, The Solar-B Mission and the Forefront of Solar Physics, ed. T. Sakurai & T. Sekii, 115–+

Sánchez Almeida, J. 2007, ApJ, 657, 1150

Sánchez Almeida, J., Domínguez Cerdeña, I., & Kneer, F. 2003a, ApJL, 597, L177

Sánchez Almeida, J., Emonet, T., & Cattaneo, F. 2003b, ApJ, 585, 536

Sánchez Almeida, J., Landi degl'Innocenti, E., Martinez Pillet, V., & Lites, B. W. 1996, ApJ, 466, 537

Sánchez Almeida, J. & Lites, B. W. 2000, ApJ, 532, 1215

Sánchez Almeida, J. & Trujillo Bueno, J. 1999, ApJ, 526, 1013

Sánchez Almeida, J., Viticchié, B., Landi Degl'Innocenti, E., & Berrilli, F. 2008, ApJ, 675, 906

Schrijver, C. J. & Title, A. M. 2003, ApJL, 597, L165

Schüssler, M. & Vögler, A. 2008, A&A, 481, L5

Shchukina, N. & Trujillo Bueno, J. 2003, in Astronomical Society of the Pacific Conference Series, Vol. 307, Astronomical Society of the Pacific Conference Series, ed. J. Trujillo-Bueno & J. Sanchez Almeida, 336–+

Shelyag, S., Schüssler, M., Solanki, S. K., Berdyugina, S. V., & Vögler, A. 2004, A&A, 427, 335

Shelyag, S., Schüssler, M., Solanki, S. K., & Vögler, A. 2007, A&A, 469, 731

Sigwarth, M., Balasubramaniam, K. S., Knölker, M., & Schmidt, W. 1999, A&A, 349, 941

Smithson, R. C. 1975, in Bulletin of the American Astronomical Society, Vol. 7, Bulletin of the American Astronomical Society, 346–+

Sobotka, M. 2003, Astronomische Nachrichten, 324, 369

Socas-Navarro, H., López Ariste, A., & Lites, B. W. 2001, ApJ, 553, 949

Socas-Navarro, H. & Sánchez Almeida, J. 2002, ApJ, 565, 1323

Solanki, S. K. 1986, A&A, 168, 311

Solanki, S. K. 1993, Space Science Reviews, 63, 1

Solanki, S. K. & Brigljevic, V. 1992, A&A, 262, L29

Solanki, S. K. & Steenbock, W. 1988, A&A, 189, 243

Spiegel, E. A. 1957, ApJ, 126, 202

Spiegel, E. A. & Weiss, N. O. 1980, Nature, 287, 616

Spruit, H. C. 1976, Sol. Phys., 50, 269

Spruit, H. C. 1979, Sol. Phys., 61, 363

Stein, R. F., Bercik, D., & Nordlund, Å. 2003, in Astronomical Society of the Pacific Conference Series, Vol. 286, Current Theoretical Models and Future High Resolution Solar Observations: Preparing for ATST, ed. A. A. Pevtsov & H. Uitenbroek, 121–+

Stein, R. F. & Nordlund, Å. 2003, in IAU Symposium, Vol. 210, Modelling of Stellar Atmospheres, ed. N. Piskunov, W. W. Weiss, & D. F. Gray, 169–+

Stein, R. F. & Nordlund, Å. 2006, ApJ, 642, 1246

Steiner, O. 1999, in Astronomical Society of the Pacific Conference Series, Vol. 184, Third Advances in Solar Physics Euroconference: Magnetic Fields and Oscillations, ed. B. Schmieder, A. Hofmann, & J. Staude, 38–54

Steiner, O. 2003, A&A, 406, 1083

Steiner, O., Grossmann-Doerth, U., Knoelker, M., & Schuessler, M. 1998, ApJ, 495, 468

Stenflo, J. O. 1982, Sol. Phys., 80, 209

Suematsu, Y., Tsuneta, S., Ichimoto, K., et al. 2008, Sol. Phys., 249, 197

Tarbell, T. D. 2007, Sol. Phys.

Thomas, J. H. & Weiss, N. O. 2004, ARAA, 42, 517

Trujillo Bueno, J., Shchukina, N., & Asensio Ramos, A. 2004, Nature, 430, 326

Tsuneta, S., Ichimoto, K., Katsukawa, Y., et al. 2008, Sol. Phys., 249, 167

Unno, W. 1959, ApJ, 129, 375

Unruh, Y. C., Solanki, S. K., & Fligge, M. 1999, A&A, 345, 635

van Ballegooijen, A. A., Nisenson, P., Noyes, R. W., et al. 1998, ApJ, 509, 435

Vince, I. & Erkapic, S. 1998, in IAU Symposium, Vol. 185, New Eyes to See Inside the Sun and Stars, ed. F.-L. Deubner, J. Christensen-Dalsgaard, & D. Kurtz, 459–+

Vince, I., Gopasyuk, O., Gopasyuk, S., & Vince, O. 2005a, Serbian Astronomical Journal, 170, 115

Vince, I., Vince, O., Ludmány, A., & Andriyenko, O. 2005b, Sol. Phys., 229, 273

Vitas, N. 2005, Memorie della Societa Astronomica Italiana Supplement, 7, 164

Vitas, N., Viticchiè, B., Rutten, R. J., & Vögler, A. 2008, ArXiv e-prints

Viticchié, B., Del Moro, D., & Berrilli, F. 2006, ApJ, 652, 1734

Vlahos, L., Fragos, T., Isliker, H., & Georgoulis, M. 2002, ApJ, 575, L87

Vögler, A. 2004, A&A, 421, 755

Vögler, A. & Schüssler, M. 2003, Astronomische Nachrichten, 324, 399

Vögler, A. & Schüssler, M. 2007, A&A, 465, L43

Vögler, A., Shelyag, S., Schüssler, M., et al. 2003, in IAU Symposium, Vol. 210, Modelling of Stellar Atmospheres, ed. N. Piskunov, W. W. Weiss, & D. F. Gray, 157–+

Vögler, A., Shelyag, S., Schüssler, M., et al. 2005, A&A, 429, 335

Wallace, L., Hinkle, K., & Livingston, W. 1998, An atlas of the spectrum of the solar photosphere from 13,500 to 28,000 cm-1 (3570 to 7405 A) (An atlas of the spectrum of the solar photosphere from 13,500 to 28,000 cm-1 (3570 to 7405 A), Publisher: Tucson, AZ: National Optical Astronomy Observatories, [1998])

Weiss, N. O. 1966, Royal Society of London Proceedings Series A, 293, 310

Wenzler, T., Solanki, S. K., & Krivova, N. A. 2005, A&A, 432, 1057

Wenzler, T., Solanki, S. K., Krivova, N. A., & Fröhlich, C. 2006, A&A, 460, 583

Zwaan, C. 1967, Sol. Phys., 1, 478

Acknowledgements

At the end of this three years I would like to say so many things about each person I worked with, but I already exceeded the "suggested" maximum number of pages for a PhD Thesis; for this reason, I'll be short.

"*Grazie di cuore*" Francesco for being not a "formal" supervisor, but an ideal colleague, for supporting me as a person, not as a mere PhD student and for sharing so many scientific ideas and great time with me.

"*Grazie*" to the whole Tor Vergata Solar Physics Group. "*Grazie*" for being such a good and important part of my life in the last three years and "*grazie*" for your constant help and support.

"*Muchas gracias*" Jorge, for giving me the opportunity to work with you, for introducing me in the "Spectropolarimetry Global (madness) Community" and for your invaluable help during the whole PhD experience. I hope your future contribution to the "quiet Sun cause" will be as important as in the past.

"*Gracias*" Arturo for your collaboration and for your availability while working on the manganese stuff.

To José Antonio, Manuel, to all the persons working at the Instituto de Astrofísica de Canarias and to the ones who passed away, "*muchas gracias*" for the great time we had together during my stay in Tenerife.

"*Danken*" Rob for giving me the opportunity to work with you, such a "Giant" in Solar Physics. "*Danken*" for introducing me to the people working in the Solar Physics Group at Utrecht University.

"*Hvala*" Nikola for being a great colleague ("magic working dwarf" for Rob) and good friend, for your support, help and for the great time we spent together. I wish you the best for your future!

"Thanks" Mark for your collaboration in the development of the numerical model.

"*Grazie*" Enrico and Claudio for your support, for the great dinners we had together laughing about physics and for being great friends since the very beginning.

"*Grazie*" to my italian friends and family for being my life out of the work.

"*Gracias*" to my spanish friends and to Sara's family, you are the reason why I miss Tenerife so much while staying in Italy.

"*Gracias Mi Amor!*" This Thesis is for you.

The contents of this PhD thesis are published on refereed journals in Viticchié et al. (2006), Sánchez Almeida et al. (2008), Berrilli et al. (2008), Vitas et al. (2008).